学位論文

Research on particle acceleration processes
in radio relics of the galaxy clusters
1RXS J0603.3+4214 and RXC J1053.7+5453
with X-ray and radio observations

(X 線、電波観測による銀河団 1RXS J0603.3+4214 と
RXC J1053.7+5453 に付随する電波レリック周辺領域での
粒子加速過程に関する研究)

February, 2018

Graduate School of Science and Engineering
Yamagata University
Madoka Itahana

Abstract

The standard theory of cosmological structure formation tells us that rich galaxy clusters form via mergers and absorptions of smaller galaxy clusters and groups. Cluster major mergers are the most energetic phenomena in the universe. Merging clusters are the largest particle accelerators in the universe, which are characterized by the huge associated energy, long lifetime, and large dynamical time scale. Mergers have great impacts on cluster evolution. Indeed, numerical simulations show that mergers cause shocks and turbulence in the intracluster medium (ICM). While a large part of kinetic energy is converted into thermal ICM during cluster mergers, some part of it will be converted into a non-thermal form such as magnetic field and cosmic-rays. In fact, some merging clusters have diffuse non-thermal radio sources, which is direct evidence of the existence of the cosmic-ray electrons whose energy is $\sim$ GeV and the magnetic fields of $\sim \mu$G in the ICM. Radio relics are usually in cluster outwards and show an arc like shape. Because of their locations and morphology, it is believed that radio relics should have a close connection with shock fronts caused by cluster mergers. Recently, temperature and density jumps have been found in the ICM across the relic in some clusters. Mach numbers of shocks can be estimated from radio and X-ray observations independently. We research on particle acceleration processes in radio relics by comparing the Mach numbers from both the radio and X-ray observations. Large sample size is necessary to draw definite conclusions. Therefore, in order to increase the sample, we observed the fields around the relics in the galaxy clusters 1RXS J0603.3+4214 (Toothbrush) and RXC J1053.7+5453 (RXJ1053) with Suzaku.

The galaxy clusters 1RXS J0603.3+4214 and RXC J1053.7+5453 have radio relics. In the galaxy clusters 1RXS J0603.3+4214, the north relic is well known for a peculiar linear shape and nicknamed by "Toothbrush". We obtained Mach numbers of $M_{\rm X,Tooth} \sim 1.5$ and $M_{\rm X,1053} \sim 1.4$ at the outer edge of Toothbrush and RXJ1053 relic, respectively, from Suzaku data. Radio observations indicate the radio spectral index is $\alpha = 0.6 \sim 0.7$ at the outer edge of Toothbrush relic. This means the Mach number is $M_{\rm radio,Tooth} \sim 4$, on the assumption that these electrons are generated following the simplest

diffusive shock acceleration (DSA) theory. Our result is significantly lower than the estimated mach number from the radio data. This suggests that the DSA theory is invalid for Toothbrush relic. Moreover, we derived a lower limit of the magnetic field strength by comparing of the upper limit to the inverse Compton X-ray with radio flux for Toothbrush and RXJ1053 relic. In this thesis, based on these results, we discuss physical states and particle acceleration processes of relics, and merging processes in the galaxy clusters 1RXS J0603.3+4214 and RXC J1053.7+5453.

Contents

List of Figures

List of Tables

Chapter 1

Introduction

1.1 Clusters of Galaxies

The standard theory of cosmological structure formation tells us that rich galaxy clusters form through mergers and absorption of smaller galaxy clusters and groups. Galaxy clusters consist of the galaxies, thermal hot gas ($kT \sim$ keV) and dark matter. This thermal plasma is commonly referred to as intracluster medium (ICM). The typical size and mass of galaxy clusters are $\sim$ Mpc and $10^{14-15} M_{\odot}$, respectively. Cluster major mergers are the most energetic phenomena in the universe. The typical energy relevant to merger events is

$$W = \frac{1}{2} M v^2 = 10^{63} \left(\frac{M}{10^{14} M_{\odot}} \right) \left(\frac{v}{1000 \text{ km s}^{-1}} \right)^2 \text{erg}, \tag{1.1}$$

where M and v are the mass and velocity of the galaxy cluster, respectively. In some clusters, edge-like structures are found in X-ray images observed by Chandra and XMM-Newton. Such features are believed to be a shock or cold front. Density, temperature, and pressure profiles show a discontinuity across a shock front. Similarly, across a cold front, the density and temperature are discontinuous, but the pressure is continuous. It is believed that these are evidence of a cluster merger. Indeed, numerical simulations show that shock and contact discontinuities appear in the ICM during cluster major mergers [79, 98, 4, 100]. The features of a contact discontinuity agree with those of cold fronts. While a large part of the dissipated energy in the shocks and

turbulence is transformed into the thermal ICM, some will be converted into a non-thermal form such as cosmic-rays and magnetic fields [65, 99, 119, 27].

1.1.1 Observations

Galaxy clusters are observed in the X-ray, optical, and radio. From X-ray observations, we can observe an X-ray emission from ICM which fill in clusters, and measure the physical quantities of the thermal ICM [24, 111, 94]. ICM is the dominant component of baryons in clusters of galaxies. From optical observations, we can observe member galaxies in galaxy clusters, and measure the velocity distribution, virial radius and redshift. Additionally, we can derive a mass distribution, most of which is composed of the dark matter, using a weak gravitational lensing effect [88, 66, 69, 70]. From radio observations, we can observe a diffuse non-thermal radio emission from relativistic electrons [37, 33, 104, 107]. In addition, using Sunyaev-Zel'dovich (SZ) effect [95], we can measure the physical quantities of the thermal ICM [76, 77]. Figure 1.1 shows Coma cluster images in various wavelength bands.

1.2 Diffuse Non-thermal Radio Sources

Some clusters host diffuse non-thermal radio sources [33, 21]. The radio emission is owing to synchrotron radiation by the interaction of relativistic electrons whose energy is $\sim$ GeV, and magnetic field of $\sim \mu$G in the ICM. They are classified into three categories by their size, morphology and location. Radio halos have morphology similar to the ICM X-ray emission and are located in the central part of the cluster[32, 37, 105, 84]. They are typically extended with sizes of ≥ 1 Mpc in the merging cluster (top left panel in figure 1.2). Mini halos are also located in the cluster center, but their typical size is much smaller ($\sim$ 0.5 Mpc) than halos [33, 39] (top right panel in figure 1.2). Radio relics are usually in cluster outskirts and show an arc-like shape [80, 13, 104, 107] (bottom panel in figure 1.2). It is believed that radio relics should have a close connection with shock fronts caused by cluster mergers because of their morphology and location. The high-energy electrons in synchrotron emission regions such as radio halos and relics, emit non-thermal

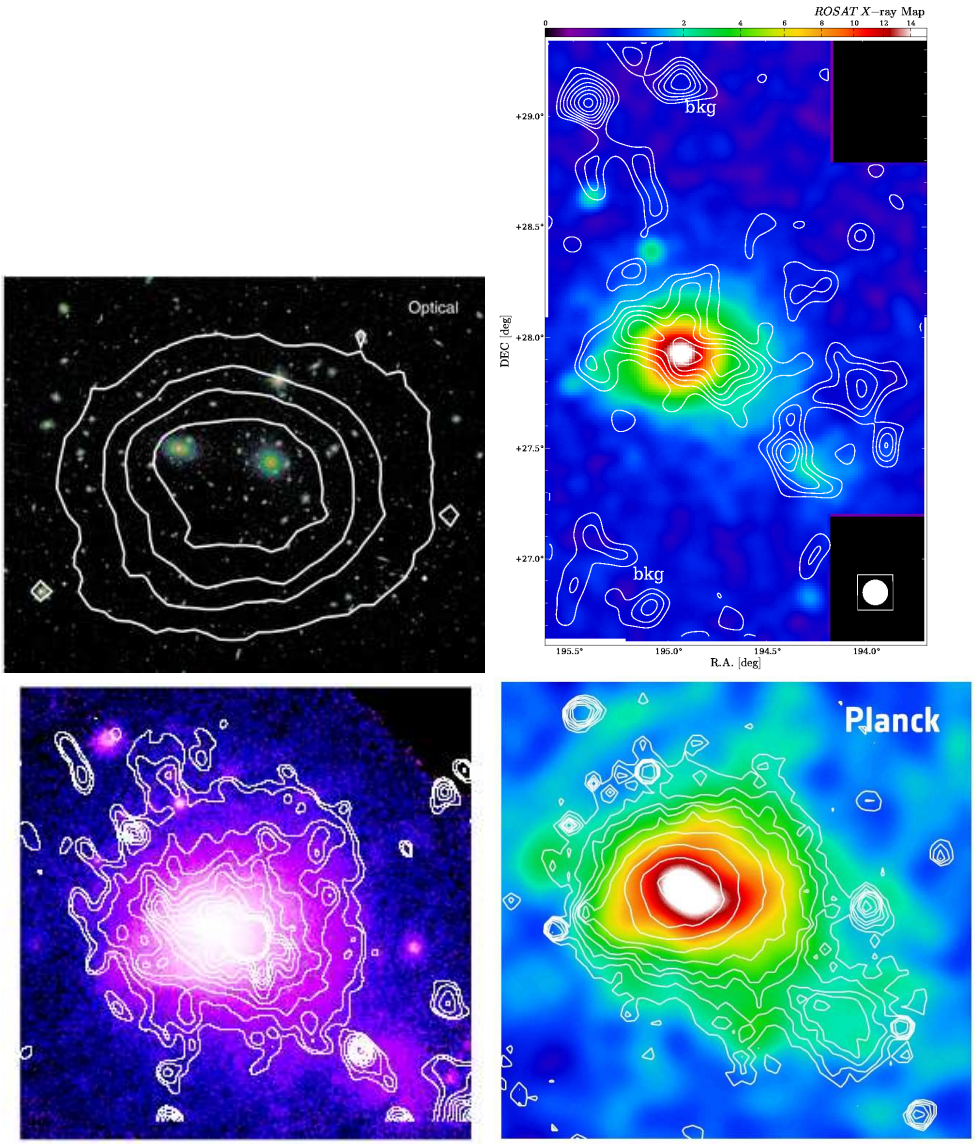

Figure 1.1: Images of the Coma cluster.
Top left:The optical image (colors) with X-ray contours (XMM-Newton) [31]. Top right: The X-ray image (ROSAT) with weak-lensing mass contours (Subaru) [68]. Bottom left: The X-ray image (ROSAT) with radio contours [58]. Bottom right: The Coma cluster as seen by Planck through the SZ effect (colors) and ROSAT in X-ray (contours) (image credits: ESA / LFI and HFI Consortia).

X-rays via the inverse Compton scattering of cosmic microwave background (CMB) photons [15]. In the non-thermal radio emission region, we are able to derive the magnetic field strength by comparing synchrotron radio and non-thermal X-ray flux. Even if only the upper limit of the inverse Compton flux is obtained, we can estimate the lower limit of the magnetic field strength. Although a lot of efforts have been made to search for such non-thermal X-rays from cluster radio halos and relics [3, 61, 93, 9], no firm detections have been reported.

1.3 Particle Acceleration Theory

1.3.1 Shock waves

Shock waves are discontinuities of the physical quantities, which are caused by the supersonic velocity medium. Perturbations in a gas are propagated away from their source at the sound speed in the medium. If a disturbance is propagated at a velocity greater than the sound speed, it cannot behave like a sound wave. Therefore, the physical quantities (etc. temperature, velocity, and gas density) show a discontinuity between the upstream and downstream of the shock. The region of progressing direction having no prior knowledge of shock imminent arrival. Such shocks are found from X-ray observations in the galaxy cluster (Bullet cluster; [56]). Here, this subsection was referred to the textbook Longair (1994) [54].

We assume that plasma vertically flows toward a shock. In the upstream of the shock wave, the pressure, density and temperature of the plasma are p_1, ρ_1 and T_1, respectively, and the sound speed is $c_s = \sqrt{\gamma P/\rho}$. Similarly, in the downstream of the shock wave, the pressure, density, and temperature are p_2, ρ_2, and T_2, respectively, and the gas moves supersonically at speed $u > c_s$. For convenience, we assume a reference frame where the shock wave is stationary. In this frame, the gas flows towards the shock at velocity of V_1, where $V_1 = u$, and the gas velocity becomes V_2 when it passes through the shock (figure 1.3). The flux of mass, momentum, and energy are conserved at

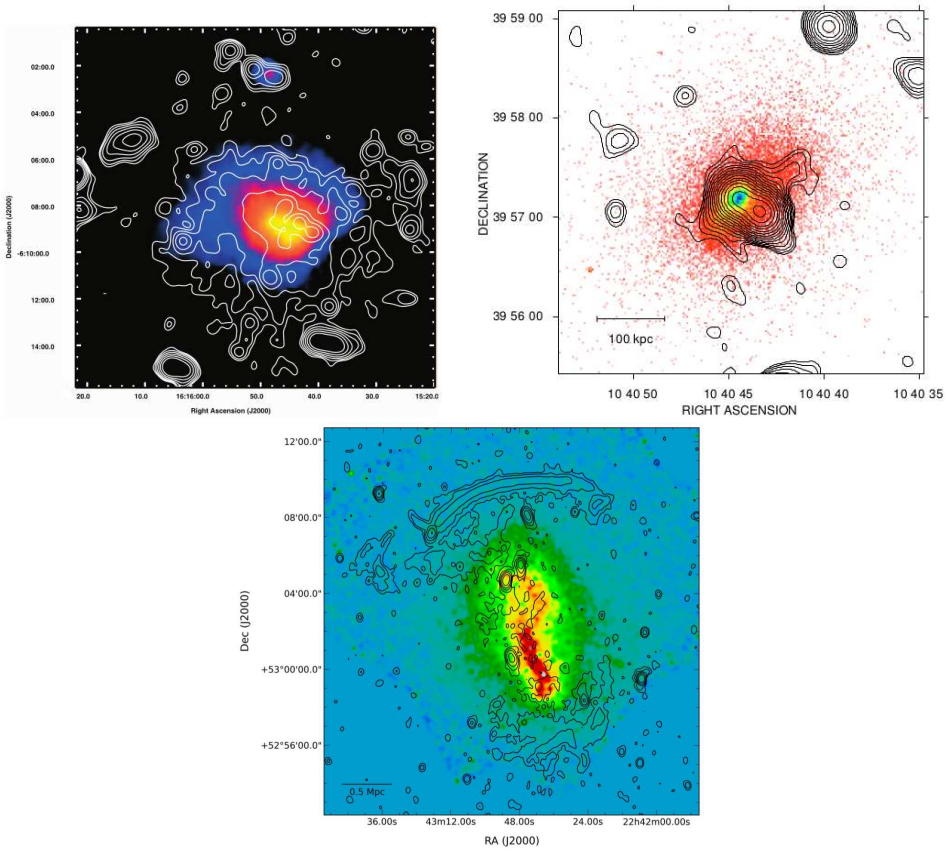

Figure 1.2: Diffuse non-thermal radio sources in clusters of galaxies. Top left: A2163 X-ray image (Chandra; 0.8-6.5 keV) with radio contours at 1.4 GHz [37]. We can see the radio halo around the cluster center. Top right: A1068 X-ray image (Chandra; 0.5-4 keV) with radio contours at 1.4 GHz [38]. There is a mini-halo in the cluster center. Bottom: CIZA2242 X-ray image (Chandra; 0.5-7 keV) with radio contour at 1.4 GHz [64]. There are radio relics at the north and south side of cluster.

the upstream and downstream of the shock wave as follows:

$$\rho_1 V_1 = \rho_2 V_2, \tag{1.2}$$

$$\rho_1 V_1^2 = \rho_2 V_2^2 + p_2, \tag{1.3}$$

$$\frac{1}{2}V_1^2 + \frac{\gamma}{\gamma-1}\frac{p_1}{\rho_1} = \frac{1}{2}V_2^2 + \frac{\gamma}{\gamma-1}\frac{p_2}{\rho_2}, \tag{1.4}$$

where γ is the specific heat ratio. Here, we consider the Mach number (M) of the shock wave which is defined to be $M = V/c_s$. Thus, the Mach numbers in the upstream and downstream of the shock wave are

$$M_1^2 = \frac{\rho_1 V_1^2}{\gamma p_1}, \tag{1.5}$$

$$M_2^2 = \frac{\rho_2 V_2^2}{\gamma p_2}. \tag{1.6}$$

From these equations, the relations between the densities or pressures and Mach numbers, respectively, are derived as follows:

$$\frac{\rho_2}{\rho_1} = \frac{V_1}{V_2} = \frac{(\gamma+1)M_1^2}{(\gamma-1)M_1^2+2}, \tag{1.7}$$

$$\frac{p_2}{p_1} = \frac{2\gamma M_1^2 - (\gamma-1)}{\gamma+1}. \tag{1.8}$$

We can derive the relation between T_1 and T_2 from the ideal gas law, $T \propto p/\rho$,

$$\frac{T_2}{T_1} = \frac{p_2\rho_1}{p_1\rho_2} = \frac{[2\gamma M_1^2 - (\gamma-1)][(\gamma-1)M_1^2+2]}{(\gamma+1)^2 M_1^2}. \tag{1.9}$$

In the very strong shocks ($M_1 \gg 1$), we find the following results

$$\frac{p_2}{p_1} = \frac{2\gamma M_1^2}{\gamma+1}, \tag{1.10}$$

$$\frac{\rho_2}{\rho_1} = \frac{\gamma+1}{\gamma-1}, \tag{1.11}$$

$$\frac{T_2}{T_1} = \frac{2\gamma(\gamma-1)M_1^2}{(\gamma+1)^2}. \tag{1.12}$$

In this case, therefore, the pressure and temperature ratios can become arbitrarily large, but the density ratio attains a maximum value of $(\gamma+1)/(\gamma-1)$. For example, ideal monatomic gas has $\gamma = 5/3$, thus, $\rho_2/\rho_1 = 4$ in the very strong shocks.

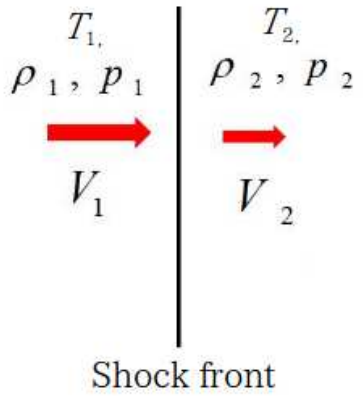

Figure 1.3: The flow of gas through the shock front in the frame of reference where the shock front is stationary.

1.3.2 Fermi acceleration

In this subsection, we describe a first-order Fermi acceleration. First, we consider the particle which crosses from the upstream to downstream side of the shock. Assuming the gas on the downstream side approaches the particle at a velocity of V, and performing a Lorentz transformation, we obtain the relation of the particle's energy as follow;

$$E' = \gamma_V (E + p_x V), \tag{1.13}$$

where p is momentum of the particle and the x-axis is take to be a perpendicular to the shock. Here, the shock is assumed to be non-relativistic, $V \ll c$, $\gamma_V = (1 - V^2/c^2) \sim 1$, however, the particles are relativistic, which have the energy $E = pc$ and momentum $p_x = (E/c)\cos\theta$. Thus,

$$\Delta E = pV\cos\theta \tag{1.14}$$

$$\frac{\Delta E}{E} = \frac{V}{c}\cos\theta, \tag{1.15}$$

where θ is the angle between the x-axis and the progress direction of the particle (figure 1.4). The number of particles within the angles $\theta \sim \theta + d\theta$ is proportional to $\sin\theta d\theta$, and the probability that the rate at which they

approach the shock front is proportional to their velocities of x-axis component, $c\cos\theta$. Therefore, the probability that the particle cross the shock is proportional to $\sin\theta\cos\theta d\theta$. The probability distribution of the particles approaching the shock is

$$P(\theta) = 2\sin\theta\cos\theta d\theta, \tag{1.16}$$

where the range of θ is $0 \sim \pi/2$. Therefore, the average energy that the particle can be obtained when it crossing the shock is

$$\left\langle \frac{\Delta E}{E} \right\rangle = \frac{V}{c}\int_0^{\pi/2} 2\cos^2\theta\sin\theta d\theta = \frac{2}{3}\frac{V}{c}. \tag{1.17}$$

The velocity vector of the particle is randomized without energy loss from scattering in the downstream region and it can crosses the shock again. Thus, the average of the increased energy in one round trip across the shock is

$$\left\langle \frac{\Delta E}{E} \right\rangle = \frac{4}{3}\frac{V}{c}. \tag{1.18}$$

In order to derive the energy spectrum of the accelerated particles, we must consider the escape probability in one round trip. To calculate the escape probability, we use the argument due to Bell (1978a) [16]. We define the average energy of the particle after one round trip across the shock as $E = \beta E_0$ and the probability that the particle within the accelerating region as P. Here, from equation (1.18) $\beta = E/E_0 = 1 + 4V/3c$. After k round trips, the number of particles with $E = E_0\beta^k$ is $N = N_0 P^k$. In case of an isotropic distribution, the number of particles crossing the shock front per unit time is given $nc/4$, where n is the number density of particles. Because the particles in downstream are away at the velocity V_2 from shock front, it can be seen that particles are removed from the shock region at a rate nV_2. Therefore, the fraction of the particles lost is $4V_2/c$. The probability of crossing the shock again can be $(1 - 4V_2/c)$, and in case of k round trip,

$$P = \left(1 - \frac{4V_2}{c}\right)^k. \tag{1.19}$$

Thus,

$$\ln P = \ln\left(1 - \frac{4V_2}{c}\right) \approx -\frac{4V_2}{c}, \tag{1.20}$$

$$\ln \beta = \ln\left(1 + \frac{4V}{3c}\right) \approx \frac{4V}{3c}, \tag{1.21}$$

and hence

$$\frac{N}{N_0} = \left(\frac{E}{E_0}\right)^{\ln P/\ln\beta}. \tag{1.22}$$

Therefore, we obtain the differential energy spectrum of the particles as follows:

$$N(E)dE \propto E^{-[1+3V_2/(V_1-V_2)]}dE. \tag{1.23}$$

In other word, particles have a power-law energy spectrum and the index of spectrum p is

$$p = 1 + \frac{3V_2}{V_2 - V_1} = \frac{C+2}{C-1}, \tag{1.24}$$

where C is a shock compression. For more detailed treatments, please see the original papers and earlier reviews [16, 17, 28, 54].

1.4 Radiative Processes

In this section, we describe radiative processes of the thermal bremsstrahlung, synchrotron radiation, inverse Compton scattering. For more information, please see Rybicki and Lightman (1979) [81].

1.4.1 Thermal bremsstrahlung emission

In a cluster of galaxies, the ICM is optically thin with the temperatures about 10^8 K. Therefore, the ICM is emitting thermal X-ray through thermal bremsstrahlung of electrons [83]. Because the ICM is spreads over the entire cluster, it can provide good information regarding the physical properties of the cluster. We describe a thermal bremsstrahlung emission in this subsection.

Radiation due to the acceleration of a charged particle in the Coulomb field of another one is called "bremsstrahlung". When the thermal electron

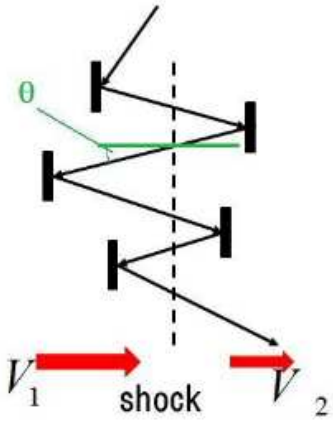

Figure 1.4: Schematic diagram of the diffusive shock acceleration. The particle which have the much faster velocity than the shock is accelerated by scattering around the shock.The x-axis is the direction perpendicular to the shock and θ is the angle between the x-axis and the progress direction of the particle.

goes through near the ion, the orbit of electron is curved. In this case, the electron emit a X-ray. Assuming an isotropic velocity distribution of electrons, the probability dP that a electron has a speed between v and dv is

$$dP \propto v^2 \exp(-\frac{mv^2}{2kT})dv, \tag{1.25}$$

where kT, m, and v are the temperature, mass, and velocity of the electron, respectively. Now we would like to integrate thermal bremsstrahlung emission from each electrons. The emissivity of bremsstrahlung (Rybicki and Lightman (1979) [81]) is

$$\frac{dW}{d\omega dV dt} = \frac{16\pi e^6}{3\sqrt{3}c^3m^2v} n_e n_i Z^2 g_{ff}(v,\omega), \tag{1.26}$$

where n_e and n_i are the number density of electron and ion, respectively. Z is the charge of an ion and g_{ff} is the Gaunt factor which is a certain function of the energy of the electron and of the frequency of the emission. Therefore, integrating the equation (1.26) with a weight of equation (1.25) over velocity,

we obtain

$$\frac{dW(T,\omega)}{d\omega dV dt} = \frac{\int_{v_{\rm min}}^{\infty} \frac{dW(v,\omega)}{d\omega dV dt} v^2 \exp\left(-\frac{mv^2}{2kT}\right) dv}{\int_0^{\infty} v^2 \exp\left(-\frac{mv^2}{2kT}\right) dv}. \tag{1.27}$$

The incident velocity of particle must be at least such that

$$h\nu \leq \frac{1}{2} m v^2, \tag{1.28}$$

because otherwise a photon of energy $h\nu$ could not be created. Therefore, $v_{\rm min} \equiv (2h\nu/m)^{1/2}$ in equation (1.27). Using $d\omega = 2\pi d\nu$, we obtain the following equation

$$\frac{dW}{dV dt d\nu} = \frac{2^5 \pi e^6}{3mc^3} \left(\frac{2\pi}{3km}\right)^{1/2} T^{-1/2} Z^2 n_e n_i e^{-h\nu/kT} \bar{g}_{ff}, \tag{1.29}$$

where $\bar{g}_{ff}(T,\nu)$ is a velocity averaged Gaunt factor. Integrating equation (1.29) over frequency,

$$\frac{dW}{dV dt} = \frac{2^5 \pi e^6}{3hmc^3} \left(\frac{2\pi}{3km}\right)^{1/2} T^{1/2} Z^2 n_e n_i \bar{g}_{ff2}, \tag{1.30}$$

where $\bar{g}_{ff2}(T)$ is a frequency average of the velocity averaged Gaunt factor. The X-ray emissivity by the thermal bremsstrahlung is dependent on the temperature and density of the electron and ion as follows:

$$\frac{dW}{dV dt} \sim n_e n_i T^{1/2}. \tag{1.31}$$

Therefore, if we have known the volume of X-ray source and obtained the temperature and X-ray radiation intensity from observations, we derive the density of electron and ion of the ICM. We also see that bremsstrahlung has a rather flat spectrum in a logarithmic scales plot up to its cutoff at about $h\nu \sim kT$ (figure 1.5).

1.4.2 Synchrotron radiation

Some clusters host diffuse non-thermal radio sources. In these galaxy clusters, there are a relativistic high energy ($\sim$ GeV) electrons. These high energy

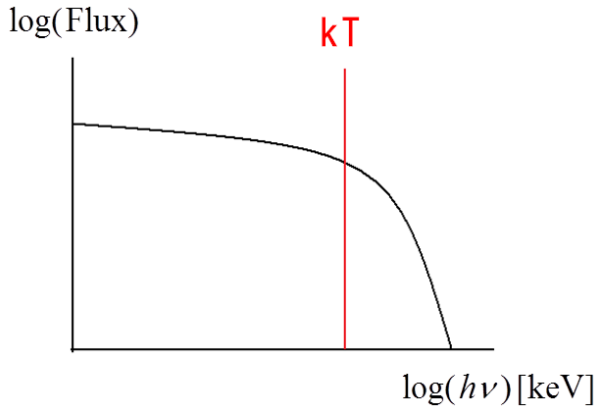

Figure 1.5: Schematic diagram of the thermal bremsstrahlung spectrum. We also see that bremsstrahlung has a rather flat spectrum in a logarithmic scales plot up to its cutoff at about $h\nu \sim kT$.

electrons emit the radio by synchrotron radiation. In this subsection, we describe a synchrotron radiation.

Radiation from the relativistic high energy electrons gyrating in a magnetic field is called "synchrotron radiation". The radiated power ($P_{\rm sync}$) of synchrotron radiation from an electron is

$$\begin{aligned} P_{\rm sync} &= \frac{4}{3}\sigma_T c\gamma^2\beta^2\frac{B^2}{8\pi} \\ &= \frac{4}{3}\sigma_T c\gamma^2\beta^2 U_B, \end{aligned} \tag{1.32}$$

where B, γ, and σ_T are the magnetic field strength, the Lorentz factor of the electron, and Thomson cross section, respectively, $U_B = B^2/8\pi$ is the energy density of the magnetic field, and $\beta \equiv v/c$ with the velocity of electron v. From equation (1.32), we see that the radiated power ($P_{\rm sync}$) of synchrotron radiation is dependent on the magnetic field strength.

The energy distribution of the high energy electrons which are accelerated by Fermi acceleration (see subsection 1.3.2), can be approximated as follows:

$$N(E)dE = CE^{-p}dE \text{ or } N(\gamma)d\gamma = C\gamma^{-p}d\gamma, \tag{1.33}$$

where C is normalization factor. The spectrum of synchrotron radiation by electrons with such a energy distribution shows a similar form of power-law

as follows:

$$S_\nu \propto \nu^{-\alpha_\nu}. \tag{1.34}$$

Here, the spectral index (α_ν) is related to that of particle distribution (p) as

$$\alpha_\nu \equiv \frac{p-1}{2}. \tag{1.35}$$

Therefore, the radiation spectrum is flatter than the energy distribution of the electron.

1.4.3 Inverse Compton scattering

The high-energy electrons in synchrotron emission regions such as radio halos and relics, emit non-thermal X-rays via the inverse Compton scattering of cosmic microwave background (CMB) photons [15]. Although a lot of efforts have been made to search for such non-thermal X-rays from cluster radio halos and relics [3, 61, 93, 9], no firm detections are reported. In this section, we describe a process of inverse Compton scattering.

When the electron is at rest, net energy may be transferred from photon to the electron. This process is called the "Compton scattering". On the other hand, when the moving electron has sufficient kinetic energy compared to the photon, net energy may be transferred from the electron to the photon. Such a scattering process is called "inverse Compton scattering". Assuming the photons have isotropic distribution, the radiated power via the inverse Compton scattering from an electron which has energy of $\gamma m_e c^2$ is

$$P_{\rm IC} = \frac{4}{3}\sigma_T c \gamma^2 \beta^2 U_{\rm ph}, \tag{1.36}$$

where $U_{\rm ph}$ is the energy density of the photon.

When the high energy electrons have the energy distribution same as equation (1.33), the energy spectrum of the inverse Compton is

$$P_{\rm tot}(\epsilon) \propto \epsilon^{-s}. \tag{1.37}$$

The power-law index becomes

$$s = \frac{p-1}{2}, \tag{1.38}$$

same as in the case of synchrotron emission (§1.4.2).

1.5 Motivation

Because of morphology and location of radio relics, it is believed that they should have a close connection with shock fronts caused by cluster mergers. The shocks are expected to be located at the outer edge of the relics. Recently, in fact, temperature and density jumps are found across the relic outer edge (figure 1.6) in some clusters by X-ray observations [35, 5, 7, 63, 9, 48]. This is direct evidence of the association of relics with shocks. Mach numbers of shocks related to the relics can be estimated from radio and X-ray observations independently. From radio observations, we can obtain the radio spectral index (α_ν in equation (1.34)) at the relic outer edges. Assuming a simple diffusive shock acceleration (DSA) theory [28, 18], which is a first-order Fermi acceleration (§1.3.2) in the presence of shock waves, the obtained spectral index can be related to the shock Mach number ($M_{\rm radio}$) [81] as follows

$$\alpha_{\rm inj} = \frac{M_{\rm radio}^2 + 1}{M_{\rm radio}^2 - 1} - \frac{1}{2}, \tag{1.39}$$

where $\alpha_{\rm inj}$ is the injection index which is flatter by 0.5 compared to the integrated spectral index α_ν [73, 59]. On the other hand, from X-ray observations, we can obtain the temperature and density distribution around relics. We can estimate the Mach number with Rankine-Hugoniot conditions (equation (1.9) and (1.7)) from the temperature and density jump at shock front [53, 89]. If the simple DSA model is valid, both methods have to give us consistent results. Thus, comparison of high quality X-ray data with excellent radio spectra is useful to get insights into the particle acceleration processes. Akamatsu and Kawahara (2013) [6] performed the first systematic study on this issue, although the number of sample was not enough. Figure 1.7 shows Mach numbers derived from the radio observation $M_{\rm radio}$ plotted against those from the ICM temperature $M_{\rm X,kT}$ in Akamatsu and Kawahara (2013) [6]. Therefore, it is important to observe more relics in both radio and X-rays.

We research on particle acceleration processes in radio relics by comparing the both Mach number from the radio and X-ray observations. As mentioned above, the sample size is not large enough to draw definite conclusions at present. Thus, in order to increase the sample size, we observed the fields around the relics in the galaxy clusters 1RXS J0603.3+4214 (Toothbrush)

and RXC J1053.7+5453 (RXJ1053) with Suzaku. We measure temperatures across the radio relics for each cluster, and estimate Mach numbers of shocks at each relic outer edge. By comparing our results with those from radio observation, we can obtain the information of particle acceleration process in radio relics. In addition, we derived a lower limit of the magnetic field strength from a combination of the upper limit to the inverse Compton X-ray and radio flux for Toothbrush and RXJ1053 relic. In this thesis, based on these results, we discuss physical states and particle acceleration processes of relics, and merging processes in the galaxy clusters 1RXS J0603.3+4214 and RXC J1053.7+5453.

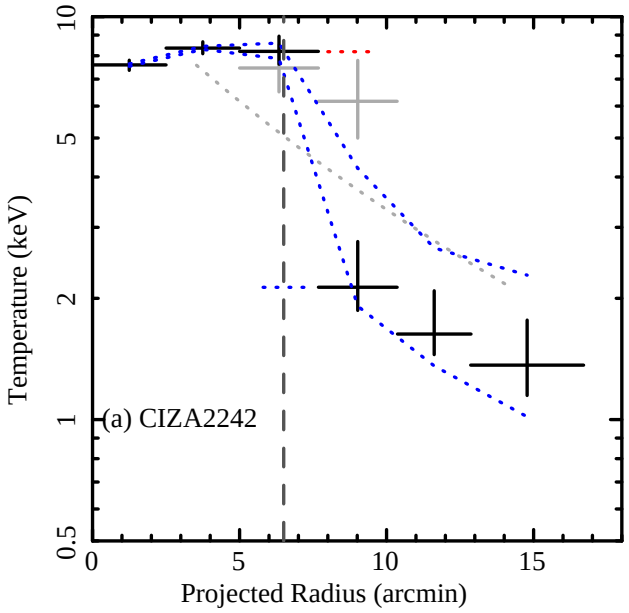

Figure 1.6: The ICM temperature profile of CIZA J2242.8+5301 across the northern relic [6].
The dashed line represents the radio relic position. We also see a temperature jump at the relic outer edge.

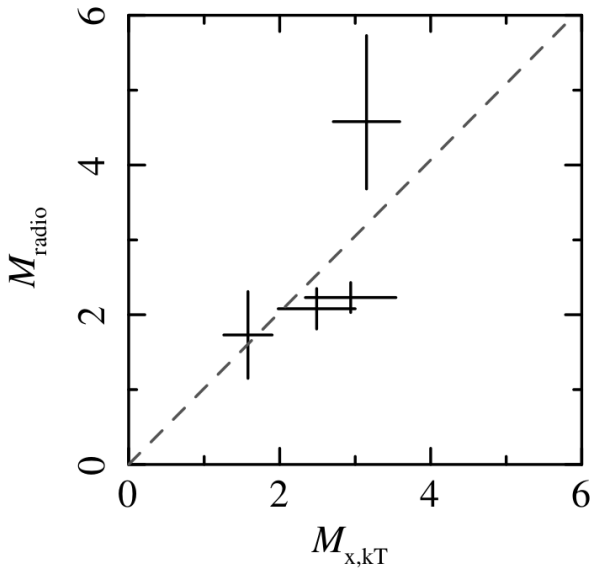

Figure 1.7: Mach numbers derived from the X-ray temperature and radio observations [6].
Mach numbers derived from the radio observation $M_{\rm radio}$ plotted against those from the ICM temperature $M_{\rm X,kT}$. The gray dotted line represents $M_{\rm radio} = M_{\rm X,kT}$.

Chapter 2

Galaxy Cluster 1RXS J0603.3+4214

1RXS J0603.3+4214 is merging cluster with radio relics and a halo at $z = 0.225$. The north radio relic is well known for a peculiar linear shape and nicknamed by "Toothbrush" [106], whose long axis length is 1.9 Mpc. van Weeren et al. (2012) reported the radio spectrum index at the relic outer edge is $\alpha = 0.6 \sim 0.7$, which means that the Mach number of shock is $M_{\rm radio} = 3.3 \sim 4.6$ [106]. This value is rather high for cluster merger shocks. In the XMM-Newton image, this cluster has an elongated north-south morphology [63]. This suggests that this cluster is in the later phase of a major merger. From the surface brightness analysis, Ogrean et al. (2013) reported that the north shock is offseted by $1'$ outwards from the relic outer edge and extended in the west of the relic [63]. The estimated Mack number of north shock becomes ~ 1.7, which is significantly lower than the result of radio observation. However, note that their results cloud be affected by the three dimensional density modeling and the projection effects.

We conducted a Suzaku X-ray observation of the field around the "Toothbrush" relic. The X-ray Imaging Spectrometer (XIS) aboard the Suzaku satellite [60] is more appropriate for observing low surface brightness diffuse sources than Chandra and XMM-Newton, thanks to its low and stable background [51]. This feature is very useful in investigating the physical properties of the ICM around cluster radio relics, which are generally located in the outer part

of the cluster.

Canonical cosmological parameters of $H_0 = 70$ Mpc^{-1} km s^{-1} , $\Omega_0 = 0.27$, and $\Lambda_0 = 0.73$ are used in this chapter. At the redshift of the this cluster ($z = 0.225$), 1 arcmin corresponds to 217 kpc. Unless otherwise stated, all uncertainties are given at the 90% confidence level.

2.1 Suzaku Observations and Data Reductions

We observed a field around the "Toothbrush" radio relic in galaxy cluster 1RXS J0603.3+4214 with Suzaku on 2012 October 7-10. In addition, a field offset by 1° in Galactic longitude was observed on 2012 October 14-15 to estimate the background components. A summary of the observations is given in table 2.1. We used HEAsoft version 6.16. The 20130305 calibration data files were adopted. The Suzaku XIS data were processed through default screening criteria as follows. Events with a GRADE of 0,2,3,4,6 and STATUS with 0:524287 were extracted. Data obtained at the South Atlantic Anomaly (SAA), within 436 s after the passage of SAA, and at low elevation angles from an Earth rim of $< 5°$ and a sun-lit Earth rim of $< 20°$ were excluded. As a result, the effective exposure times became 124.4 and 26.8 for the cluster and OFFSET field, respectively. In order to reduce the non-X-ray background (NXB) level, which increased after changing the amount of charge injection, we applied additional processing for XIS1 following the processes descriptions in the Suzaku XIS analysis topics [1)]. We did not use the XIS0 segment A which is damaged because of a micrometeorite accident [2)]. NXB spectra and images of XIS were generated using the ftool "xisnxbgen" [101]. Figure 2.1 shows a 0.5-8.0 keV XIS image with the 1.16-1.78 GHz radio contours [106].

2.2 Data Analysis and Results

For the spectral analysis of the XIS data, we generated redistribution matrix files (RMFs) and ancillary response files (ARFs) with the FTOOL "xisrmfgen" and "xissmarfgen" [45], respectively. Uniform emission over a circular region

[1)] http://www.astro.isas.jaxa.jp/suzaku/analysis/xis/xis1_ci_6_nxb/

[2)] http://www.astro.isas.ac.jp/suzaku/doc/suzakumemo/suzakumemo-2010-01.pdf

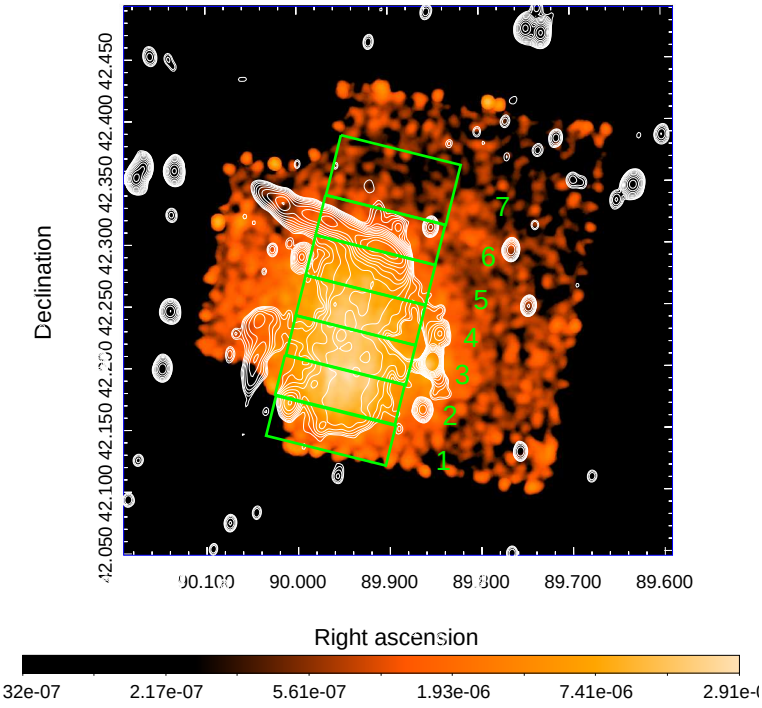

Figure 2.1: Suzaku XIS image of 1RXS J0603.3+4214 cluster.
An XIS3 image of 1RXS J0603.3+4214 cluster in the 0.5-8.0 keV band overlaid with the 1.16-1.78 GHz radio contours [106]. The X-ray image was corrected for exposure and vignetting effects after subtracting NXB, and smoothed it by a Gaussian kernel with $\sigma = 0.'26$. The regions used to investigate temperature distribution along the collision axis in subsection 2.2.2 are displayed as green boxes. The region numbers are also shown in green.

Table 2.1: An observational log of 1RXS J0603.3+4214

Name (Obs.ID)	(RA, Dec) (Deg)	Observation Date	Exposure (ks)[1)]
Suzaku			
1RXS J0603.3+4214			
(807001010)	(90.7885, +42.2628)	2012/10/7-10	124.4
OFFSET			
(807002010)	(92.2826, +42.2613)	2012/10/14-15	26.8

[1)] Effective exposure time after data screening as described in the text.

with $20'$ radius was used as an input image to generate an ARF. The solar abundances are normalized to Anders & Grevesse (1989) [10].

2.2.1 Background components

We estimate the background components using the data of OFFSET field. The region used for this purpose is shown in figure 2.2 by green circle. We assume that the background components are composed of the Local Hot Bubble (LHB), the Milky Way Halo (MWH) and the Cosmic X-ray background (CXB). Then we fit the spectrum of background field using the following model:

$$apec_{\rm LHB} + wabs * (apec_{\rm MWH} + powerlaw_{\rm CXB}), \tag{2.1}$$

where $apec_{\rm LHB}$, $apec_{\rm MWH}$ and $powerlaw_{\rm CXB}$ represent the LHB, MWH and CXB, respectively. We fix the temperature of LHB to 0.08 keV, and the redshift and abundance of both the LHB and MWH to zero and solar, respectively. The photon index of the CXB is fixed to 1.4 [52]. We assume $N_H = 1.79 \times 10^{21}$ cm^{-2} for the Galactic absorption [26]. For the spectral fitting of the background components, we used the energy band of 0.5-8.0 keV. However, the energy band of 1.7-1.8 keV was ignored, because the response matrix around the Si-K edge had residual uncertainties.

Figure 2.3 shows the spectra of the background field fitted with the abovementioned model, where the black, red and green crosses show the spectra of

XIS0, XIS1 and XIS3, respectively. The total and each component of the best-fit model spectra are also plotted as solid histograms, respectively. Table 2.2 shows the detailed results of the best-fit model. The obtained temperature of the MWH component ($kT = 0.56^{+0.12}_{-0.21}$ keV) is somewhat higher than the typical value ($kT \sim 0.3$ keV), which might be due to a patchy high temperature component found in the former analysis [118, 85].

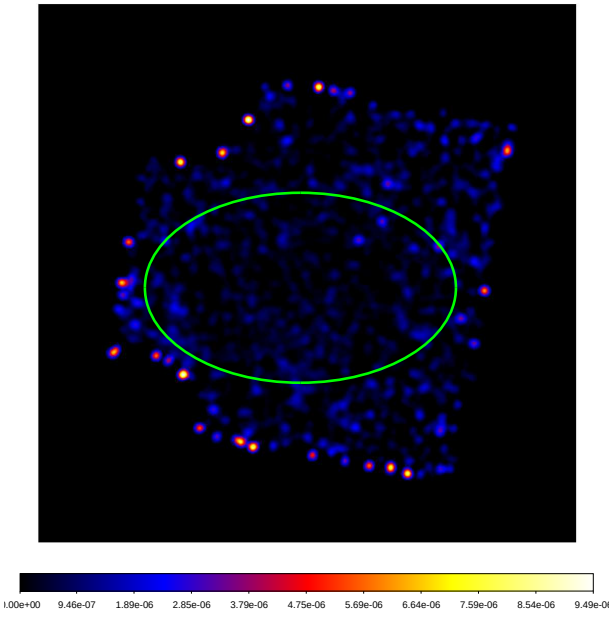

Figure 2.2: Suzaku XIS image of OFFSET field.
An XIS3 image of OFFSET field in the 0.5-8.0 keV band. The X-ray image was corrected for exposure and vignetting effects after subtracting NXB, and smoothed it by a Gaussian kernel with $\sigma = 0.'26$. The regions used to estimate the background components are displayed as green circle.

2.2.2 Temperature profile of collision axis

We investigate the temperature distribution along the collision axis to reveal the overall structure of the system. For this purpose, we chose regions as shown in figure 2.1 by green boxes marking. We fit the spectrum of each

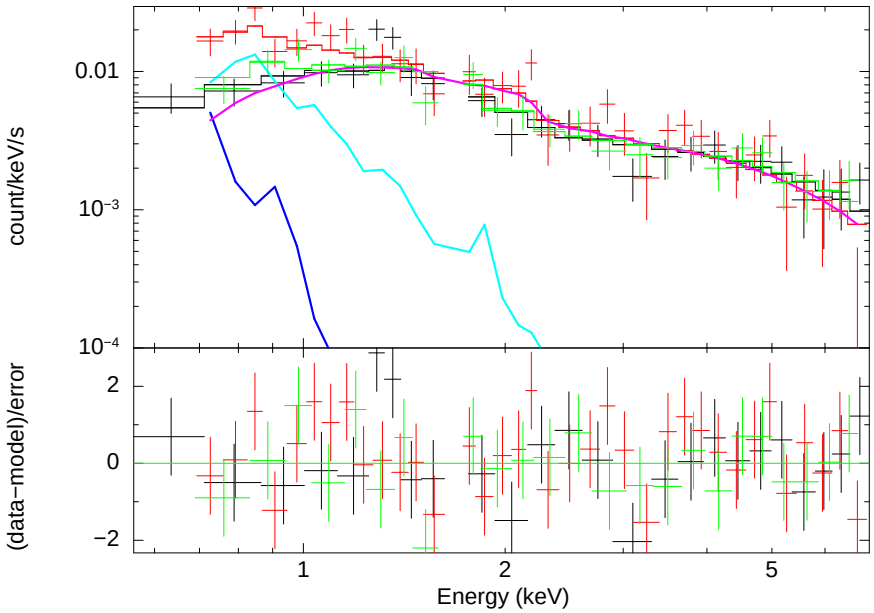

Figure 2.3: XIS spectra of the background field.
The XIS spectra of the background field fitted with the background model described in the text. The black, red, and green crosses show the spectra of XIS0, XIS1, and XIS3, respectively. The total spectra of the best-fit model are also plotted as solid histograms. The blue, light blue, and magenta solid histograms represent the LHB, MWH, and CXB components, respectively.

region by the following model:

$$constant * [apec_{\rm LHB} + wabs * (apec_{\rm MWH} + powerlaw_{\rm CXB} + apec_{\rm ICM})], \quad (2.2)$$

where $apec_{\rm ICM}$ represents the emission from the ICM. We fixed all the parameters of the background components ($apec_{\rm LHB}$, $apec_{\rm MWH}$, and $powerlaw_{\rm CXB}$) to the values derived from the background field analysis in subsection 2.2.1. We assume $N_H = 2.14 \times 10^{21}$ cm^{-2} for the Galactic absorption [26]. The redshift of the ICM component is fixed to 0.225, and the metal abundance is fixed to 0.2 solar for regions where we did not have enough photons to determine it. We introduced a parameter *constant* to correct for slight differences in normalization among the XIS sensors. It is known that there is uncertainty

Table 2.2: Best-fit parameters for the XIS spectra of the background field

Model Component	Parameter	Value
LHB	kT[1)]	0.08 (fixed)
	N[2)]	$5.91^{+3.56}_{-3.78} \times 10^{-2}$
MWH	kT[1)]	$0.56^{+0.12}_{-0.21}$
	N[2)]	$3.94^{+3.02}_{-1.03} \times 10^{-4}$
CXB	Γ[3)]	1.4 (fixed)
	N[4)]	$9.05^{+0.59}_{-0.58} \times 10^{-4}$
	$\chi^2/d.o.f$	72.67/81

[1)] Temperature of the each component in keV.
[2)] Normalization in the *apec* code for each component scaled with a factor $1/400\pi$.
$N = (1/400\pi) \int n_e n_H dV/[4\pi(1+z)^2 D_A^2] \times 10^{-14}$ cm^{-5} arcmin^{-2}, where D_A is the angular diameter distance to the source.
[3)] Photon index of the power-law component.
[4)] Normalization in the power-law component in photons keV^{-1} cm^{-2} s^{-1} at 1 keV

in the gain with negligible energy dependence in Suzaku XIS [51, 116, 14]. The value of *constant* is fixed to be unity for XIS1 and allowed to vary freely for XIS0 and XIS3. For the spectral fitting of the ICM component, we used the energy band of 0.7-7.0 keV. However, the energy band of 1.7-1.8 keV was ignored, because the response matrix around the Si-K edge had residual uncertainties. The resultant best-fit parameters are listed in table 2.3. Figure 2.4 shows the obtained temperature profile along the collision axis, where the horizontal axis represents the distance from the southern peak (region 2 in figure 2.1). The north and south directions are positive and negative, respectively. The temperature is the highest in the region 2, where the southern main X-ray peak is located.

Table 2.3: Best fit parameters for the XIS spectra of the region presented in figure 2.1

Region Number	kT (keV)	abundance	$\chi^2/d.o.f$
1	$7.31^{+0.75}_{-0.67}$	$0.24^{+0.08}_{-0.08}$	174.37/189
2	$8.53^{+0.52}_{-0.31}$	$0.18^{+0.03}_{-0.03}$	819.42/739
3	$8.25^{+0.27}_{-0.26}$	$0.16^{+0.03}_{-0.03}$	1043.07/925
4	$7.81^{+0.29}_{-0.29}$	$0.13^{+0.03}_{-0.03}$	908.03/814
5	$7.13^{+0.46}_{-0.50}$	$0.16^{+0.04}_{-0.04}$	461.81/398
6	$5.76^{+0.75}_{-0.63}$	$0.22^{+0.11}_{-0.10}$	116.45/126
7	$3.66^{+0.93}_{-0.66}$	0.2(fixed)	67.93/80

2.2.3 Candidate shock regions

In this subsection, we investigate the temperature structure around the candidate shock region. The spectral model used in the fitting is the same as in subsection 2.2.2. We search for point sources with XMM-Newton data, whose spatial resolution is better than Suzaku. In order to reduce contamination and CXB systematic errors, $1'$ radius circular regions centered by a position of a point source whose flux is more than 1.0×10^{-14} erg cm^{-2} s^{-1} are excluded and shown in figure 2.5 by green circles. Assuming that a shock is located at the Toothbrush relic outer edge, we chose regions as shown in figure 2.5 by red boxes, whose box size is $2' \times 8'$, where the outermost region is a $2.'5 \times 6.'5$. Ogrean et al. (2013) [63] suggested a temperature gradient along the relic's long axis. To investigate how this affects the Mach number estimation, R3 region is divided into two $2' \times 4'$ boxes as in figure 2.5.

It is well known that CXB has the spatial fluctuations. This can be modeled as $\sigma_{\rm CXB}/I_{\rm CXB} \propto \Omega_e^{-0.5} S_c^{0.25}$, where Ω_e and S_c are the effective solid angle and upper cutoff flux of a point source, respectively. From the HEAO-I A2 results, Shafer (1983) [87] reported that

$$\frac{\sigma_{\rm CXB}}{I_{\rm CXB}} = 2.8\% \left(\frac{\Omega_{\rm e}}{15.8 \text{ deg}^2} \right)^{-0.5} \left(\frac{S_{\rm c}}{8 \times 10^{-11} \text{ erg s}^{-1} \text{ cm}^{-2}} \right)^{0.25}. \quad (2.3)$$

We assumed the upper cutoff flux of $S_c = 1.0 \times 10^{-14}$ erg cm^{-2} s^{-1}. From

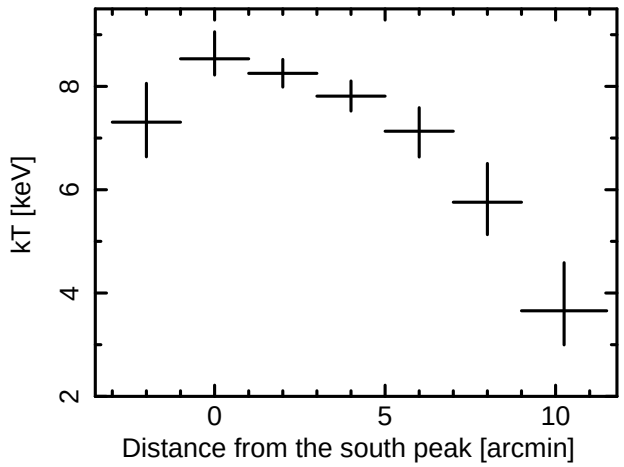

Figure 2.4: Temperature profile along the collision axis.
The horizontal axis shows the angular distance from the southern main X-ray peak (region 2 in figure 2.1 with the highest temperature), where the north and south directions are positive and negative, respectively.

the size of each region, the calculated CXB fluctuation at the 90 % confidence level are shown in table 2.4. In addition, it is reported that the reproducibility of NXB was 6.0 % and 12.5 % for XIS FI and BI at the 90 % confidence level, respectively [101]. We estimate CXB and NXB systematic errors taking into account of these uncertainties.

Figure 2.6 shows the spectra of pre- (R2) and post-shock (R3) regions fitted with the above-mentioned model. The ICM component of the pre-shock region is clearly detected over the CXB. The resultant best-fit parameters are listed in table 2.4, where the first, second and third errors are statistical, CXB systematic, and NXB systematic errors at 90 % confidence level, respectively. The temperature profile is shown in figure 2.7, where the horizontal axis represents the angular distance from the relic outer edge, and the positive and negative is inward and outward directions from the relic outer edge. We found a temperature drop at the relic outer edge, and also confirmed the temperature gradient in the relic region along the relic's longer axis.

Ogrean et al. (2013) also suggest that the shock is elongated towards the west of the relic [63]. We investigate the temperature structure around there. The regions used in this analysis are displayed in cyan annuli (west shock

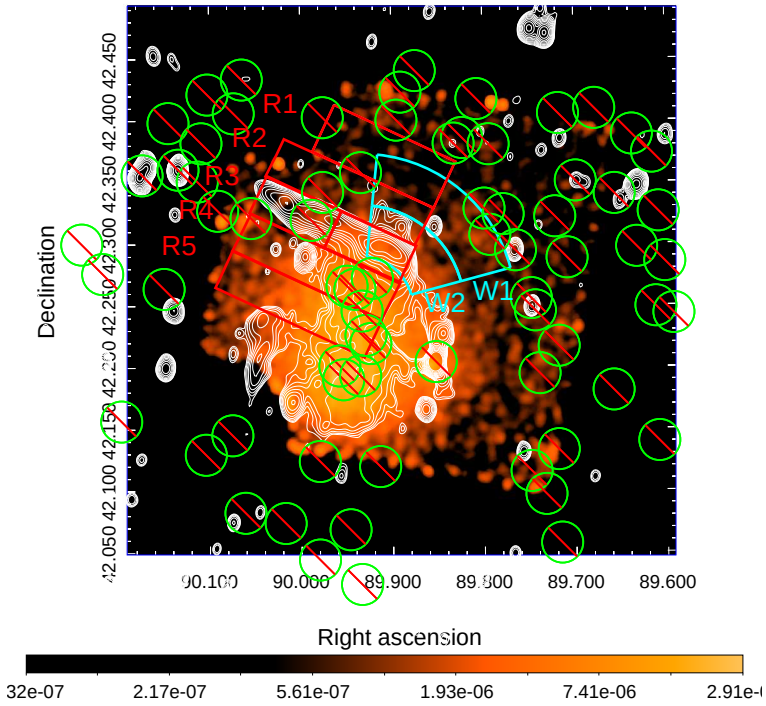

Figure 2.5: Candidate shock regions

Regions utilized in the candidate shock analysis. Red boxes and cyan annular are regions for the analysis of the relic shock and west shock, respectively. Green circles are excluded regions of a point source.

Table 2.4: Fitting results of the relic shock regions.

Region Number	kT (keV)[1)]	abundance[1)]	$\chi^2/d.o.f$	$\Delta_{\rm CXB}$ (%)[2)]
R1	$3.06^{+1.74+1.05+0.57}_{-0.94-0.92-0.53}$	0.2(fixed)	24.06/31	38
R2 (pre-shock)	$4.07^{+0.99+0.69+0.40}_{-0.68-0.68-0.42}$	0.2(fixed)	72.46/66	33
R3 (post-shock)	$6.10^{+0.60+0.22+0.13}_{-0.58-0.24-0.18}$	0.2(fixed)	205.76/161	35
R4	$5.98^{+0.51+0.16+0.10}_{-0.50-0.16-0.14}$	$0.24^{+0.07+0.00+0.00}_{-0.07-0.00-0.01}$	185.74/178	38
R5	$8.06^{+0.46+0.07+0.07}_{-0.44-0.07-0.09}$	$0.16^{+0.05+0.00+0.00}_{-0.05-0.00-0.00}$	457.43/419	32
R3east	$2.70^{+1.22+0.96+0.38}_{-0.62-0.77-0.21}$	0.2(fixed)	17.87/17	59
R3west	$6.82^{+1.02+0.47+0.34}_{-0.55-0.21-0.11}$	0.2(fixed)	187.50/170	41

[1)] The first, second, and third errors are statistical, CXB systematic, and NXB systematic, respectively.
[2)] CXB fluctuations at the 90 % confidence level estimated with equation (2.3).

region) in figure 2.5. We fit the spectrum of each region in the same ways as in above-mentioned. The resultant best-fit parameters are listed in table 2.5, and the temperature profile is shown in figure 2.8 We also see a clear temperature drop across the expected shock front.

2.2.4 Candidate cold front regions

van Weeren et al. (2016) suggested that there are the very hot ICM with $kT \sim 15$ keV and a cold front in the south of the southern subcluster's core [107]. In order to check these, we chose the regions as in figure 2.9, whose radii from the southern peak are $1'$, $2.'5$, and $4'$ from the southern peak. The estimated temperature map in van Weeren et al. (2016) show that the temperature of eastside is higher than the westside's one. Taking account of this, we divide the region of $1' - 2.'5$ into two annular as in figure 2.9. In this spectral analysis, we used the abundance table of Asplund et al. (2009)[11]. The spectral model used in this fitting is the same as in subsection 2.2.2. Table 2.6 shows the detailed results of the best-fit model and the temperature profile is shown in figure 2.10. The obtained temperature of southern core is 10.05 ± 0.37 at 1σ confidence level. This value is consistent with the result of

Table 2.5: Fitting results of the west shock regions.

Region Number	kT (keV)[1)]	abundance	$\chi^2/d.o.f$	$\Delta_{\rm CXB}$ (%)[2)]
W1 (pre-shock)	$3.76^{+0.73+0.49+0.31}_{-0.63-0.66-0.54}$	0.2 (fixed)	89.32/83	30
W2 (post-shock)	$6.16^{+0.62+0.25+0.13}_{-0.60-0.28-0.19}$	0.2 (fixed)	173.22/158	34

[1)] The first, second, and third errors are statistical, CXB systematic, and NXB systematic, respectively.
[2)] CXB fluctuations at the 90 % confidence level estimated with equation (2.3).

van Weeren et al. (2016) ($kT = 9.00 \pm 0.28$) considering the 3σ errors. Our results suggest that there is the high temperature ICM of $kT \sim 10$ keV around the southern core. Although we did not find a significant temperature jump between the regions ahead ($1' - 2.'5_{\rm East}$) and behind ($0' - 1'$) of the candidate cold front, the temperature increases toward the outside.

2.2.5 Search for the non-thermal inverse Compton X-rays

The same electron population attributed to the radio relic are expected to emit non-thermal X-rays via the inverse Compton scattering of the CMB photons. In order to constrain this component, the spectra in the radio relic region (R3 in figure 2.5) are fitted by the following model:

$$constant * [apec_{\rm LHB} + wabs * (apec_{\rm MWH} + powerlaw_{\rm CXB} + apec_{\rm ICM} + powerlaw_{\rm IC})], \quad (2.4)$$

where $powerlaw_{\rm IC}$ represents the inverse Compton component. We fixed all the parameters of the background components ($apec_{\rm LHB}$, $apec_{\rm MWH}$, and $powerlaw_{\rm CXB}$) to the values derived from the background field in subsection 2.2.1. The temperature of the ICM component is fixed to the value obtained in the candidate shock region analysis ($kT = 6.10$ keV) because the inverse Compton component is most likely to be much weaker than the thermal ICM one. We fixed the photon index of the inverse Compton component to be 2.1 considering that van Weeren et al. (2012) reported that the integrated radio spectral index of the relic is 1.1. The fitting results are summarized

Table 2.6: Fitting results of the candidate cold front regions.

Region	kT (keV)[1)]	abundance[1)3)]	$\chi^2/d.o.f$	$\Delta_{\rm CXB}$ (%)[2)]
$0' - 1'$	$10.05^{+0.61+0.05+0.00}_{-0.60-0.05-0.00}$	$0.33^{+0.10+0.00+0.00}_{-0.10-0.00-0.00}$	413.11/404	66%
$1' - 2.'5$	$10.33^{+1.16+0.07+0.00}_{-0.84-0.07-0.00}$	$0.41^{+0.14+0.00+0.00}_{-0.14-0.00-0.00}$	312.71/272	48%
$2.'5 - 4'$	$9.22^{+1.49+0.21+0.00}_{-1.24-0.22-0.00}$	$0.38^{+0.24+0.00+0.00}_{-0.24-0.00-0.00}$	150.23/135	35%
$1' - 2.'5_{\rm East}$	$11.63^{+1.47+0.11+0.00}_{-1.24-0.12-0.00}$	$0.40^{+0.18+0.00+0.00}_{-0.18-0.00-0.00}$	239.61/225	54%
$1' - 2.'5_{\rm West}$	$8.91^{+0.80+0.10+0.00}_{-0.64-0.10-0.00}$	$0.40^{+0.12+0.00+0.00}_{-0.12-0.00-0.00}$	297.77/267	54%

[1)] The first, second, and third errors are statistical, CXB systematic, and NXB systematic, respectively.
[2)] CXB fluctuations at the 90 % confidence level estimated with equation (2.3).
[3)] The abundance table of Asplund et al. (2009) [11] is used.

in table 2.7. Though we did not detect the inverse Compton component, we obtained its upper limit. Considering both the statistical and systematic errors, we derive an upper limit of the inverse Compton component in 0.3-10 keV at the 90 % confidence level. The resultant upper limit on the flux is $F_{\rm IC} < 2.4 \times 10^{-13}$ erg s^{-1} cm^{-2} for the $2' \times 8'$ area.

2.3 Discussion

2.3.1 Temperature profile of collision axis

We compare the temperature profile of the galaxy cluster 1RXS J0603.3+4214 with that of typical relaxed clusters. First, Burns et al. (2010) reported the scaled temperature profile which is based on cosmological N-body + hydrodynamic simulation results [23]. The temperature and radius of profile are normalised by the mean temperature ($< kT >$) and virial radius (r_{200}), respectively. The scaled profile outside $0.2r_{200}$ is

$$\frac{kT}{< kT >} = A \left[1 + B\frac{r}{r_{200}}\right]^{\alpha}, \tag{2.5}$$

where the best-fit parameters are $A = 1.74 \pm 0.03$, $B = 0.64 \pm 0.10$, and $\alpha = -3.2 \pm 0.4$. We adopt the mean temperature of $< kT >= 7.8$ keV [63].

Table 2.7: Best fit parameters of the spectrum model with inverse Compton components.

components	kT (keV) or Γ	normalization[3)]
$apec_{\rm ICM}$	6.10 (fixed)[1)]	$3.67^{+0.64+0.37+0.15}_{-0.63-0.37-0.22} \times 10^{-2}$
$powerlaw_{\rm IC}$	2.1 (fixed)[2)]	$2.03^{+1.51+0.39+0.24}_{-1.51-0.39-0.19} \times 10^{-3}$
	$\chi^2/d.o.f$	200.88/161

[1)]The value obtained from spectral fitting of the relic post shock region summarized in table 2.4.
[2)] Photon index derived from the integrated radio spectral index [106].
[3)] Normalizations in the *apec* code and powerlaw component are written in the same way as in table 2.2.
The errors are represented as in table 2.4.

The virial radius is calculated from the following empirical relation [40]:

$$r_{200} = 2.77 \pm 0.02 h_{70}^{-1} {\rm Mpc} \frac{(kT/10 \text{ keV})^{1/2}}{E(z)}, \tag{2.6}$$

where h_{70} is the Hubble constant normalized by the value $H_0 = 70$ Mpc^{-1} km s^{-1} and $E(z) = [\Omega_0(1+z)^3 + 1 - \Omega_0]^{1/2}$. As a result, the obtained virial radius becomes $r_{200} = 2.21$ Mpc. Figure 2.11 shows the scaled temperature profile of our results (table 2.3). The obtained temperatures are higher than the value of the fitting function around $r \sim 0.7 r_{200}$, which might be owing to the heating by the merger shock, the disturbed shape of the gravitational potential, and/or the disturbed entropy distribution.

Next, we compare our results with a universal temperature profile obtained by Okabe et al. (2014) [67] from Suzaku X-ray and Subaru weak-lensing observations of four relaxed galaxy clusters. Okabe et al. (2014) reported the scaled temperature profile as follows:

$$\frac{kT}{kT_*} = \left(\tilde{r}_0^{-1} \frac{r}{r_{200}} \right)^{\frac{3}{5}\alpha - \frac{2}{5}\gamma} \left[1 + (\tilde{r}_0^{-1} \frac{r}{r_{200}})^{\beta} \right]^{-(\frac{2}{5}\delta - \frac{2}{5}\gamma + \frac{3}{5}\alpha)/\beta}, \tag{2.7}$$

where $\alpha = 1.16^{+0.17}_{-0.12}$, $\beta = 5.52^{+2.87}_{-2.64}$, $\gamma = 1.82^{+0.28}_{-0.30}$, $\delta = 2.72^{+0.34}_{-0.35}$, and $\tilde{r}_0 =$

$0.45^{+0.08}_{-0.07}$. The normalization factor of the temperature is

$$kT_* = 1.27^{+0.24}_{-0.19}\mathrm{keV}\left[\frac{M_{200}E(z)}{10^{14}h_{70}^{-1}M_\odot}\right]^{2/3}, \tag{2.8}$$

where M_{200} is the total mass inside r_{200}. Though both M_{200} and r_{200} should be determined through direct mass measurements, such as gravitational lensing techniques ideally, we do not have available lensing data for this cluster. Therefore, we calculate M_{200} simply assuming that the mean density inside r_{200}, which is derived from equation (2.6), is 200 times the critical density of the universe. The critical density is

$$\rho_c = \frac{3H_0^3}{8\pi G}, \tag{2.9}$$

where G is a gravitational constant. We derive $M_{200} = 1.23 \times 10^{15} M_\odot$ using the following equation:

$$M_{200} = \frac{4}{3}\pi r_{200}^3 \times (200\rho_c). \tag{2.10}$$

As a result, we obtain $kT_* = 7.30$ keV from equation (2.8). Figure 2.12 shows a comparison of our results with the temperature profile of Okabe et al. (2014). It is clear that the measured temperatures are systematically higher than the universal profile for all radii. This suggests that the normalization determination dose not work very well, which is not so surprising considering that we did not use gravitational lensing data. The central part and outermost data could be marginally consistent with the universal profile, taking account of the errors in kT_*. Note that the our data shows a convex profile where as the universal profile is concave around $r \sim 0.7r_{200}$.

2.3.2 Candidate shock

We derive the Mach number (M_X) from the temperature ratio of the candidate shock region using the Rankine-Hugoniot relation as follows:

$$\frac{T_{\mathrm{post}}}{T_{\mathrm{pre}}} = \frac{5M_X^4 + 14M_X^2 - 3}{16M_X^2}, \tag{2.11}$$

where T_{pre} and T_{post} are the temperature of the pre- and post-shock regions, respectively, and we assume that the specific heat ratio $\gamma = 5/3$. Using

equation (2.11), the derived Mach number of Toothbrush relic is $M_X = 1.50^{+0.37+0.25+0.14}_{-0.27-0.24-0.15}$ with the temperatures of R2 and R3 regions. This means that $M_X = 1.50^{+0.28}_{-0.24}$ at 1σ confidence revel. On the other hand, the radio spectral index results indicate $M_{\rm radio} = 3.3 \sim 4.6$ on the assumption of a simple DSA theory [106]. Thus, our results show a clear discrepancy between them even including both statistical and systematic errors, which strongly suggests that a simple DSA theory dose not hold, at least for this object, and that there should be other parameters that control the shock acceleration. Recently, van Weeren et al. (2016) reported the $M_{\rm radio} = 2.8^{+0.5}_{-0.3}$ with deep LOFAR observations at low frequency. However, this value is still higher than our results.

Ogrean et al. (2013) suggests a temperature gradient along the long axis of Toothbrush relic [63], which is also confirmed in our data as shown in figure 2.7. This means that the temperature of the R3 region could be underestimated, which leads to the underestimation of the Mach number. Considering this, we derived the Mach number using the R2 and R3 west region temperatures. The resultant Mach number becomes $M_X = 1.67^{+0.43+0.27+0.16}_{-0.28-0.25-0.15}$. Therefore, this effect is quite limited and the discrepancy between the radio and our results still remains. We search for a corresponding temperature gradient in the pre-shock region, dividing R2 region into east and west regions and performing the spectral analysis as in subsection 2.2.2. However, no significant temperature gradient is found because of the poor statistics.

Considering Suzaku's point spread function (PSF), whose half power diameter is $\sim 2'$. The temperature ratio between the neighboring regions could be somewhat underestimated. In particularly, because of the contamination from the hotter and brighter post-shock region, the temperature of the cooler and fainter pre-shock region would be overestimated. In order to check this, we measured the temperature of the region $1'$ ahead of the Toothbrush relic outer edge. The obtained temperature is $kT = 2.85^{+0.93+0.76+0.43}_{-0.58-0.61-0.49}$ keV. This is ~ 1.2 keV lower than the pre-shock temperature. This temperature decline is partly because of the global temperature decline trend shown in figure 2.3, and partly because of the contamination from the post-shock region. In other words, the overestimation of the pre-shock region temperature due to the PSF should be ~ 1 keV at most, which could be comparable to the statistical and

CXB systematic errors at most.

If the ICM components that are not directly associated with the shock but have different temperature are accidentally located along the line of sight, we would have incorrect temperature ratio. We fit the spectra with a two temperature ICM model to investigate this possibility, but the fitting results did not improve significantly. At least, we do not have compelling evidence to introduce a two temperature ICM model. Also, this unexpected temperature difference could be a result of the complicated dynamical history of the cluster. Indeed, both the temperature gradient along the longer axis of the relic and the peculiar linear shape of the Toothbrush suggest that the galaxy cluster 1RXS J0603.3+4214 dose not undergo a simple bimodal merger. Brüggen et al.(2012) [22] suggested a triple merger scenario, where the interaction of multiple shocks generates a linear-shape shock front like the Toothbrush relic.

The spectrum has a memory of the past acceleration history in a re-acceleration scenario [20], where the electrons in the relic have already accelerated once somewhere. In other words, the present shock Mach number alone cannot determine the relic spectrum. If the past acceleration process is relevant to higher Mach number shocks such a virial shocks [82, 108], relic shock Mach number would be lower than what is expected from radio observations. A non-linear acceleration model [55], where the shock structures are modified by the interactions between the thermal ICM and accelerated non-thermal particles, is another possibility to explain this kind of discrepancy. The relation between the Mach number and radio spectrum index is not simple and will depend on the details of the modeling.

For the western shock region, a similar analysis is also performed and the obtained Mach number becomes $M_X = 1.63^{+0.32+0.20+0.12}_{-0.28-0.27-0.22}$ at the 90% confidence level. This Mach number is consistent with the XMM-Newton results ($M = 1.7^{+0.41}_{-0.42}$ at the 1σ confidence level) based on X-ray surface brightness analysis [63]. Generally, the temperature measurement is less seriously affected by the line of sight structures, while some kind of three dimensional modeling is necessary to get the information of the density structure from the X-ray surface brightness distribution. On the other hand, our result could be affected by Suzaku's moderate spatial resolution, as mentioned above. Although it is probable that a temperature difference and Mach number are un-

derestimated to a certain extent, we obtained results consistent with Ogrean et al. (2013) in an independent way.

2.3.3 Magnetic field strength in the radio relic

We constrain the magnetic field strength in the relic from the comparison of the radio synchrotron and an inverse Compton X-ray flux [81]. The following procedure is a similar way as in Sugawara et al. (2009) [93]. The typical energy ($h\nu'$) of photons scattered via inverse Compton by electrons with energy $\gamma m_e c^2$ is

$$h\nu' = \frac{4}{3}\gamma^2 h\nu, \tag{2.12}$$

where $h\nu$ is the energy of photon before scattering and γ is the electron's relativistic Lorentz factor. The typical CMB photon energy at $z = 0.225$ is

$$h\nu = 2.82kT_0(1+z) = 7.1 \times 10^{-4} \text{ eV}, \tag{2.13}$$

where $T_0 = 2.725$ K is the temperature of the CMB at $z = 0$. Therefore, the range of the electron's relativistic Lorentz factor corresponding to the $0.3-10$ keV inverse Compton X-ray is

$$5.3 \times 10^2 < \gamma < 3.0 \times 10^3. \tag{2.14}$$

On the other hand, assuming a homogeneous pitch angle distribution, the synchrotron critical frequency emitted by electrons with magnetic field strength B is

$$\left(\frac{\nu_c}{\text{MHz}}\right) = 3.3 \times 10^2 \left(\frac{\gamma}{10^4}\right)^2 \left(\frac{B}{\mu\text{G}}\right). \tag{2.15}$$

Thus, the typical synchrotron frequency range emitted by the electron in the energy range of equation (2.14) is

$$9.1 \times 10^{-1} \left(\frac{B}{\mu\text{G}}\right) < \left(\frac{\nu_c}{\text{MHz}}\right) < 3.0 \times 10 \left(\frac{B}{\mu\text{G}}\right). \tag{2.16}$$

van Weeren et al. (2012) [106] reported that the radio flux of the Toothbrush relic is 319.5 mJy at 1.382 GHz and that the spectral index is $\alpha = 1.1$. Therefore, the radio flux corresponding to the energy range of 0.3-10.0 keV inverse Compton X-ray is

$$F_{\text{sync}} = 2.7 \times 10^{-14} \left(\frac{B}{\mu\text{G}}\right)^{-0.1} \text{erg s}^{-1} \text{ cm}^{-2}, \tag{2.17}$$

with a monochromatic approximation for a single electron's spectrum and on the assumption of a single power-law electron energy distribution.

It is well known that the flux of the synchrotron radiation and inverse Compton scattering of CMB photons from the same electron population has the following relation:

$$\frac{F_{\rm IC}}{F_{\rm sync}} = \frac{U_{\rm CMB}}{U_{\rm mag}} = \frac{U_{\rm CMB}}{B^2/8\pi}, \tag{2.18}$$

where $U_{\rm mag}$ and $U_{\rm CMB}$ are the energy density of the magnetic field and CMB photons, respectively. Here, the energy density of the CMB photons at $z = 0.225$ is

$$\begin{aligned} U_{\rm CMB} &= 4.22 \times 10^{-13}(1+z)^4 \text{ erg cm}^{-3} \\ &= 9.5 \times 10^{-13} \text{ erg cm}^{-3}. \end{aligned} \tag{2.19}$$

With this value, comparing the above-mentioned $F_{\rm sync}$ and the obtained upper limit of $F_{\rm IC}$, the lower limit of the magnetic field strength in the Toothbrush relic becomes $B > 1.6$ μG. This result is consistent with the equipartition magnetic field energy, $B_{\rm eq} = 9.2$ μG [106]. Note that our results are free from the assumption of energy equipartition between cosmic ray electrons and magnetic field.

The upper limit on the inverse Compton flux could be sensitive to the temperature determination of the thermal ICM component. We checked how the upper limit on the inverse Compton flux is affected by the temperature changes of the ICM component in the spectral analysis. In case of a 1 keV increase and decrease of the ICM temperature, the obtained upper limits of the inverse Compton flux and the derived lower limits of magnetic field strength are summarized in table 2.8. A 1 keV increase and decrease of the ICM temperature cause a 24% increase and 27% decrease of the upper limit flux, respectively. These also result in a 12% decrease and 12% increase in the lower limit of the magnetic field strength, respectively. It seems odd at first glance that the temperature increase (or decrease) of the ICM cause an increase (or decrease) of the inverse Compton component. The best fit values and statistical errors of inverse Compton component normalization are less sensitive to the ICM temperature change. On the other hand, the systematic errors

are more sensitive and become larger (or smaller) when the ICM temperature becomes higher (or lower), which is the main factor governing the resultant upper limit flux. At any rate, magnetic field strength of $\sim$ μG level are still inferred.

We also checked how the results are affected by the radio spectral index changes. In case of the 0.1 increase and decrease of the absolute value of the radio spectral (and X-ray photon) index, the obtained upper limits of the inverse Compton flux and the derived lower limits of magnetic field strength are also summarized in table 2.8. The 0.1 increase and decrease of the absolute value of the radio spectral (and X-ray photon) index cause a 31% and 62% decrease of the upper limit flux, respectively. These cause a 50% increase and 19% decrease of the lower limit of the magnetic field strength, respectively. Note that the range of electrons attributed to the observed synchrotron radiation is most likely higher than that of the inverse Compton component in our analysis. Although the range of the Lorentz factor of electrons attributed to 0.1-1 GHz synchrotron radiation is $5.5\times10^3(B/\mu\mathrm{G})^{-0.5} < \gamma < 1.7\times10^4(B/\mu\mathrm{G})^{-0.5}$, that to the 0.3-10 keV inverse Compton component is $5.3 \times 10^2 < \gamma < 3.0 \times 10^3$ as discussed before. Fixing the normalization in the radio observation range, an increase (or decrease) of the absolute value of the radio spectral index causes an increase (or decrease) of the synchrotron flux corresponding to the inverse Compton component, which results in an increase (or decrease) of the lower limit on the magnetic field strength. In general, the above results all indicate a magnetic field at the $\sim \mu$G level. However, if the radio spectrum is not a single power-law, this might not be the case because we rely on the extrapolation of the synchrotron spectrum. Lower frequency radio and higher energy X-ray observations are crucial in this regard.

2.3.4 Energy densities in the radio relic region

From our results, we estimate the energy densities of the thermal ICM, non-thermal electrons, and magnetic field, which are basic and crucial parameters for radio relic studies. For simplicity, the radio relic region is assumed to be a cylinder whose radius and height are 868 kpc and 434 kpc, respectively. The estimated electron number density of the thermal ICM in the radio relic region

Table 2.8: Upper limits of the inverse Compton component and lower limits of the magnetic field strength.

fixed parameters	$F_{\rm IC}$ [erg s^{-1} cm^{-2}]	B [μG][1)]
$kT = 6.10$ keV		
$\Gamma = 2.1$	$< 2.42 \times 10^{-13}$	> 1.6
$kT = 5.10$ keV		
$\Gamma = 2.1$	$< 1.76 \times 10^{-13}$	> 1.8
$kT = 7.10$ keV		
$\Gamma = 2.1$	$< 3.00 \times 10^{-13}$	> 1.4
$kT = 6.10$ keV		
$\Gamma = 2.0$	$< 1.66 \times 10^{-13}$	> 2.4
$kT = 6.10$ keV		
$\Gamma = 2.2$	$< 9.04 \times 10^{-13}$	> 1.3

[1)] The lower limit of the magnetic field strength.

becomes $n_e = 3.54 \times 10^{-4}$ cm^{-3} from the normalization of the $apec_{\rm ICM}$ model (table 2.7). With this value and the temperature of this region ($kT = 6.10$ keV), we derive the energy density of thermal ICM using following equation:

$$U_{\rm th} = \frac{3}{2}\frac{n_e kT}{\mu}, \tag{2.20}$$

where μ is the mean molecular weight. Assuming $\mu = 0.6$, the obtained value is $U_{\rm th} = 8.6 \times 10^{-12}$ erg cm^{-3}. Next, we estimate the energy density of the magnetic field from following equation:

$$U_B = \frac{B^2}{8\pi}. \tag{2.21}$$

With the obtained lower limit of magnetic field strength ($B > 1.6$ μG), the energy density of the magnetic field is $U_{\rm mag} > 1.0 \times 10^{-13}$ erg cm^{-3}. As a result, $U_{\rm mag}/U_{\rm th} > 1.2 \times 10^{-2}$. This means that the magnetic field energy could be more than a few percent of the thermal one and that the ICM evolution and structures could be somewhat affected by the magnetic field. From the upper limit of the inverse Compton component, the energy density of the relativistic

electrons corresponding to 0.3-10 keV X-ray band (or, $5.3 \times 10^2 < \gamma < 3.0 \times 10^3$) becomes $U_{\rm e} < 3.6 \times 10^{-14}$ erg cm^{-3}. Therefore, $U_{\rm e}/U_{\rm th} < 4.3 \times 10^{-3}$, although we did not include the contribution from lower energy electrons in these calculation, which could be dominant in the energy density of the non-thermal electron populations.

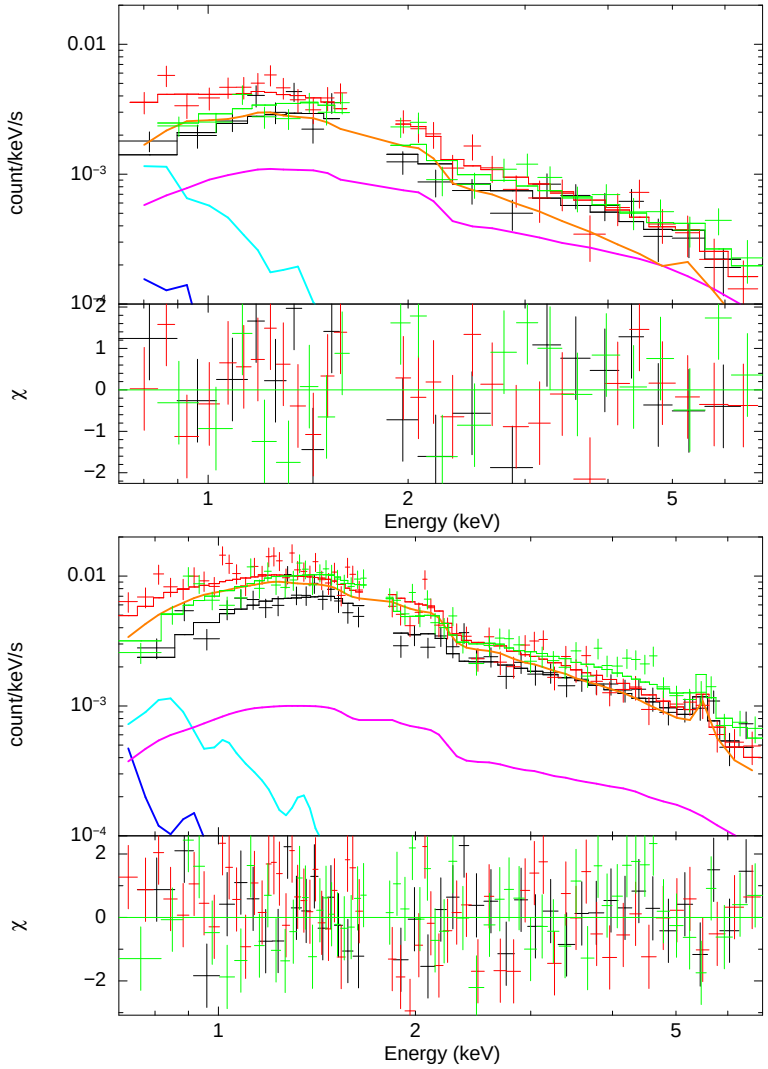

Figure 2.6: XIS spectra of the pre- and post-shock regions.
The XIS spectra of the pre- (R2; top) and post-shock (R3; bottom) regions of the relic shock fitted with the model described in the text. The black, red, and green crosses show the spectra of XIS0, XIS1, and XIS3, respectively. The total spectra of the best-fit model are also plotted as solid histograms. The blue, light blue, magenta, and orange solid histograms represent the LHB, MWH, CXB, and ICM components, respectively. The ICM component is clearly detected over the CXB.

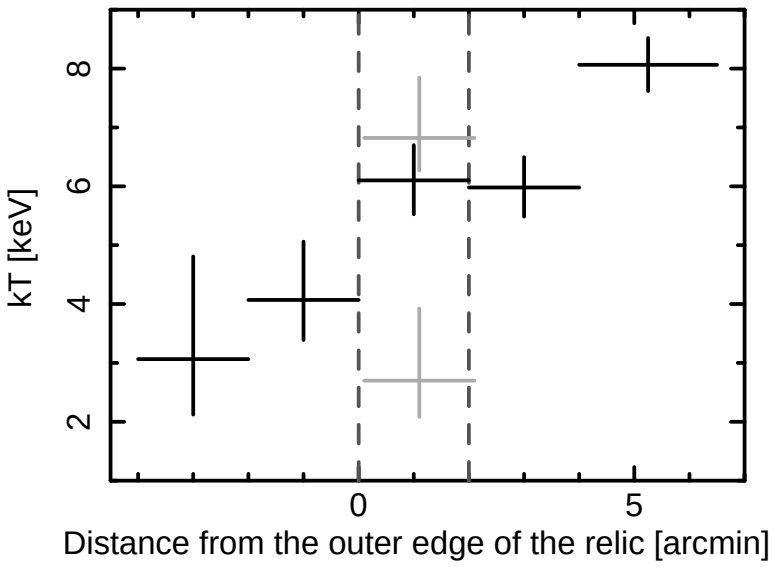

Figure 2.7: Temperature profile across the Toothbrush relic.
The temperature profile across the relic shock regions. Horizontal axis represents the angular distance from the relic outer edge. The positive and negative is inward and outward directions from the relic outer edge. Black crosses show the results from regions R1, R2, R3, R4, and R5. Light gray crosses show the results when the region R3 (post shock) is divided into R3east and R3west regions. Only statistical errors are displayed. The positions of the inner and outer edges of the relic are displayed by dark gray dotted lines.

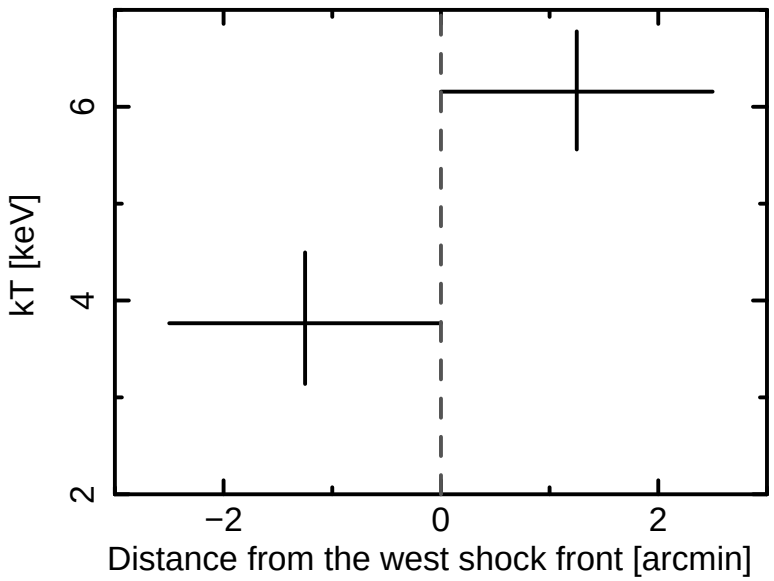

Figure 2.8: Temperature profile of the west shock regions.
The temperature profile across the west shock regions. Horizontal axis represents the angular distance from the possible shock front. Inward and outward directions from the possible shock front are positive and negative, respectively. (see cyan annuli in figure 2.5). Only statistical errors are displayed.

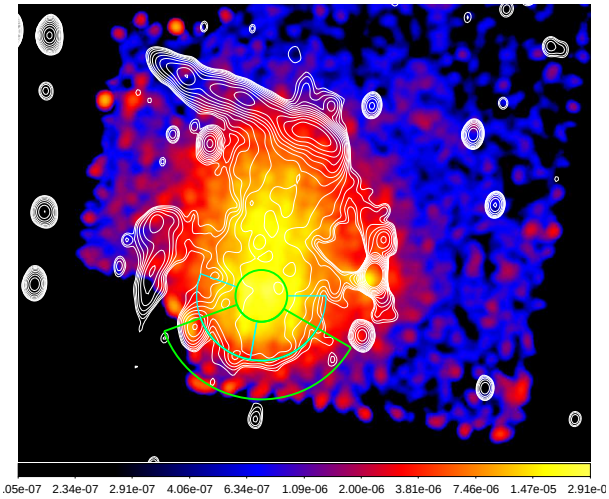

Figure 2.9: Candidate cold front regions
Green annular are regions for the analysis of the cold front, whose radii from the southern peak are $1'$, $2.'5$, and $4'$ from the southern peak. Light blue regions are divided the region of $1' - 2.'5$ into two annular.

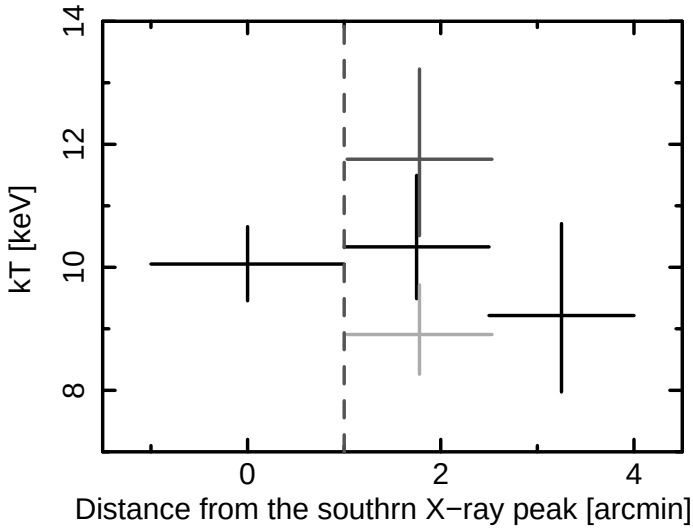

Figure 2.10: Temperature profile of the candidate cold front region Horizontal axis represents the distance from the southern X-ray peak. The black crosses are results of green regions in figure 2.9. The dark and light gray crosses are the light blue annular region of east and west side, respectively. The positions of the candidate cold front is displayed by dark gray dotted lines.

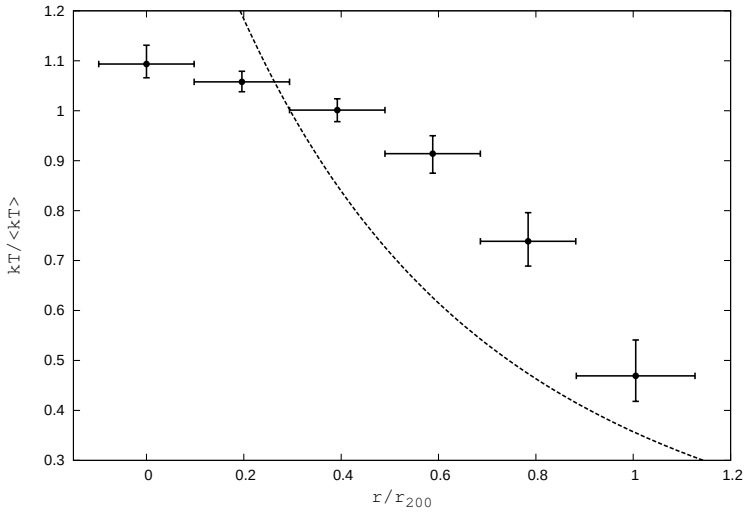

Figure 2.11: Comparison of temperature profile along the collision axis with the scaled profile of Burns et al. (2010) (Toothbrush cluster).
Comparison of the scaled temperature profile along the collision axis toward the north with a fitting function for relaxed clusters proposed by Burns et al. (2010)[23], which is based on cosmological N-body + hydrodynamical simulation results. The temperature and radius are normalized by the mean temperature and virial radius, respectively. Crosses and dotted lines represent our results and the fitting function, respectively. The temperatures are higher than the values of fitting function around $r \sim 0.7 r_{200}$, which might be because of the heating by the merger shock, disturbed shape of the gravitational potential, and/or disturbed entropy distribution.

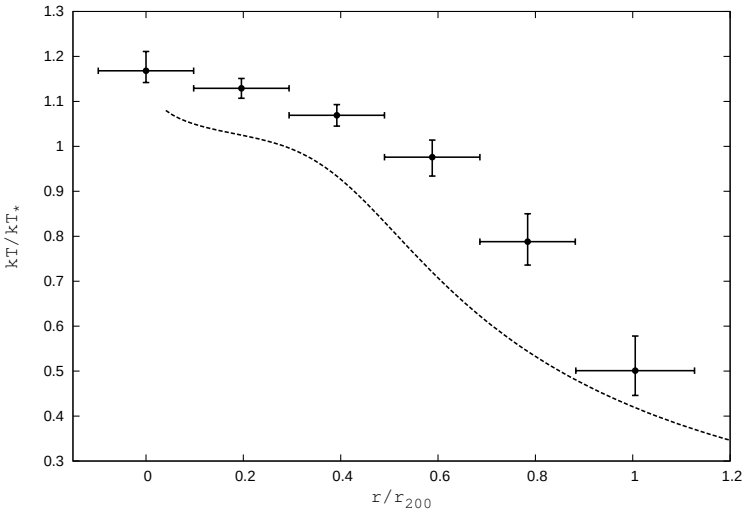

Figure 2.12: Comparison of temperature profile along the collision axis with the scaled profile of Okabe et al. (2014) (Toothbrush cluster).
Comparison of the scaled temperature profile along the collision axis toward the north with a universal temperature profile obtained from Suzaku X-ray and Subaru weak-lensing observations [67]. Crosses and dotted lines represent our results and the universal profile, respectively. Clearly, the measured temperatures are systematically higher than the universal profile in all radii, though the central part and outermost data could be marginally consistent with the universal profile taking account of the errors of kT_*. Note that the our data shows a convex profile whereas the universal profile is concave around $r \sim 0.7 r_{200}$.

Chapter 3

Galaxy Cluster RXC J1053.7+5453

The galaxy cluster RXC J1053.7+5453 ($z = 0.0704$) is known to host a radio relic. The radio relic is located at the distance of 524 kpc ($\sim 6'$) from the X-ray peak toward the west. Its X-ray luminosity with ROSAT is $L_{\mathrm{X}[0.1-2.4\mathrm{keV}]} = 0.96 \times 10^{44}$ erg s^{-1} [78] and the expected temperature from $L_{\mathrm{X}} - kT$ relation is $kT \sim 3$ keV [30]. This temperature is rather low for clusters with radio relics. However, there is no direct temperature measurement for this cluster. According to the Sloan Digital Sky Survey (SDSS) data, the velocity dispersion of the member galaxies is 665^{+51}_{-45} km s^{-1} and the virial radius is $r_{200} = 1.52$ Mpc [1], which is defined as the radius within which the mean density becomes 200 times of the critical density of the universe. From the radio observation, van Weeren et al. (2011) reported that the relic length and the radio flux density are 600 kpc and $S_{1382\ \mathrm{MHz}} = 15 \pm 2$ mJy, respectively [105]. There is no observational information about the radio spectra of this relic.

We observed a field around the radio relic in galaxy cluster RXC J1053.7+5453 with Suzaku for spectral analysis. In addition, we used Chandra archive data for surface brightness and the point sources removal, because the Advanced CCD Imaging Spectrometer (ACIS) has high spatial resolution. Figure 3.1 shows a ROSAT image of RXC J1053.7+5453 in 0.1-2.4 keV band. The yellow and light blue boxes show the FOVs of the Chandra ACIS and Suzaku

XIS observations. The white dashed circle shows the virial radius of RXC J1053.7+5453 ($r_{200} = 18.'8$).

In this chapter, we used canonical cosmological parameters of $H_0 = 70$ km s^{-1} Mpc^{-1}, $\Omega_0 = 0.27$, and $\Lambda_0 = 0.73$. At the redshift of this cluster ($z = 0.0704$), $1'$ corresponds to 81 kpc. Unless otherwise stated, the errors correspond to 90% confidence level.

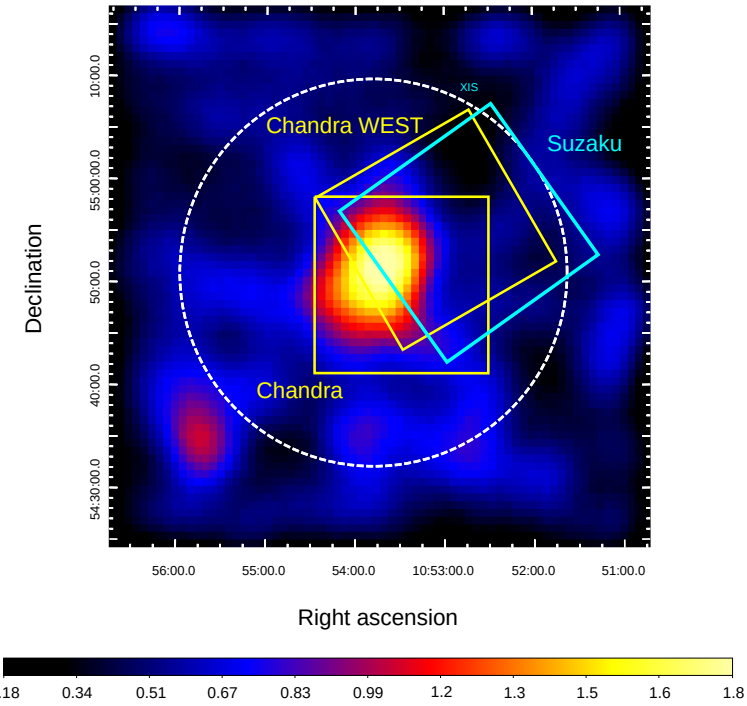

Figure 3.1: A ROSAT image of RXC J1053.7+5453.
A ROSAT image of RXC J1053.7+5453 in the 0.1-2.4 keV band. The image intensity is arbitrary unit and rms value of the image fluctuation is $\sigma = 0.48$. The yellow and light blue boxes show the FOVs of the Chandra ACIS and Suzaku XIS observations. The white dashed circle shows the virial radius of RXC J1053.7+5453 ($r_{200} = 18.'8$).

3.1 Observations and Data Reductions

We observed a field around the radio relic in galaxy cluster RXC J1053.7+5453 with Suzaku on 2014 November 01 - 03. This observation is one of the Suzaku AO9 Key projects. In addition, we used the Suzaku archive data of the Lockman Hole to estimate the background components. We used the data observed on 2009 June 12-14, which is the data of the field nearest to this cluster on sky plain among Lockman Hole observations of Suzaku. We used HEAsoft version 6.19 for these Suzaku data. The 20150312 calibration data files were adopted for these data. The XIS data were processed through default screening criteria (see section 2.1). Additionally, data obtained in the periods with geomagnetic cosmic-ray cut-off rigidity ($COR2$) > 8 GV were excluded. As a result, the effective exposure times became 71.6 ks and 63.8 ks for the cluster and Lockman Hole region, respectively. The additional processing for the NXB of XIS1 is applied in the same way as in section 2.1. We did not use the XIS0 segment A, which is damaged because of a micrometeorite accident [1)]. Figure 3.2 shows a 0.5-8.0 keV Suzaku XIS1 image with 1382 MHz radio contours [105]. RXC J1053.7+5453 was also observed with Chandra on 2013 June 22. Additionally, in order to search for point sources, we observed a field around the radio relic with Chandra on 2016 February 09. We used CIAO version 4.8 with the calibration files of CALDB version 4.7.0. The event files were reprocessed using the task "chandra_repro". The "lc_lean" algorithm was used to filter the soft proton flares, and the light curves were visually inspected to check for any residual flaring. As a result, the effective exposure times became 24.5 ks and 6 ks for the central and west fields, respectively. A Chandra image in the 0.5-2.0 keV band is shown in the figure 3.3. A summary of the Suzaku and Chandra observations is given in table 3.1.

3.2 Data Analysis and Results

For the spectral analysis of the Suzaku XIS data, RMFs and ARFs are generated in the way same as in section 2.2. The solar abundance are normalized to Asplund et al. (2009) [11].

[1)] http://www.astro.isas.ac.jp/suzaku/doc/suzakumemo/suzakumemo-2010-01.pdf

Table 3.1: The observational log of RXC J1053.7+5453 and Lockman Hole.

Name (Obs.ID)	(RA, Dec) (Deg)	Observation Date	Exposure (ks)[1)]
Suzaku			
RXC J1053.7+5453 (809120010)	(163.1807,+54.9140)	2014/11/01-03	71.6
LOCKMAN HOLE (104002010)	(162.9375,+57.2667)	2009/6/12-14	63.8
Chandra			
RXC J1053.7+5453 Center (15322)	(163.4148,+54.8296)	2013/6/22	24.5
RXC J1053.7+5453 WEST (17207)	(163.2642,+54.9077)	2016/2/09	6

[1)] Effective exposure time after data screening as described in the text.

3.2.1 Background components

We estimate the background components in a similar way as in section 2.2.1. The spectrum of the background region is fitted using the following model:

$$apec_{\rm LHB} + phabs * (apec_{\rm MWH} + powerlaw_{\rm CXB}). \quad (3.1)$$

We assumed $N_H = 6.05 \times 10^{19}$ cm^{-2} for the Galactic absorption [112]. The temperature of the LHB is fixed to be 0.08 keV, and the redshift and abundance of both LHB and MWH are also fixed to be zero and solar, respectively. We fixed the photon index of the CXB to $\Gamma = 1.4$ [52]. For the spectral fitting of the background components, we used energy bands of 0.7-7.0 keV (XIS0,3) and 0.6-7.0 keV (XIS1). However, the energy band of 1.7-1.8 keV was ignored, because the response matrix around the Si-K edge had residual uncertainties.

Figure 3.4 shows the spectra of the background field fitted with the above-mentioned model. Each color crosses and solid histograms same as in figure 2.3. Table 3.2 shows the detailed results of the best-fit model. The obtained temperature of the MWH component ($kT = 0.28^{+0.73}_{-0.07}$ keV) is consistent with the typical value ($kT \sim 0.3$ keV; [118])

Table 3.2: Best-fit background parameters for the XIS spectra of RXJ1053

Model Component	Parameter	Value
LHB	kT[1)]	0.08 (fixed)
	N[2)]	$5.03^{+9.53}_{-5.02} \times 10^{-2}$
MWH	kT[1)]	$0.28^{+0.73}_{-0.07}$
	N[2)]	$3.98^{+7.94}_{-3.34} \times 10^{-4}$
CXB	Γ[3)]	1.4 (fixed)
	N[4)]	$8.14^{+0.31}_{-0.30} \times 10^{-4}$
	$\chi^2/d.o.f$	120.96/110

[1)] Temperature of the each component in keV.
[2)] Normalization in the *apec* model for each component scaled with a factor $1/400\pi$.
$N = \frac{1}{400\pi} \int n_{\rm e} n_{\rm H} dV / [4\pi(1+z)^2 D_{\rm A}^2] \times 10^{-14}$ cm^{-5} arcmin^{-2},
where $D_{\rm A}$ is the angular diameter distance to the source.
[3)] Photon index of the power-law component.
[4)] Normalization in the power-law component in photons keV^{-1} cm^{-2} s^{-1} at 1 keV

3.2.2 Candidate shock regions

We investigate the temperature structure across the radio relic which is the candidate shock region. Assuming that a shock is located at the relic outer edge, we chose the regions as in the figure 3.2 by green annular marking. We search the point sources with Chandra data, whose spatial resolution is better than Suzaku. In order to reduce the contamination and CXB systematic errors, we exclude $2'$ radius circular region centered at the position of a point source (light blue circle in the figure 3.2) whose flux is more than 5×10^{-15}erg s^{-1} cm^{-2} (0.2-10 keV). We fit the spectrum of each region by the following model:

$$constant * [apec_{\rm LHB} + phabs * (apec_{\rm MWH} + powerlaw_{\rm CXB} + apec_{\rm ICM})], \quad (3.2)$$

where $apec_{\rm ICM}$ represents the ICM component. In the central region, we add $powerlaw_{\rm AGN}$ to the fitting model because there is an active galactic nucleus

(AGN) which cannot be excluded. Therefor, we fit the spectrum of the central region by the following model:

$$constant * [apec_{\rm LHB} + phabs * (apec_{\rm MWH} + powerlaw_{\rm CXB} + apec_{\rm ICM} + powerlaw_{\rm AGN})]. \quad (3.3)$$

We assume $N_H = 8.38 \times 10^{19}$ cm^{-2} for the Galactic absorption [112]. All parameters of the background components ($apec_{\rm LHB}$, $apec_{\rm MWH}$, and $powerlaw_{\rm CXB}$) are fixed to be the values derived from the background field in subsection 3.2.1. We fixed the redshift and abundance of the ICM components to be 0.0704 and 0.3 solar, respectively. For the spectral fitting of the ICM component, we used the energy band of 0.7-7.0 keV. However, we ignored the energy band of 1.7-1.8 keV, because the response matrix around Si-K edge had residual uncertainties. Systematic errors of the CXB and NXB are estimated in the same way as in subsection 2.3.2. We assume the upper cutoff flux of $S_c = 5 \times 10^{-15}$ erg s^{-1} cm^{-2}. With the size of each region, the calculated CXB fluctuations at the 90 % confidence level are shown in table 3.3. In addition, we assumed that the reproducibility of NXB is 4.9 % at the 90 % confidence level [101]. We estimated CXB and NXB systematic errors taking account of these uncertainties.

Figure 3.5 shows the spectra of each region fitted with the above-mentioned model. The ICM components of the outside region ($> 6'$) are fainter than the CXB component. The resultant best-fit parameters are listed in table 3.3. The first, second, and third errors are statistical, CXB systematic and NXB systematic errors, respectively. Considering only the statistical errors, the ICM component is marginally detected in the outside region of the radio relic ($9' - 15'$). However, the normalization of the $apec_{\rm ICM}$ is consistent with zero taking account of systematic errors. Figure 3.6 shows the temperature profile, where the horizontal axis represents the angular distance from the X-ray peak. The best-fit parameters (Γ and normalization) of the $powerlaw_{\rm AGN}$ in the central region are $\Gamma = 2.19^{+0.11}_{-0.13}$ and $norm = 1.66^{+0.32}_{-0.37} \times 10^{-2}$ photon keV^{-1} s^{-1} cm^{-2} and the flux of the AGN becomes 2×10^{-13} erg s^{-1} cm^{-2} (2.0-10 keV). Here, we also measured the temperature in the central region with the Chandra data. The obtained temperature becomes $kT = 1.52^{+0.53}_{-0.23}$ keV. This value is consistent with the Suzaku result

considering statistical errors. Though we did not find a significant temperature jump at the relic outer edge, the temperature decreases outward across the radio relic. If the shock is not located just at the relic outer edge, the temperature in the pre- and post-shock regions could be over- and underestimated, respectively. To check this, we measured the temperature of the yellow regions in the figure 3.2, which are $1'$ shifted outward compared with the green ones. The obtained temperatures are shown with light gray crosses in figure 3.6. This suggests that the shock could be located in the $6' - 9'$ region from X-ray peak and that the temperature in that region could be underestimated.

Table 3.3: Fitting results of regions across the relic.

Region	kT (keV)[1)]	normalization[2)]	$\chi^2/d.o.f$	$\Delta_{\rm CXB}$[3)]
$0 - 2'$	$1.38^{+0.17+0.04+0.01}_{-0.11-0.04-0.01}$	$4.38^{+1.37+0.14+0.02}_{-1.21-0.18-0.02} \times 10^{-2}$	118.17/105	35 %
$2' - 4'$	$1.64^{+0.50+0.41+0.01}_{-0.26-0.22-0.02}$	$1.44^{+0.32+0.31+0.01}_{-0.31-0.27-0.01} \times 10^{-2}$	8.1/13	65 %
$4' - 6'$	$1.56^{+0.23+0.16+0.04}_{-0.22-0.19-0.04}$	$3.67^{+0.71+0.87+0.08}_{-0.70-0.75-0.09} \times 10^{-3}$	38.93/33	25 %
$6' - 9'$	$1.15^{+0.44+0.72+0.04}_{-0.25-0.72-0.05}$	$5.83^{+3.94+4.20+0.03}_{-2.56-0.88-0.03} \times 10^{-4}$	36.02/21	19 %
$9' - 15'$	$1.08^{+0.32+0.00+0.00}_{-0.96-0.95-0.00}$	$1.95^{+1.79+6.89+0.39}_{-1.40-1.53-0.12} \times 10^{-4}$	44.73/51	11 %
$3' - 5'$	$1.58^{+0.21+0.20+0.02}_{-0.20-0.20-0.02}$	$7.05^{+1.17+1.33+0.10}_{-1.15-1.22-0.11} \times 10^{-3}$	27.81/31	32 %
$5' - 7'$	$1.60^{+0.36+0.18+0.05}_{-0.29-0.23-0.06}$	$2.17^{+0.63+0.73+0.08}_{-0.62-0.64-0.09} \times 10^{-3}$	38.93/31	24 %
$7' - 10'$	$1.08^{+0.51+0.00+0.00}_{-0.98-0.01-0.00}$	$2.62^{+2.18+2.08+0.22}_{-2.04-2.39-0.19} \times 10^{-4}$	47.08/35	17 %

[1)] The first, second, and third errors are statistical, CXB systematic, and NXB systematic, respectively.

[2)] CXB fluctuations at the 90 % confidence level estimated.

3.2.3 Analysis of the surface brightness edge regions

The Chandra image shows a surface brightness edge at a distance of $\sim 2'$ from the X-ray peak toward the west. We investigate the temperature and density structures of this region with Suzaku and Chandra, respectively. First, we extract the surface brightness profile from Chandra data and estimate the density ratio across the surface brightness edge. We exclude compact sources detected in the 0.5-7.0 keV band with CIAO task "wavdetect" using scales of 1, 2, 4, 8, 16 pixels and cutting at the 3σ level. We used PROFFIT [29] to extract and fit the profile. In order to extract the surface brightness profile,

we chose the green sector region in figure 3.3. The instrumental backgrounds are subtracted, and we used the energy band of 0.5-2.0 keV. We determine the sky background component by fitting a *constant* model for the outer region $(5.'0 - 7.'0)$ of the profile. The obtained value of the *constant* model becomes 4.37×10^{-7} count s^{-1} arcmin^{-2}. In the following analysis, the sky background component is fixed to this value. We assume the following density model:

$$n(r) = \begin{cases} n_1 \left(\frac{r}{R_f}\right)^{-\alpha_1}, & r < R_f \\ n_1 \frac{1}{C} \left(\frac{r}{R_f}\right)^{-\alpha_2}, & r > R_f \end{cases} \tag{3.4}$$

where $n(r)$ is the electron number density at the radius r, n_i $(i = 1,\ 2)$ is the density, and R_f is the radius of the location of the discontinuity in arcmin. α_i $(i = 1,\ 2)$ is powerlaw index, C is the density contrast (n_1/n_2) , and 1 and 2 denote the inside and outside regions, respectively. The profile and best-fit model $(\chi^2/d.o.f = 4.77/17)$ are shown in figure 3.7. The fitting results are summarized in table 3.4. We obtain a density contrast of $C = 2.44^{+2.50}_{-1.22}$ at the edge $(R_f = 2.'14^{+0.16}_{-0.15})$.

Table 3.4: Fitting results of the surface brightness profile.

α_1	α_2	R_f [1)]	
$0.46^{+0.51}_{-0.61}$	$1.66^{+1.15}_{-1.61}$	$2.14^{+0.16}_{-0.15}$	
C	S_0 [2)]	$const$ [3)]	$\chi^2/d.o.f$
$2.44^{+2.50}_{-1.22}$	$1.26^{+0.77}_{-0.58} \times 10^{-5}$	4.37×10^{-7} (fixed)	4.77/17

[1)]The radius of the location of the discontinuity in arcmin.
[2)]Normalization of the surface brightness units are count s^{-1} arcmin^{-2}.
[3)]The sky background component units are count s^{-1} arcmin^{-2}.

Secondly, we estimate the temperature structures around the surface brightness edge with Suzaku data. In this analysis, the used regions are displayed in green in figure 3.8. The radius of the annulus region is $2'$, $4'$, $6'$, $9'$, and $15'$, respectively. We fit the spectrum of each region by the model used in subsection 3.2.2. The resultant best-fit parameters are listed in table 3.5, and the temperature profile is shown in figure 3.9. We obtained the temperature ratio $T_1/T_2 = 0.72^{+0.24}_{-0.15}$ at the surface brightness edge, using the results of

Table 3.5: Spectral fitting results of regions across the surface brightness edge.

Region	kT (keV)[1)]	normalization[1)]	$\chi^2/d.o.f$	$\Delta_{\rm CXB}$ [2)]
$0-2'$	$1.34^{+0.19+0.01+0.00}_{-0.06-0.01-0.00}$	$4.39^{+0.96+0.11+0.00}_{-0.95-0.10-0.00}\times10^{-2}$	113.15/100	39 %
$2'-4'$	$1.85^{+0.40+0.23+0.03}_{-0.37-0.55-0.03}$	$1.66^{+0.26+0.21+0.01}_{-0.26-0.40-0.01}\times10^{-2}$	17.24/12	53 %
$4'-6'$	$1.71^{+0.61+0.27+0.00}_{-0.39-0.28-0.00}$	$2.72^{+0.86+1.07+0.09}_{-0.92-1.15-0.09}\times10^{-3}$	18.47/11	34 %
$6'-9'$	$1.72^{+1.88+1.51+0.21}_{-0.52-0.36-0.06}$	$1.59^{+0.70+0.90+0.10}_{-0.68-0.70-0.07}\times10^{-3}$	13.18/21	24 %
$9'-15'$	$0.41^{+1.06+0.02+0.01}_{-0.34-0.23-0.01}$	$8.75^{+4.48+2.89+0.60}_{-7.56-3.10-0.57}\times10^{-4}$	18.25/24	15 %

[1)] The first, second, and third errors are statistical, CXB systematic, and NXB systematic, respectively.
[2)] CXB fluctuations at the 90 % confidence level estimated.

the $0'-2'$ and $2'-4'$ regions. This indicates that the temperature increases outward across the edge.

3.2.4 Search for the non-thermal inverse Compton X-rays

We estimate the non-thermal X-ray components in a similar way as in section 2.2.5. To search the inverse Compton component, we selected the yellow region in figure 3.8, whose shape and size are similar to those for the radio flux measurement in van Weeren et al. (2011) [105]. First, we determine the thermal ICM temperature in this region by fitting the same spectral model as in subsection 3.2.2. We obtain the ICM temperature of $kT = 1.22$ keV. In the following fit, we fix the temperature of the ICM component to this value because the inverse Compton component is most likely to be much weaker than the thermal ICM one. Second, we fit the extracted spectra from the radio relic region by the following model:

$$constant * [apec_{\rm LHB} + phabs * (apec_{\rm MWH} + powerlaw_{\rm CXB} + apec_{\rm ICM} + powerlaw_{\rm IC})], \quad (3.5)$$

where $powerlaw_{\rm IC}$ represents the inverse Compton component. We fixed all parameters of the background components to the values derived from the background field in subsection 3.2.1. We consider two case for the $powerlaw_{\rm IC}$ photon index (Γ): 2.0 or 3.8. Note that there is no observational information

about the radio spectra of this relic. Assuming a simple DSA theory with the obtained Mach number (M_X) from our results, the photon index becomes $\Gamma = \alpha + 1 = 3.8$ (see subsection 3.3.2). However, this implies spectra much steeper than typical radio relics. On the other hand, a simple DSA dose not seem to hold for some relics. For example, in the Toothbrush cluster, the obtained $M_X \sim 1.5$ from Suzaku data as written in subsection 2.3.2 is significantly lower than the value estimated from the radio data [106]. If a similar situation occurs, Γ can be significantly smaller than 3.8. Therefore, we assume $\Gamma = 2.0$ as an extreme case. Systematic errors of CXB and NXB were taken into account in the same way as in the former analysis. The fitting results are summarized in table 3.6. Although we did not detect the inverse Compton component, we obtain an upper limit of the inverse Compton component. As a result, we obtain the upper limits on the flux of $F_{\rm IC} < 1.9 \times 10^{-14}$ erg s^{-1} cm^{-2} and $< 8.2 \times 10^{-11}$ erg s^{-1} cm^{-2} for $\Gamma = 2.0$ and $\Gamma = 3.8$, respectively, in 0.3-10 keV considering both the statistical and systematic errors for 4.50×10^{-3} deg^2 area.

Table 3.6: Spectral fitting results of the spectrum model with inverse Compton components.

components	kT (keV) or Γ	normalization[3)]
$apec_{\rm ICM}$	1.22 (fixed)[1)]	$8.36^{+3.95+1.42+0.42}_{-4.49-3.62-0.64} \times 10^{-4}$
$powerlaw_{\rm IC}$	2.0 (fixed)[2)]	$1.95^{+1.43\times10^{12}+2.17\times10^{12}+45.25}_{-0.81-1.95-1.95} \times 10^{-16}$ ($< 2.60 \times 10^{-4}$)[4)]
	$\chi^2/d.o.f$	28.23/19
$apec_{\rm ICM}$	1.22 (fixed)[1)]	$8.37^{+3.94+3.11+0.44}_{-3.81-3.64-0.65} \times 10^{-4}$
$powerlaw_{\rm IC}$	3.8 (fixed)[2)]	$1.11^{8.22\times10^{19}+0.92+47.61}_{-1.11-0.44-0.21} \times 10^{-20}$ ($< 8.22 \times 10^{-1}$)[4)]
	$\chi^2/d.o.f$	28.23/19

[1)] The value obtained from spectral fitting of the relic region in figure 3.8.

[2)] Assumed values for the photon index.

[3)] Normalizations in the *apec* code and powerlaw component are written in the same way as in table 3.2. The errors are represented as in table 3.3.

[4)] Upper limits of normalization.

3.3 Discussion

3.3.1 Temperature in the cluster central region

The $L_X - kT$ and $\sigma_v - kT$ relations are useful to investigate the physical status of galaxy clusters [114, 115, 62, 41]. We compare the temperature of our results in the central region with the expected one from the $L_X - kT$ and $\sigma_v - kT$ relations. First, Hilton et al. (2012) [41] reported a $L_X - kT$ relation as follows:

$$\log\left(E^{-1}(z)\frac{L_{\rm X}}{\rm erg\ s^{-1}}\right) = (44.67 \pm 0.09) + (3.04 \pm 0.16)\log\left(\frac{kT}{5\ \rm keV}\right) - (1.5 \pm 0.5)\log(1+z), \quad (3.6)$$

where $L_{\rm X}$ is X-ray luminosity in the 0.1-2.4 keV band, z is redshift and $E(z) = [\Omega_0(1+z)^3 + \Lambda_0]^{1/2}$. The expected temperature of this cluster is $kT = 3.04 \pm 1.08$ keV (1σ confidence level) with $L_{\rm X[0.1-2.4keV]} = 0.96 \times 10^{44}$ erg s^{-1} [78]. We also checked the expected temperature from another $L_X - kT$ relation. Novicki et al. (2002)[62] reported a $L_X - kT$ relation as follows:

$$\log\left(\frac{L_X}{10^{44}\ \rm erg\ s^{-1}}\right) = (2.82^{+0.32}_{-0.32})\log\left(\frac{kT}{\rm keV}\right) + (2.05^{+1.07}_{-1.06})\log(1+z) + (-1.13^{+0.22}_{-0.22}). \quad (3.7)$$

The expected temperature is $kT = 2.98 \pm 1.24$ keV and consistent with the above-mentioned one. Next, Wilson et al. (2016)[113] reported a $\sigma_v - kT$ as follows

$$\log\left(\frac{\sigma_{\rm v}}{1000\ \rm km\ s^{-1}}\right) = (0.02 \pm 0.05) + (0.86 \pm 0.14)\log\left(\frac{kT}{5\ \rm keV}\right) - (0.37 \pm 0.33)\log E(z), \quad (3.8)$$

where σ_v is the velocity dispersion. The expected temperature is $kT = 2.98 \pm 1.10$ keV (1σ confidence level) with $\sigma_v = 665^{+51}_{-45}$ km s^{-1} [1]. Again, we also checked the expected temperature from another $\sigma_v - kT$ relation. Wu et al. (1998)[114] reported a $\sigma_v - kT$ relation at $z < 0.1$ as follows:

$$\left(\frac{\sigma_v}{\rm km\ s^{-1}}\right) = 10^{2.57\pm0.03}\left(\frac{kT}{\rm keV}\right)^{0.49\pm0.05}. \quad (3.9)$$

The expected temperature is $kT = 3.28 \pm 0.28$ keV and consistent with the above-mentioned one. The expected temperatures from both relations are higher than our result at the center considering both statistical and systematic errors ($1.38^{+0.11}_{-0.07}$ keV; 1σ confidence level).

Cool core components should be removed in the analysis with the $L_X - kT$ and $\sigma_v - kT$ relations. If this point is not appropriately treated, we will have a lower temperature than expected. In fact, we see a weak temperature decrease towards the center. However, the cool core cluster usually have a centrally peaked distribution of metal abundance. We checked the abundance in the central region with the spectral fitting where the abundance is a free parameter. As a result, the obtained value ($Z = 0.13^{+0.14}_{-0.05} Z_\odot$) is not so high and we did not find such a feature in this cluster. Thus, our result is not likely due to a cool core in this cluster. As another possibility, it is likely that this cluster is not in dynamical equilibrium. Numerical simulations of cluster mergers show that the ICM temperature decreases due to an adiabatic expansion after the collision [46, 97]

The $\sigma_v - kT$ relation is derived from most galaxy clusters which are regarded as in dynamical equilibrium. If the cluster is in an adiabatic expansion phase after the collision, the velocity dispersion cloud be high, and the ICM temperature decreases. As a result, the expected temperature from the $\sigma_v - kT$ relation could be higher than the obtained temperature from observation. In fact, the measured temperature is lower than the expected one. Thus, the above results also suggest that this cluster might be in an adiabatic expansion phase after the collision.

3.3.2 Candidate shock

First, we compare the temperature profile of the galaxy cluster RXC J1053.7+5453 with that of typical relaxed clusters in a similar way as in subsection 2.3.1. As for this cluster, we compare our results with the temperature profile of Okabe et al. (2014). We adopt the mean temperature $< kT >= 1.38$ keV, which is the result of the central region. With equation (2.6), the derived virial radius of this cluster is $r_{200} = 1.00$ Mpc. Using equation (2.10) with the obtained r_{200} and equation (2.8), we obtain $M_{200} = 1.14 \times 10^{14} M_\odot$ and $kT_* = 1.41$ keV.

Figure 3.10 shows a comparison of our results with the temperature profile of Okabe et al. (2014) (equation (2.7) in subsection 2.3.1). Considering the errors, the obtained temperatures are consistent with the universal profile. We did not find a temperature jump around the relic ($0.5 - 0.8r_{200}$ in figure 3.10).

Although we did not find a significant temperature jump at the relic outer edge, figure 3.6 shows that the temperature decreases outward across the relic. This suggests the existence of shock. We derive the Mach number (M_X) from the temperature ratio of the shock candidate region using the Rankine-Hugoniot relation (equation (2.11)). We did not find a significant temperature jump at the relic outer edge where the shock is expected. From figure 3.6, if shock exists, it could be located $6' - 9'$ from the X-ray peak. Considering Suzaku's spatial resolution, the temperatures of the post-shock region could be underestimated. Therefore, we used the temperatures of regions $4' - 6'$ and $9' - 15'$ in the figure 3.2 for pre- and post-shock, respectively. As a result, we obtain $M_X = 1.44^{+0.48+0.14+0.03}_{-0.91-1.34-0.04}$, where the first, second and third errors are statistical, CXB systematic and NXB systematic at 90% confidence level, respectively. Some theoretical studies suggests that there are difficulties in particle acceleration at low Mach number shocks. For example, Vink and Yamazaki (2014) reported that shocks with Mack number less than $\sqrt{5}$ cannot accelerate particles [109]. Our results seem to contradict this because the existence of radio relics is evidence of the accelerated particles.

Assuming a shock with the above-mentioned Mach number exists at the radio relic, we can calculate the expected radio spectral index. We derive the shock compression (C) from the Mach number ($M_X \sim 1.4$) of the shock candidate region using the Rankine-Hugoniot relation as follows:

$$C \equiv \frac{\rho_2}{\rho_1} = \frac{4M^2}{M^2 - 3}, \tag{3.10}$$

where ρ_1 and ρ_2 are the density of pre- and post-shock region, respectively, and we assume that the specific heat ratio $\gamma = 5/3$. If the electrons are accelerated by DSA, the energy spectrum of the electrons becomes a power-law with index p;$(n(E)dE \propto E^{-p}dE)$, which is related to shock compression and given by $p = (C + 2)/(C - 1)$. Using equation (3.10), the obtained shock compression is $C = 1.6$. From this value, the power-law index becomes $p = 5.7$. This

mean that the spectral index of synchrotron radio at the injection region is $\alpha_{\rm inj} = (p-1)/2 = 2.3$. The integrated radio spectrum is steeper by 0.5 compared to $\alpha_{\rm inj}$ [73, 59]. As a result, $\alpha = \alpha_{\rm inj} + 0.5 = 2.8$. Thus, we used the photon index of $\Gamma = \alpha + 1 = 3.8$ in subsection 3.2.4.

If future radio observations provide us with the spectra, we might be able to get crucial information about the particle acceleration process around the radio relic in this cluster. Unfortunately, because no radio spectral information has been obtained so far, we cannot compare the Mach number of the shock from radio observations with our result. Radio observations at other frequency bands are necessary for this cluster.

In figure 3.9, the temperature profile south of the relic suggests a decrease of the temperature around $9'$ from the X-ray peak. The obtained Mach number is $M_X = 3.27^{+3.41+1.80+0.25}_{-1.76-0.46-0.08}$ using the temperature ratio of the regions $6' - 9'$ and $9' - 15'$. This is higher than the aforementioned value around the relic, which suggests that the Mach number varies along the radio relic, though the errors are large.

3.3.3 Surface brightness edge

We estimate the pressure profile across the surface brightness edge. This is important to investigate the physical states of the edge. In figure 3.7 and figure 3.9, we see that the density and temperature decreases and increases outward across the edge, respectively. This suggest that this structure is not associated with a shock. We calculate the pressure ratio (P_1/P_2) at the edge. Using our results about the density ratio ($n_1/n_2 = 2.44^{+2.50}_{-1.22}$) and temperature ratio ($kT_1/kT_2 = 0.72^{+0.24}_{-0.15}$) at the edge from Chandra and Suzaku data, the obtained pressure ratio becomes $P_1/P_2 = 1.76^{+1.89}_{-0.95}$.

In the X-ray image, cold fronts are seen as an edge-like structure. The density and the temperature are discontinuous but the pressure is continuous across a cold front. Our results show that the density and the temperature show a sharp decrease and an increase outward across the edge, respectively. In addition, the pressure could be continuous across the edge. These suggest that the edge could be a cold front. If the existence of a cold front is true, this could be evidence that the galaxy cluster RXC J1053.7+5453 experienced

merger with another cluster (or group). It seems that this cluster is in an east-west merger event, considering the overall morphology of X-ray emission of the Chandra image, the location of a possible cold front, and the orientation and location of the radio relic. Alternatively, the thermal pressure ratio at the edge could really be more than unity. It cannot be ruled out that the thermal pressure is discontinuous at the edge. In this case, if the pressure across the edge is in equilibrium, other forms of pressure sources such as cosmic-rays are necessary.

3.3.4 Magnetic field strength in the radio relic

We constrain the magnetic field strength in the radio relic. Blumenthal and Gould (1970) [19] derived the following equations for the synchrotron and inverse Compton emissions from an electron population with a power-law energy spectrum at frequency $\nu_{\rm synch}$ and $\nu_{\rm IC}$, respectively:

$$\frac{dW_{\rm Synch}}{d\nu_{\rm Synch}dt} = \frac{4\pi N_0 e^3 B^{(p+1)/2}}{m_e c^2}\left(\frac{3e}{4\pi m_e c}\right)^{(p-1)/2} a(p)\nu_{\rm Synch}^{-(p-1)/2}, \tag{3.11}$$

$$\frac{dW_{\rm IC}}{d\nu_{\rm IC}dt} = \frac{8\pi^2 r_0^2}{c^2} h^{-(p+3)/2} N_0 (kT_{\rm CMB})^{(p+5)/2} F(p)\nu_{\rm IC}^{-(p-1)/2} \tag{3.12}$$

where N_0 is the normalization, p is the power-law index of the electron spectrum ($N(\gamma) = N_0\gamma^{-p}$;γ is the Lorentz factor of the electron), r_0 is the classical electron radius, h is the Planck constant, and $T_{\rm CMB}$ is CMB temperature ($T_{\rm CMB} = 2.73(1+z)$). The function $a(p)$ and $F(p)$ are given as follows [19]:

$$a(p) = \frac{2^{(p-1)/2}\sqrt{3}\Gamma\left(\frac{3p-1}{12}\right)\Gamma\left(\frac{3p+19}{12}\right)\Gamma\left(\frac{p+5}{4}\right)}{8\pi^{1/2}(p+1)\Gamma\left(\frac{p+7}{4}\right)}, \tag{3.13}$$

$$F(p) = \frac{2^{p+3}(p^2+4p+11)\Gamma\left(\frac{p+5}{2}\right)\zeta\left(\frac{p+5}{2}\right)}{(p+3)^2(p+5)(p+1)}. \tag{3.14}$$

We can estimated the magnetic field strength in the radio relic from the comparison of the observed flux density of the synchrotron and inverse Compton emissions by the relation [34, 71, 72, 9] as follows:

$$\frac{S_{\rm Synch}}{S_{\rm IC}} = \frac{\left(\frac{dW_{\rm Synch}}{d\nu_{\rm Synch}dt}\right)}{\left(\frac{dW_{\rm IC}}{d\nu_{\rm IC}dt}\right)}. \tag{3.15}$$

First, in the case of $\Gamma = 2.0$, we derive the upper limit of the inverse Compton flux density as $S_{\rm IC} < 2.22 \times 10^{-10}$ Jy at 10 keV ($\nu_{\rm IC} = 2.4 \times 10^{18}$ Hz) from the spectral analysis for the non-thermal power-law component ($\Gamma = 2.0$ in subsection 3.2.4). Comparing this value and the radio flux density of the relic as $S_{\rm synch} = 15$ mJy at 1382 MHz [105], the derived magnetic field strength is $B > 0.73$ μG, and similar to those of other relics ($B > 0.1 - 1$ μG).

Secondly, in the case of $\Gamma = 3.8$, we obtain $B > 2.00$ μG using $S_{\rm IC} < 1.11 \times 10^{-8}$ Jy, which is estimated in the same was as in the case of $\Gamma = 2.0$. This lower limit of magnetic field strength is rather high. In addition, if this is true, the energy density of the magnetic field could be higher than the thermal one. We will discuss this problem in the next subsection.

3.3.5 Energy densities in the radio relic region

We estimate energy density of each component in the same way as in subsection 2.3.4. For simplicity, the radio relic region is assumed to be a cylinder whose radius and height are 284 kpc and 243 kpc, respectively. The estimated electron number density becomes $n_e = 3.12^{+0.78}_{-1.08} \times 10^{-5}$ cm^{-3} from the normalization of $apec_{\rm ICM}$ model (table 3.6). Using equation (2.20), the energy density of the thermal ICM is $U_{\rm th} = 1.52^{+1.10}_{-0.45} \times 10^{-13}$ erg cm^{-3} with the obtained n_e, the temperature of this region ($kT = 1.22^{+0.80}_{-0.33}$ keV) and $\mu = 0.6$.

Next, we estimate the energy densities of the magnetic field and the non-thermal electrons for each photon index ($\Gamma = 2.0, 3.8$). In the case of $\Gamma = 2.0$, the energy density of the magnetic field is $U_{\rm mag} > 2.1 \times 10^{-14}$ erg cm^{-3}. As a result, $U_{\rm mag}/U_{\rm th} > 0.14$, which means that the magnetic energy could be more than ten percent of the thermal one. The energy density of the non-thermal electrons corresponding to the 0.3-10 keV X-ray bands is $U_e < 7.8 \times 10^{-16}$erg cm^{-3}. Therefore, $U_{\rm e}/U_{\rm th} < 5.1 \times 10^{-3}$, although the contribution from lower energy electrons is not include in these calculation, which could be dominant in the energy density of the non-thermal electron populations.

On the other hand, in the case of $\Gamma = 3.8$, we obtain $U_{\rm mag} > 1.6 \times 10^{-13}$ erg cm^{-3} and $U_e < 5.6 \times 10^{-12}$erg cm^{-3}. As a result, $U_{\rm mag}/U_{\rm th} > 1.00$ and $U_{\rm e}/U_{\rm th} < 36.7$. This means that the magnetic field energy density might be higher than the thermal one. This seems to be quite odd, and makes us

suspicious of the underlying assumptions. For example, DSA dose not hold and hence $\Gamma \neq 3.8$, or the electron spectrum is significantly deviated from a single power-law form. Another possibility is that the Mach number derived from our results is seriously underestimated owing to projection effects and/or limited spatial resolution. In this case, the actual electron spectrum should be flatter.

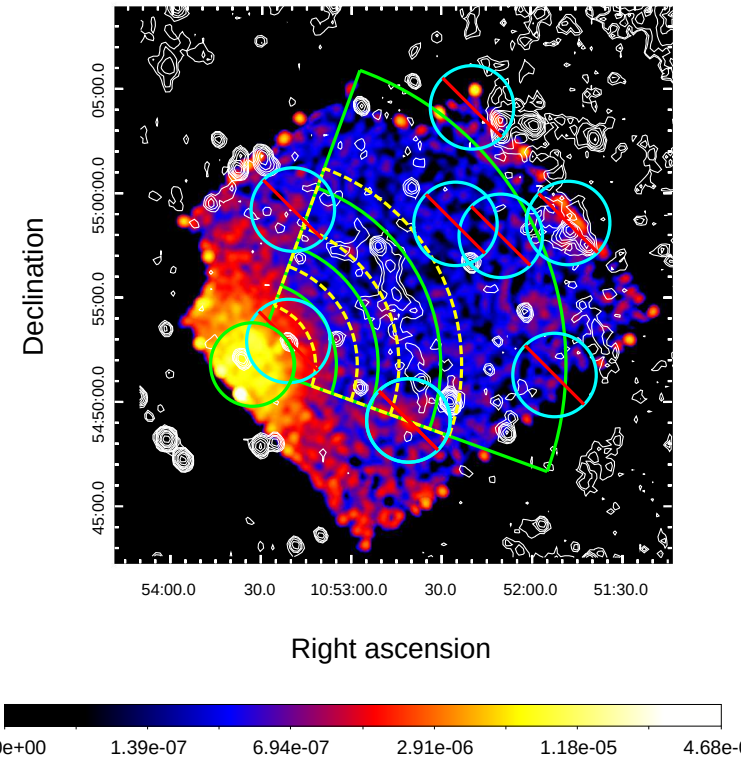

Figure 3.2: Suzaku image with radio contours of RXC J1053.7+5453
An XIS1 image in the 0.5-8.0 keV band (Obs.ID:809120010) with the 1382 MHz radio contours [105]. The X-ray image was corrected for exposure and vignetting effects after subtracting NXB and smoothed by a Gaussian kernel with $\sigma = 0.'26$. The radio contours are drawn at $[1, 2, 4, 8, ...] \times 0.1$ mJy beam^{-1}. The green and yellow regions were used for the spectral analysis, with annular radius of $2', 4', 6', 9', 15'$ and $3', 5', 7', 10'$, respectively. The light blue circles are excluded regions of a point source.

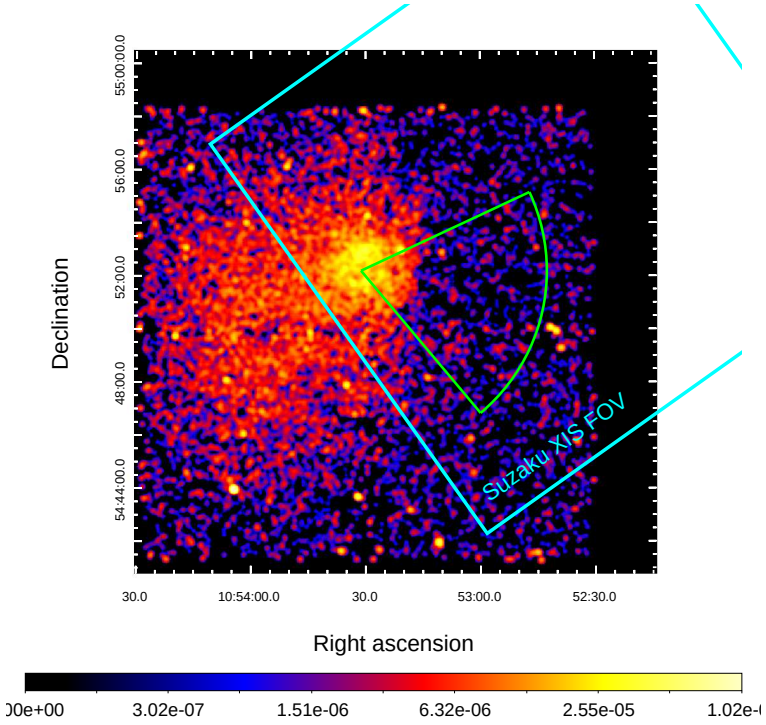

Figure 3.3: Chandra image with radio contours of RXC J1053.7+5453 A Chandra image in 0.5-2.0 keV band (Obs.ID:15322). The image was corrected for exposure. The green sector is a region used for extracting surface brightness profile in subsection 3.2.3. Light blue box is the Suzaku XIS FOV.

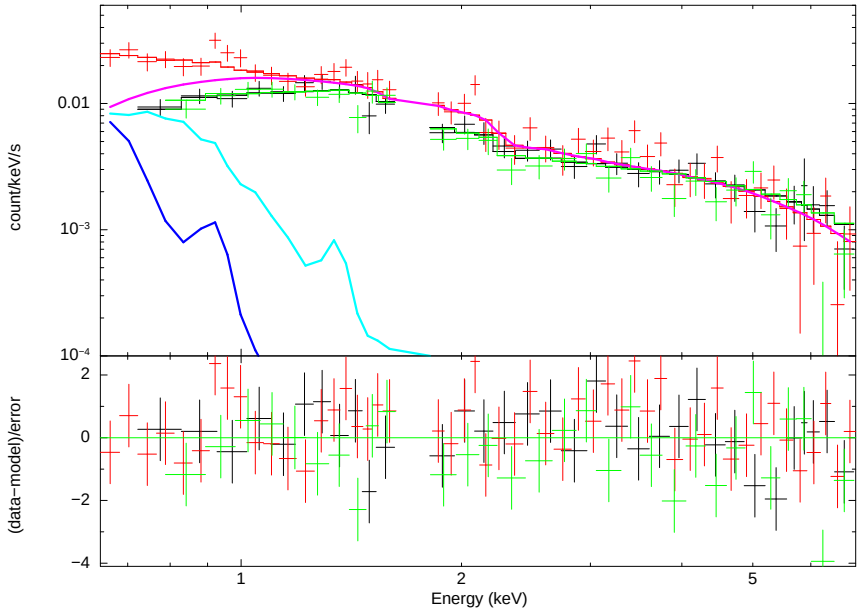

Figure 3.4: XIS spectra of the background field for RXC J1053.7+5453. The XIS spectra of the background field fitted with the background model described in the text. Each color of crosses and solid histograms same as in figure 2.3.

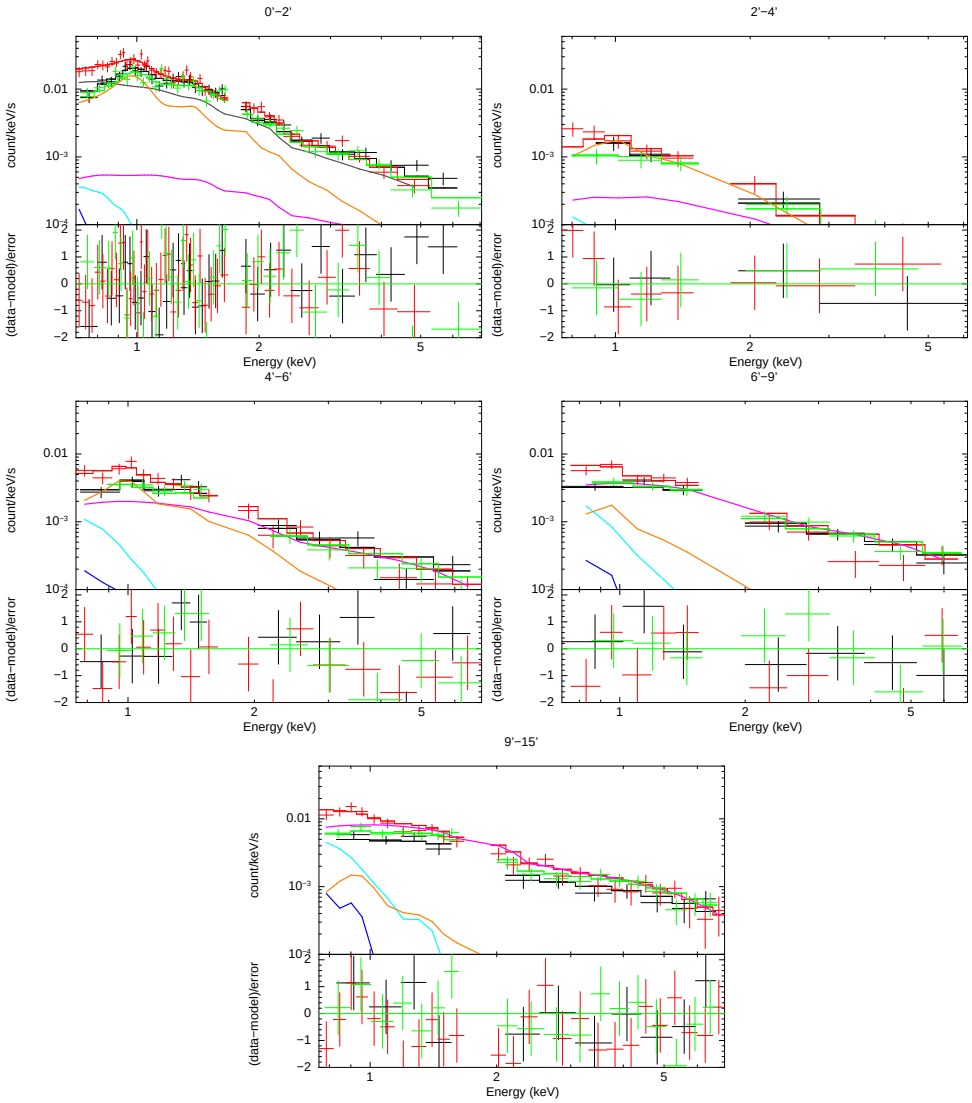

Figure 3.5: XIS spectra of regions across the relic of the galaxy cluster RXC J1053.7+5453.

The XIS spectra of regions across the relic fitted with the model described in the text. Each color of crosses and solid histograms same as in figure 2.6. The Gray solid line in the $0' - 2'$ region spectra is an AGN component.

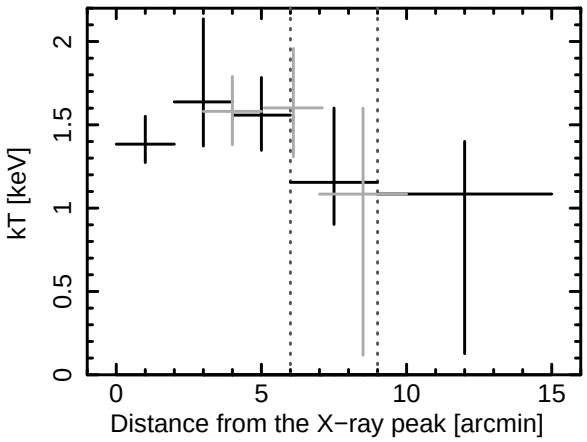

Figure 3.6: Temperature profile across the radio relic of the galaxy cluster RXC J1053.7+5453.
The temperature profile across the radio relic. The horizontal axis represents the angular distance from the X-ray peak. Black and light gray crosses show the results from green and yellow regions of figure 3.2. Only statistical errors are displayed. The positions of the inner and outer edges of the relic are displayed by dark gray dotted lines.

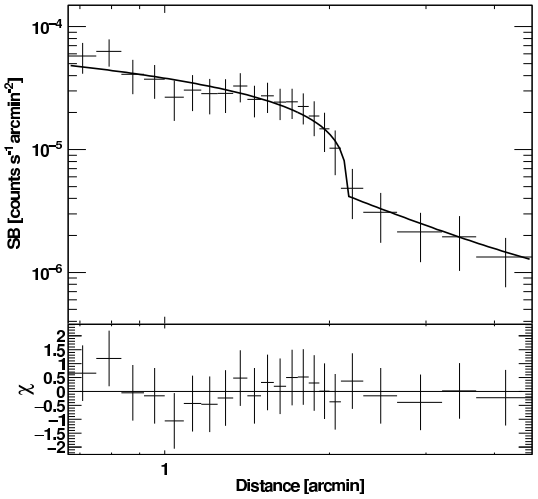

Figure 3.7: Surface brightness profile across the edge.
The surface brightness profile across the surface brightness edge. The profile was binned so that a signal-to-noise ratio is more than 2 per bin. The best fit model described in the text is displayed with the black line.

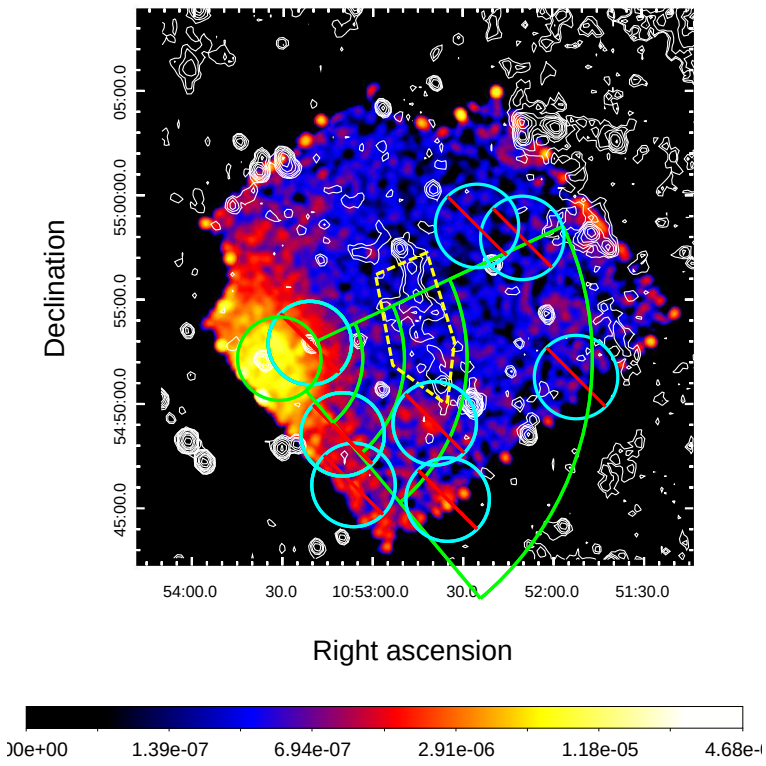

Figure 3.8: Surface brightness edge regions
The XIS image and radio contours same as in the figure 3.2, but overlaid with green regions utilized in the surface brightness edge analysis. The radius of annulus region are $2'$, $4'$, $6'$, $9'$, and $15'$. Yellow region was used to search for inverse Compton component, whose size is $4.50 \times 10^{-3}\mathrm{deg}^2$. The light blue circles are excluded regions of a point source.

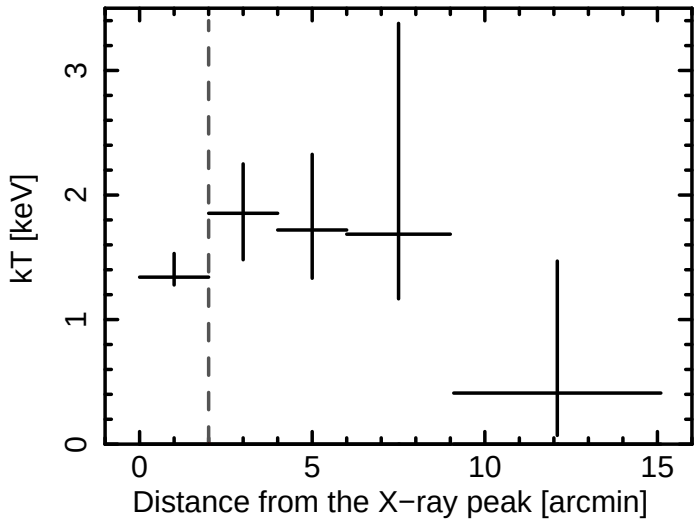

Figure 3.9: Temperature profile across the surface brightness edge. The temperature profile across the surface brightness edge. The position of the surface brightness edge is displayed by dark gray dotted line.

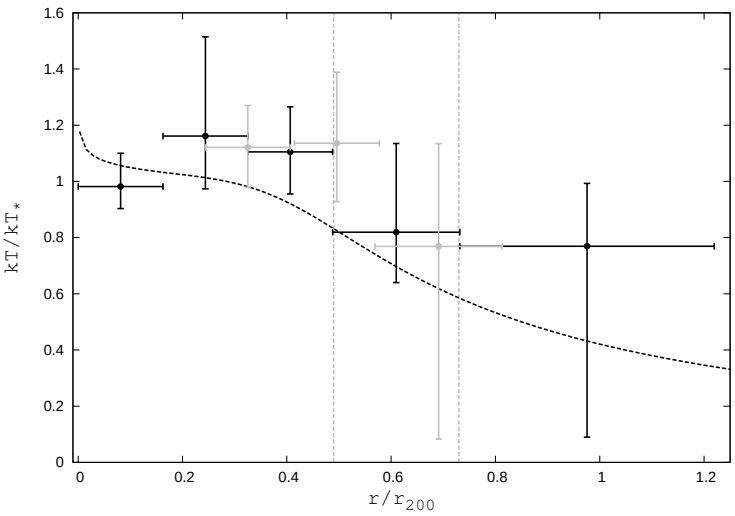

Figure 3.10: Comparison of temperature profile along the collision axis with the scaled profile of Okabe et al. (2014) in RXJ1053.
Comparison of the scaled temperature profile along the collision axis toward the north with a universal temperature profile obtained from Suzaku X-ray and Subaru weak-lensing observations [67]. Crosses and dotted black line represent our results and the universal profile, respectively. The positions of the inner and outer edges of the relic are displayed by dark gray dotted lines. Considering the errors, the obtained temperatures are consistent with the universal profile.

Chapter 4

Discussion on Particle Acceleration Processes in the Radio Relics

Particle acceleration processes in the radio relic are researched with both the X-ray (XMM-Newton, Suzaku, and Chandra) [5, 6, 63, 9] and radio observations [105, 106, 49, 91, 107]. Table 4.1 shows the derived Mach number of shocks by the X-ray (Suzaku) and radio observations in the literature and this work. Figure 4.1 shows Mach numbers derived from the radio spectral index ($M_{\rm radio}$) plotted against those from the X-ray temperature measurements ($M_{X,kT}$), which is an updated version of figure 8 in Akamatsu and Kawahara (2013) [6]. From table 4.1, some relics have consistent Mach numbers considering the errors. On the other hand, in other relics (CIZA2242 North, A2255, and A3667 South), M_X is lower than $M_{\rm radio}$. The Toothbrush relic also shows clear discrepancy even considering both the statistical and systematic errors. If these are true, a simple DSA theory does not hold in these cluster. We propose followings as the possibility of these discrepancies; a) The estimated Mach number from X-ray observation is underestimated by projection effects [90, 43]. b) The temperature in the post-shock region is underestimated because electrons are not in reaching thermal equilibrium [117, 110]. c) There are low energy relativistic electrons and (or) reaccelerated electrons, resulting

in a flat radio spectrum with a rather small temperature jump [57, 74, 50, 92]. d) Other mechanisms, for example, turbulence accelerations [36].

Note that the derived Mach number from X-ray observations ($M_{X,kT}$) could be underestimated because the temperature in pre-shock region is overestimated owing to projection effects and/or moderate resolution of Suzaku point spread function (PSF). If the shock front is not parallel to the line of sight, the obtained temperature in pre-shock region could be overestimated because the ICM in the pre- and post-shock regions overlap with each other. As a result, the derived $M_{X,kT}$ could be underestimated. Additionaly, considering the Suzaku PSF, the temperature in pre-shock region could be overestimated. In particularly, because of the contamination from the hotter and brighter post-shock region, the temperature of the cooler and fainter pre-shock region would be overestimated. Therefore, we will underestimate $M_{X,kT}$. If $M_{X,kT}$ is underestimated, for some radio relics with $M_X < M_{\rm radio}$, the $M_{X,kT}$ could be consistent with the $M_{\rm radio}$, and a simple DSA theory does hold.

As mentioned previously, the present shock Mach number alone cannot determine the Toothbrush relic spectrum. The spectrum has a memory of the past acceleration history in a reacceleration scenario, where the electrons in the relic have already accelerated once somewhere. Fujita et al. (2015) reported that the turbulent reacceleration of cosmic ray electrons which had been weakly accelerated at a shock [36]. As a result, they reproduced the hard spectrum of the relic observed in the Toothbrush cluster, which cannot be explained by the simple DSA model. This results show that the turbulent reacceleration may be the main mechanism to produce high-energy electrons in the Toothbrush relic.

In some clusters, on the other hand, recent low frequency radio observations with LOFAR give lower $M_{\rm radio}$ than the previous values. For example, in the galaxy cluster CIZA J2242.8+5301, van Weeren et al. (2010) [104] reported the Mach number of 4.58 ± 1.32 at the north relic outer edge. However, Hoang et al. (2017) [44] reported $2.7^{+0.6}_{-0.3}$ at lower frequency bands. This value is consistent with the X-ray result ($2.7^{+0.7}_{-0.4}$ [8]). Similarly, in the Toothbrush cluster, van Weeren et al. (2016) [107] reported the Mach number of $2.8^{+0.5}_{-0.3}$ with LOFAR. Although this value is lower than the former result of van Weeren et al. (2012) [106], still higher than our result ($1.55^{+0.29}_{-0.25}$). If

we observe in a lower frequency band, the estimated Mach number at the Toothbrush relic outer edge could be consistent with the X-ray results.

Additionally, some theoretical studies suggest that there are difficulties in particle acceleration at low Mach number shocks. For example, Vink and Yamazaki (2014) reported that shocks with Mack number less than $\sqrt{5}$ cannot accelerate particles [109]. Although the existence of radio relics is evidence of the accelerated particles, there are radio relics whose Mach number is lower than $\sqrt{5}$. In these relics, other particle acceleration process could be necessary to explain the accelerated particles.

Table 4.1: Mach numbers of the relic outer edge

	$M_{\rm X}$	$M_{\rm radio}$
CIZA J2242.8+5301 North	$2.7^{+0.7}_{-0.4}$ [8]	4.58 ± 1.32 [104]
CIZA J2242.8+5301 South	$1.7^{+0.4}_{-0.3}$ [8]	2.8 ± 0.2 [91]
Abell 3376	2.94 ± 0.60 [6]	2.23 ± 0.20 [49]
Abell 3667 North	2.41 ± 0.39 [6]	2.4 ± 0.4 [42]
Abell 3667 South	1.75 ± 0.13 [6]	2.4 ± 0.4 [42]
Coma	2.2 ± 0.5 [7]	1.9 ± 0.05 [102]
Abell 2255	$1.42^{+0.19}_{-0.15}$ [9]	2.77 ± 0.35 [75]
Abell 2256	$1.7^{+0.1}_{-0.1}$ [103]	2.5 ± 0.2 [103]
1RXS J0603.3+4214 (Toothbrush)	$M_X = 1.50^{+0.28}_{-0.24}$ (This work)	$3.0 \sim 4.6$ [106]
RXC J10537+5453	$1.44^{+0.30}_{-0.98}$ (This work)	-

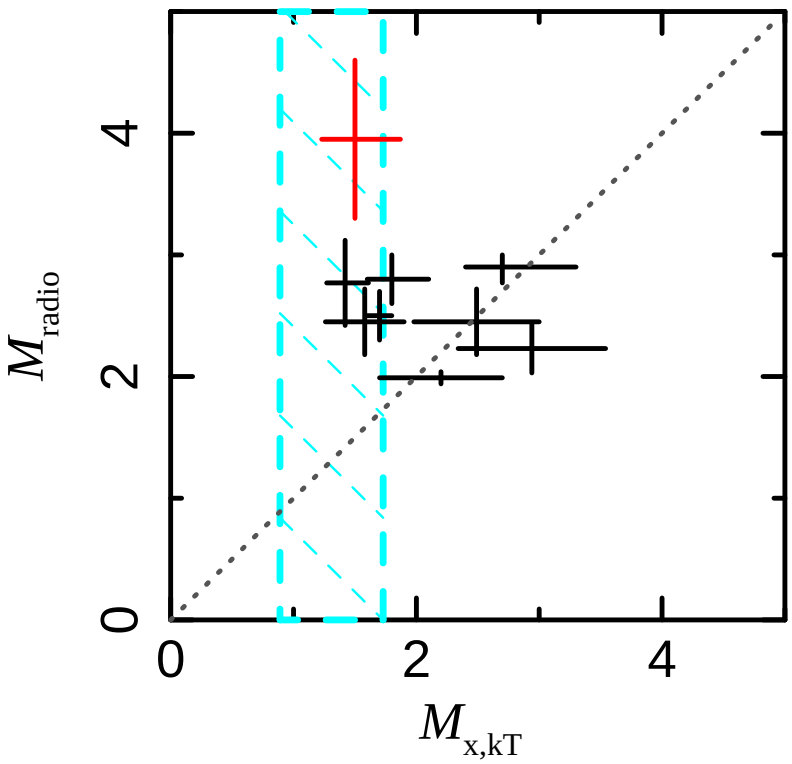

Figure 4.1: $M_{X,kT}$ - M_{radio} plots of radio relics
Mach numbers derived from the radio spectral index (M_{radio}) plotted against those from the X-ray temperature measurements ($M_{X,kT}$), which is an updated version of figure 8 in Akamatsu and Kawahara (2013) [6]. The gray dotted lines represent $M_{X,kT} = M_{\mathrm{radio}}$. Black crosses show all relic except for this work in table 4.1. A red cross shows the "Toothbrush" relic. A light blue hatched area shows the error range of $M_{X,kT}$ in the RXC J1053.7+5453.

Appendix A

Characteristics of the X-ray Satellites

A.1 Suzaku

Suzaku is the fifth X-ray astronomy satellite in Japan, which is devoted to observations of celestial X-ray sources. It was launched on 10 July 2005 and the mission came to an end on 2 September 2015. Suzaku was placed in a near-circular orbit with an apogee of 568 km and an orbital period of about 96 minutes. Because it is in a low altitude orbit, the background level is lower than other X-ray satellites (e.g. Chandra and XMM-Newton).

Suzaku has five X-ray telescopes (XRTs), four X-ray imaging spectrometers (XISs), a hard X-ray detector (HXD), and a X-ray spectrometer (XRS). The XIS is X-ray CCD camera, and it has the energy resolution of 130 eV with the energy range $0.2 - 12$ keV. There are four X-ray sensitive imaging CCD cameras, three of which are front-illuminated (FI; energy range of 0.4-12 keV) and one back-illuminated (BI; 0.2-12 keV), with moderate energy resolution. Unfortunately, the entire imaging area of the XIS2 was lost in 2005 November and a part of the XIS0 was also damaged in 2009 June. The XRS is a X-ray microcalorimeter. It has the energy resolution of 6 eV. However, the XRS lost all of its cryogen before routine scientific observations could begin on 2005 August. The HXD was developed to cover the high energy range (10-600 keV). All of the instruments on Suzaku can operate simultaneously,

and high sensitivity X-ray spectroscopy in the wide energy bands is possible. Each of co-aligned XRTs features an X-ray mirror with an angular resolution of $\sim 2'$ (Half-power diameter; HPD). In this section, we shortly describe only the XRT and XIS that we used in the spectral analysis. For more detailed information, please see "The Suzaku Technical Description" [96].

A.1.1 X-ray Telescopes: XRT

Suzaku has five X-ray telescopes (XRTs [86]). Four XRTs on board Suzaku are used for the XIS (XRT-I), and the remaining XRT is for the XRS (XRT-S). The telescope dimensions and parameters of XRT-I are listed in table A.1. The focal length is 4.75 m and the optical axes of the quadrants of each XRT are aligned to within $2'$ from the mechanical axis. The effective areas at 1.5 keV and 8 keV are 440 cm^2 and 250 cm^2, respectively. The angular resolution of the XRTs ranges $1'.8 - 2'.3$, expressed in terms of half-power diameter, within which half of the focused X-rays are enclosed. The angular resolution dose not significantly depend on the energy of the incident X-rays in the energy range of XIS ($0.2 - 12$ keV).

Figure A.1: Suzaku X-ray telescope [96].

Table A.1: Telescope dimensions and parameters of XRT-I [96].

	Suzaku XRT-I
Focal length	4.75 m
Outer diameter	399 mm
Mass per telescope	19.5 kg
Reflecting surface	Au
Reflectors per telescope	1400
Angular resolution (HPD)	$\sim 2'.0$

A.1.2 X-ray Imaging Spectrometers: XIS

Suzaku has four X-ray imaging spectrometers (XISs, [51]), which are named XIS0, 1, 2, and 3. The XIS is composed of four units of Si-based X-ray charge coupled device (CCD) cameras (figure A.2). In these X-ray sensors, incident X-ray photons are transformed into a number of electron-hole pairs through photoelectric absorptions and subsequent ionization by photoelectrons and their secondaries. The energy of the incident photon can be measured since it is proportional to the amount of charge produced. Each XIS unit is located at the focal plane of one of fore independent, identical, and coaligned X-ray telescope modules. The XIS is operated in photon counting mode, in which each X-ray event is discriminated from the others and its position, energy, and arrival time are reconstructed. This gives the XIS imaging spectroscopic capabilities in the 0.2-12 keV energy band. The overview of Suzaku XIS is shown in table A.2. The four XISs are true imagers, with a large field of view ($\sim 18' \times 18'$), and moderate spectral resolution.

The XIS1 is a back side illuminated (BI) CCD, and the others (XIS0, 2, and 3) are front side illuminated (FI) CCD. The BI CCD has high sensitivity in low energy band than FI CCD. Each CCD camera has a single CCD chip with an array of 1024×1024 pixels and covers an $17'.8 \times 17'.8$ region on the sky. A single XIS CCD chip consists of four segments called segment A, B, C, and D. Each segment has its own readout node. A part of the segment A of the XIS0 was flooded with a large amount of charge. It is possibly owing to a

Figure A.2: Suzaku X-ray imaging spectrometers [96].

micro-meteorite impact [1)]. Each XIS carries ^{55}Fe calibration sources near the two corners of the chip. The ^{55}Fe sources emit strong Mn Kα and Kβ lines at 5.9 keV and 6.5 keV, respectively. Two sources illuminate corners of the segment A and D of the imaging area at the far side of the readout node.

The energy resolution is defined as the full width at half maximum (FWHM) of the Gaussian function of the main peak. The energy resolution of an XIS CCD is as follows:

$$\Delta E(\mathrm{eV}) = W \times \sqrt{8 \ln 2} \times \sqrt{N^2 + \frac{EF}{W} + AE^2}, \tag{A.1}$$

where E is the X-ray energy, W is the mean energy for electron-hole pair creation (Si; 3.65 eV), N is the RMS system noise, F is Fano factor, and A is a correction term. Though the physical interpretation of A is not clear, this phenomenological model can fit the XIS data well. A energy resolution of $\sim$ 130 eV at 5.9 keV was achieved for all the sensors and segment by the XIS team [51].

[1)] http://www.astro.isas.ac.jp/suzaku/doc/suzakumemo/suzakumemo-2010-01.pdf

Table A.2: Overview of Suzaku XIS[96].

	Suzaku XIS
Field of view	$17'.8 \times 17'.8$
Bandpass	0.2 - 12.0 keV
Pixel grid	1024 ×1024
Pixel size	24 μm
Energy resolution	∼130 eV @6 keV
Effective area (incl XRT-I))	340 cm^2(FI), 390 cm^2(BI) @1.5 keV
	350 cm^2(FI), 100 cm^2(BI)@8 keV
Time resolution	8 s (Normal mode), 7.8 ms(P-Sum mode)

A.2 Chandra

The Chandra X-ray observatory was successfully launched by NASA's Space Shuttle Columbia on 1999 July 23. Chandra was designed to provide order of magnitude advances over previous X-ray astronomy mission with regards to spatial and spectral resolution. The orbit is highly elliptical and varies with time. The apogee and perigee height was $\sim 131,000$ km and $\sim 18,500$ km, respectively, as of 2016 December.

Chandra has the High Resolution Mirror Assembly (HRMA), the Advanced CCD Imaging Spectrometer (ACIS) and the High Resolution Camera (HRC). The HRMA consists of four pairs of nested reflecting surfaces, arranged in the usual Wolter-I geometry, with a diameter of 1.2 m. The focal length is 10 m. The HRMA produces images with a half-power diameter of the point spread function (PSF) of $< 0''.5$. The ACIS contains 10 planar, 1024×1024 pixel CCDs, four of which arranged in a 2×2 array (ACIS-I) are used for imaging, and six of which arranged in a 1×6 array (ACIS-S) aer used either for imaging or for a grating spectrum read out. Two CCDs are back illuminated (BI) and eight are front illuminated (FI). The response of the BI devices extends to energies below that accessible to the FI chips. The chip average energy resolution of the BI devices is better than that of the FI devices. The HRC is a microchannel plate (MCP) instrument comprised of two detectors, one optimized for imaging (HRC-I), and one (HRC-S)

which serves as read-out for the Low Energy Transmission Grating (LETG). The HRC-I provides the largest field of view ($\sim 30' \times 30'$) of any detector aboard Chandra, and its response extends to energies below the sensitivity of ACIS, albeit without comparable spectral resolution. The time resolution of the HRC detector is 16μs.

In this section, we shortly describe only the HRMA and ACIS that we used in this work. For more detailed information, please see "The Chandra proposers Observatory Guide" [25]

A.2.1 High Resolution Mirror Assembly: HRMA

The Chandra X-ray telescope consists of 4 pairs of concentric thin walled, grazing incidence Wolter-I mirrors called the High Resolution Mirror Assembly (HRMA) [2]. The front mirror of each pair is a paraboloid and the back a hyperboloid. The eight mirrors were fabricated from Zerodur glass, polished, and coated with iridium on a binding layer of chromium. Figure A.3 shows the four nested HRMA mirror pairs and associated structures. The outer mirror pair is number 1 and progressing inwards 3, 4, and 6. The pair diameters range from 0.65 to 1.23 meters. An annular on-axis beam enters each mirror pair is reflected from paraboloids and hyperboloids and exits to converge to a focus. Table A.3 shows more information of the HRMA.

The point spread function (PSF) of HRMA has been simulated with numerical raytrace calculations based upon the mirror model previously discussed. A most useful parameter is the encircled energy fraction as a function of radius from the image center. The PSF and the encircled energy fraction for a given radius depend upon the off axis angle and energy. The optical axis of HRMA is defined for practical purposes, and calibrated in flight, as the direction of the sharpest PSF. The PSF broadens, and the encircled energy fraction decreases as (a) the off axis angle increases because of mirror aberrations, and (b) the X-ray energy increases because of increased X-ray scattering.

Table A.3: Chandra HRMA characteristics [25].

	Chandra HRMA
Focal length	10.070 ± 0.003 m
Mirror outer diameter	1.23 m
Mass per telescope	1484 kg
Total length	276 cm
Angular resolution (PSF)	$< 0''.5$
Effective area	800cm^2 @ 0.25 keV
	400cm^2 @ 5.0 keV
	100cm^2 @ 8.0 keV

A.2.2 Advanced CCD Imaging Spectrometer: ACIS

The Advanced CCD Imaging Spectrometer (ACIS) offers the capability to simultaneously acquire high resolution images and moderate resolution spectra. The instrument can also be used in conjunction with High Energy Transmission Grating (HETG) or Low Energy Transmission Grating (LETG) to obtain higher resolution spectra. The ACIS contains 10 planar, 1024×1024 pixel CCDs (figure A.4), four of which arranged in a 2×2 array (ACIS-I) are used for imaging, and six of which arranged in a 1×6 array (ACIS-S) are used either for imaging or for a grating spectrum read out. Two CCDs are back illuminated (BI) and eight are front illuminated (FI). The response of the BI devices extends to energies below that accessible to the FI chips. The chip average energy resolution of the BI devices is better than that of the FI devices.

A CCD is a sold state electronic device composed primarily of silicon. A "gate" structure on one surface defines the pixel boundaries by alternating voltages on three electrodes spanning a pixel. The silicon in the depletion region (the region below the gates wherein most of the absorption takes place) has an applied electric field so that charge move quickly to the gate surface. The gate allows confined charge to be passed down a "bucket brigade" of pixels in parallel to a serial read out at one edge by appropriately varying the voltages in the gates. The front illuminated CCDs of ACIS have the gate

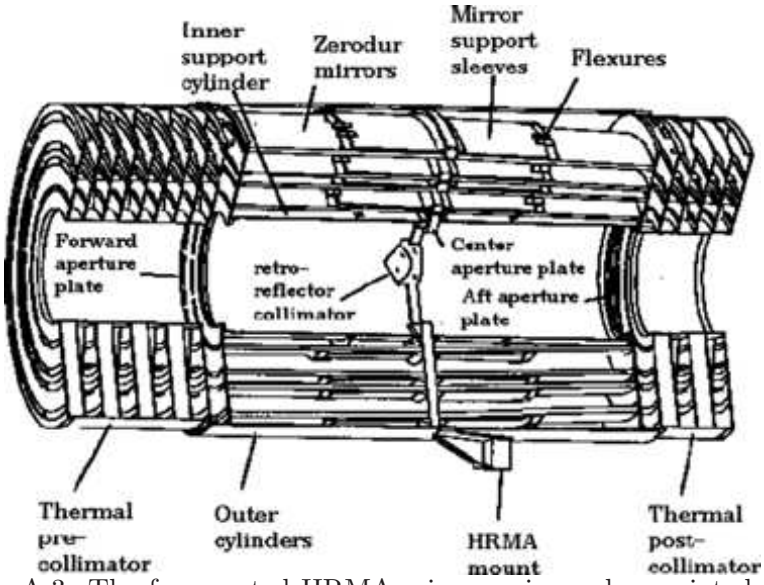

Figure A.3: The four nested HRMA mirror pairs and associated structures [25].

structure facing the incident X-ray beam. Two of the CCD chips on the ACIS-S array (S1 and S3 in figure A.4) are back illuminated (BI) chips. These have had the back sides of the chip treated, removing insensitive, underplayed bulk silicon material and leaving the photo-sensitive depletion region exposed.

Photoelectric absorptions of an X-ray photon in silicon results in the liberation of a proportional number of electrons. An average of one electron-hole pair for each 3.7 eV of energy absorbed. Immediately after the photoelectric interaction, the charge is confined by electric fields to a small volume near the interaction site. Charge in a FI device can also be liberated below the depletion region, in an inactive substrate, where it diffuses into the depletion region. This charge may easily appear in two or more pixels. Good spectral resolution depends upon an accurate determination of the total charge deposited by a single photon. This in turn depends upon the fraction of charge collect, the fraction of charge lost in transfer from pixel during read out, and the ability of the read out amplifiers to measure the charge. Spectral resolution also depends on read noise and off-chip analog processing electronics. The ACIS CCDs have read out noise less than 2 electrons RMS. Total system

noise for the 40 ACIS signal chains ranges from 2 to 3 electrons (RMS) and is dominated by the off-chip analog processing electronics. Table A.4 show the ACIS characteristics.

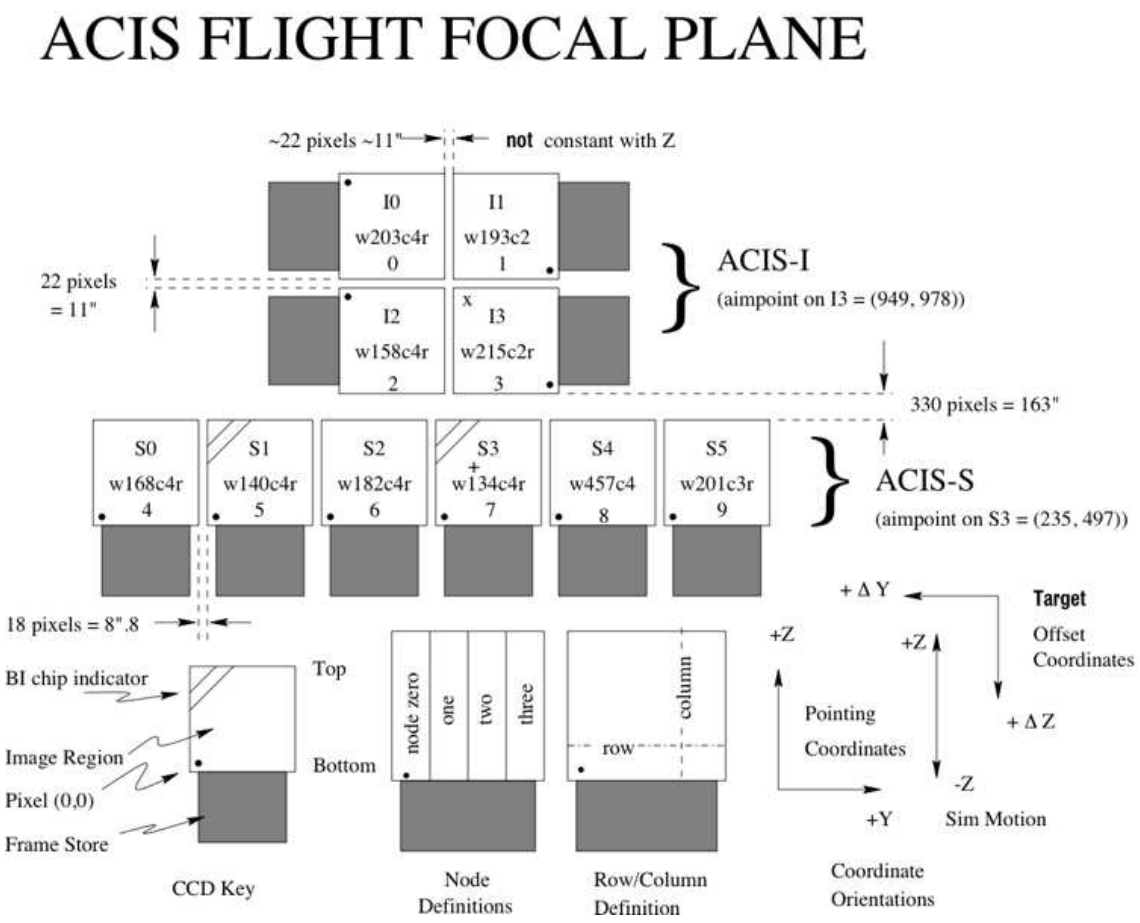

Figure A.4: A schematic drawing of the ACIS focal plane. [25].

Table A.4: Chandra ACIS characteristics [25].

	Chandra ACIS
Array size	$16'.9 \times 16'.9$ (ACIS-I)
	$8'.3 \times 50'.6$ (ACIS-S)
CCD format	1024 $\times$1024
Pixel size	23.985 μm
On-axis effective area [1)]	600 cm^2(FI) @1.5 keV
	40 cm^2(FI)@8 keV
Point source sensitivity	4×10^{-15} erg/cm^{-2}/s (0.4-6.0 keV)

[1)]Effective area is integrated over the PSF to $> 99\%$ encircled energy.

Appendix B

Bugs in the *apec* model of XSPEC

The *apec* model in XSPEC version 12.8.2 had the incorrect normalization and abundance dependence on redshift (z), which gave too small value by a factor $\sim (1+z)$ [1)]. This bug was reported on June 15 2016. When the paper of the galaxy cluster 1RXS J0603.3+4214 [47] was published, this bug had not been found. Therefore, the normalization and abundance of our results in this cluster could be incorrect. We preform spectral analysis again for some regions in this cluster with XSPEC 12.9.0, which is corrected bugs following the processes descriptions in the XSPEC known issues topics [2)].

B.1 Results of the Galaxy Cluster 1RXS J0603.3+4214 After Removing Bugs

B.1.1 Candidate shock

We fit again the spectrum of pre- (R2) and post-shock (R3) regions by the model used in subsection 2.2.2. The resultant best-fit parameters are listed in table B.1. The first, second, and third errors are statistical, CXB systematic, and NXB systematic errors, respectively. We derive the Mach num-

[1)] https://heasarc.gsfc.nasa.gov/docs/xanadu/xspec/issues/archive/issues.12.8.2q.html
[2)] https://heasarc.gsfc.nasa.gov/docs/xanadu/xspec/issues/archive/issues.12.9.0u.html

Table B.1: Fitting results of pre- (R2) and post-shock (R3) regions.

Region	kT (keV)[1)]	abundance[1)3)]	$\chi^2/d.o.f$	$\Delta_{\rm CXB}$ (%)[2)]
$R2$	$5.09^{+1.58+0.90+0.61}_{-1.00-0.85-0.90}$	0.3 (fixed)	71.57/66	66%
$R3$	$7.43^{+0.90+0.28+0.19}_{-0.84-0.30-0.27}$	0.3 (fixed)	195.95/161	48%

[1)] The first, second, and third errors are statistical, CXB systematic, and NXB systematic, respectively.

[2)] CXB fluctuations at the 90 % confidence level estimated with equation (2.3).

[3)] The abundance table of Asplund et al. (2009) [11] is used.

ber from the temperature ratio of pre- (R2) and post-shock (R3) regions using Rankine-Hugoniot relation (equation (2.11)). As a result, we obtained $M_X = 1.46^{+1.06+0.60+0.40}_{-0.68-0.56-0.41}$. This Mach number is consistent with the result in subsection 2.3.2 ($M_X \sim 1.5$), taking account of the statistical errors.

B.1.2 Energy densities

The obtained electron number density in subsection 2.3.4 could be overestimated. We fit again the spectrum of post-shock (R3) region by the model used in subsection 2.2.5. As a result, we obtained $F_{\rm IC} < 1.1 \times 10^{-13}$ erg s^{-1} cm^{-2} in 0.3-10 keV bands, $B > 2.3$ μG, and $n_e = 3.39 \times 10^{-4}$ cm^{-3}. From these results, each energy density becomes $U_{\rm th} = 1.0 \times 10^{-11}$ erg cm^{-3}, $U_{\rm mag} > 2.1 \times 10^{-13}$ erg cm^{-3}, and $U_{\rm e} < 1.7 \times 10^{-14}$ erg cm^{-3}. These are consistent with results in subsection 2.3.4. In conclusion, our results in subsection 2.3.4 were hardly affected by the bugs in XSPEC version 12.8.2.

Acknowledgement

Firstly, I would like to express my sincere gratitude to my supervisor Professor Motokazu Takizawa in Yamagata University. His guidance helped me in all the time of research and writing of this thesis. He has been a tremendous mentor for me. I would like to thank him for encouraging my research. I would also like to thank Professor Shinpei Shibata, Professor Toyoharu Umebayashi, and Professor Humitaka Yanagisawa not only for their insightful comments and encouragement, but also the difficlt questions. I would also like to thank Dr. Hiroki Akamatsu, Dr. Hajime Kawahara, Dr. Reinout J. van Weeren, Dr. Takaya Ohashi, Dr. Yoshitaka Ishisaki, Dr. Yasushi Fukazawa, Dr. Jelle S. Kaastra, Dr. Kazuhiro Nakazawa, Dr. Naomi Ota, Dr. Huub J. A. Röttgering, Dr. Jacco Vink, and Dr. Fabio Zandanel, who gave me constructive comments and warm encouragement. Without their help, this thesis would not been completed.

Last but not least, I would like to thank my family: my parents and my brother for supporting me mentally throughout writing this thesis and my my life in general.

References

[1] Aguerri, J. A., Sánchez-Janssen, R., & Muñoz-Tuñón, C. 2007, A&A, 471,17, "A study of catalogued nearby galaxy clusters in the SDSS-DR4. I. Cluster global properties"

[2] Aschenbach, B. 1985, RPPh, 48, 579, "X-ray telescopes"

[3] Ajello, M., Rebusco, P., Cappelluti, N., Reimer, O., Böhringer, H., Greiner, J., Gehrels, N., Tueller, J., & Moretti, A. 2009, ApJ, 690, 367, "Galaxy Clusters in the Swift/Burst Alert Telescope Era: Hard X-rays in the Intracluster Medium"

[4] Akahori, T., & Yoshikawa, K. 2010, PASJ, 62, 335, "Hydrodynamic Simulations of Merging Galaxy Clusters: Non-Equilibrium Ionization State and Two-Temperature Structure"

[5] Akamatsu, H., de Plaa, J., Kaastra, J., Ishisaki, Y., Ohashi, T., Kawaharada, M., & Nakazawa, K. 2012, PASJ, 64, 49, "Properties of the Intracluster Medium of Abell 3667 Observed with Suzaku XIS"

[6] Akamatsu, H., & Kawahara, H. 2013, PASJ, 65, 16, "Systematic X-Ray Analysis of Radio Relic Clusters with Suzaku"

[7] Akamatsu, H., Inoue, S., Sato, T., Matsusita, K., Ishisaki, Y., & Sarazin, C. L. 2013, PASJ, 65, 89, "Suzaku X-Ray Observations of the Accreting NGC 4839 Group of Galaxies and a Radio Relic in the Coma Cluster"

[8] Akamatsu, H. van Weeren, R. J., Ogrean, G. A., Kawahara, H., Stroe, A., Sobral, D., Hoeft, M., Rttgering, H., Brggen, M., Kaastra, J. S.,

2015, A&A, 582, 87, “Suzaku X-ray study of the double radio relic galaxy cluster CIZA J2242.8+5301”

[9] Akamatsu, H., Mizuno, M., Ota, N., Zhang, Y.-Y., van Weeren, R. J., Kawahara, H., Fukazawa, Y., Kaastra, J. S., Kawaharada, M., Nakazawa, K., Ohashi, T., Röttgering, H. J. A., Takizawa, M., Vink, J., & Zandanel, F., 2017, A&A, 600, 100, “Suzaku observations of the merging galaxy cluster Abell 2255: The northeast radio relic”

[10] Anders, E., & Grevesse, N. 1989, Geochim. Cosmochim. Acta, 53, 197, “Abundances of the elements - Meteoritic and solar”

[11] Asplund, M., Grevesse N., Sauval A.J. & Scott P. 2009, ARA&A, 47, 481, “The Chemical Composition of the Sun”

[12] Bartels, R., Zandanel, F., & Ando, S. 2015, A&A, 582, 20, “Inverse-Compton emission from clusters of galaxies: Predictions for ASTRO-H”

[13] Bonafede, A., Giovannini, G., Feretti, L., Govoni, F., & Murgia, M. 2009, A&A, 494, 429, “Double relics in Abell 2345 and Abell 1240. Spectral index and polarization analysis”

[14] Bamba, A., Fukazawa, Y., Hiraga, J., S., Hughes, J., P., Katagiri, H., Kokubun, M., Koyama, K., Miyata, E., Mizuno, T., Mori, K., Nakajima, H., Ozaki, M., Petre, R., Takahashi, H., Takahashi, T., Tanaka, T., Terada, Y., Uchiyama, Y., Watanabe, S., Yamaguchi, H. 2008, PASJ, 60, 153, “Suzaku Wide-Band Observations of SN1006”

[15] Bartels, R., Zandanel, F., & Ando, S. 2015, A&A, 582, 20, “Inverse-Compton emission from clusters of galaxies: Predictions for ASTRO-H”

[16] Bell. A. R.,1978, MNRAS, 182, 147, “The acceleration of cosmic rays in shock fronts - I”

[17] Bell. A. R.,1978, MNRAS, 182, 443, “The acceleration of cosmic rays in shock fronts - II”

[18] Blandford, R. & Eichler, D. 1987 Phys. Rep., 154, 1, “Particle acceleration at astrophysical shocks: A theory of cosmic ray origin”

[19] Blumenthal, G. R., & Gould, R. J. 1970, Rev. Mod. Phys, 42, 237, "Bremsstrahlung, Synchrotron Radiation, and Compton Scattering of High-Energy Electrons Traversing Dilute Gases"

[20] Brunetti, G., Setti, G., Feretti, L., & Giovannini, G. 2001, MNRAS, 320, 365

[21] Brunetti, G., & Jones, T., W. 2014, International Journal of Modern Physics D, 23, 1430007, "Cosmic Rays in Galaxy Clusters and Their Nonthermal Emission"

[22] Brüggen, M., van Weeren, R. J., & Röttgering, H. J. A. 2012. MNRAS, 425, L76

[23] Burns, J. O., Skillman, S. W., & O'Shea, B. W. 2010, ApJ, 721, 1105,"Galaxy Clusters at the Edge: Temperature, Entropy, and Gas Dynamics Near the Virial Radius"

[24] Byram, E. T., Chubb, T. A., Friedman, H. 1966, Science 152, 66, "Cosmic X-ray Sources, Galactic and Extragalactic"

[25] Chandra X-ray Center, Chandra Project Science, MSFC. Ahandra IPI Teams, 2016, "The Chandra Proposers Observatory Guide Version 19.0"

[26] Dickey, J., M., & Lockman, F., J. 1990 ARA&A, 28, 215, "H I in the Galaxy"

[27] Donnert, J., Dolag, K., Brunetti, G., & Cassano, R. 2013, MNRAS, 429, 3564, "Rise and fall of radio haloes in simulated merging galaxy clusters"

[28] Drury L. O. 198, Rep. Prog. Phys., 46, 973, "An introduction to the theory of diffusive shock acceleration of energetic particles in tenuous plasmas"

[29] Eckert, D., Molendi, S., & Paltani, S., 2011, A&A, 526, 79, "The cool-core bias in X-ray galaxy cluster samples. I. Method and application to HIFLUGCS"

[30] Ebeling, H., Edge, A. C., Bohringer, H., Allen, S. W., Crawford, C. S., Fabian, A. C., Voges, W., & Huchra, J. P., 1998, MNRAS, 301, 881, "The ROSAT Brightest Cluster Sample - I. The compilation of the sample and the cluster log N-log S distribution"

[31] Andrade-Santos, F., Nulsen P. E. J., Kraft, R. P., Forman, W. R., Jones, C., Churazov, E., & Vikhlinin, A. 2013, ApJ, 766, 107, "Dark Matter Subhalos and the X-Ray Morphology of the Coma Cluster"

[32] Feretti, L., Giovannini, G., & Böhringer, H. 1997, New Astron., 2, 501, "The radio and X-ray properties of Abell 2319"

[33] Feretti, L., Giovannini, G., Govoni, F., & Murgia, M. 2012, A&ARv, 20, 54, "Clusters of galaxies: observational properties of the diffuse radio emission"

[34] Ferrari, C., Govoni, F., Schindler, S., Bykov, A. M., & Rephaeli, Y., 2008, Space Sci. Rev., 134, 93, "Observations of Extended Radio Emission in Clusters"

[35] Finoguenov, A., Sarazin, C. L., Nakazawa, K., Wik, D. R., & Clarke, T. E. 2010, ApJ, 715, 1143, "XMM-Newton Observation of the Northwest Radio Relic Region in A3667"

[36] Fujita, Y., Takizawa, M., Yamazaki, R., Akamatsu, H., & Ohno, H., 2015, ApJ, 815, 116, "Turbulent Cosmic-Ray Reacceleration at Radio Relics and Halos in Clusters of Galaxies"

[37] Govoni, F., Markevitch, M., Vikhlinin, A., van Speybroeck, L., Feretti, L., & Giovannini, G., 2004, ApJ, 605, 695, "Chandra Temperature Maps for Galaxy Clusters with Radio Halos"

[38] Govoni, F., Murgia, M., Markevitch, M., Feretti, L., Giovannini, G., Taylor, G. B., & Carretti, E. 2009, A&A, 499, 371, "A search for diffuse radio emission in the relaxed, cool-core galaxy clusters A1068, A1413, A1650, A1835, A2029, and Ophiuchus"

[39] Giacintucci, S., Markevitch, M., Venturi, T., Clarke, T., E., Cassano, R., & Mazzotta, P. 2014, ApJ, 781, 9, "New Detections of Radio Minihalos in Cool Cores of Galaxy Clusters"

[40] Henry, J. P., Evrard, A. E., Hoekstra, H., Babul, A., & Mahdavi, A. 2009, ApJ, 691, 1307, "The X-Ray Cluster Normalization of the Matter Power Spectrum"

[41] Hilton, M., Romer, A. K., Kay, S., T., Mehrtens, N., Lloyd-Davies, E. J., Thomas, P., A., Short, C., J., Mayers, J., A., Rooney, P., J., Stott, J., P., Collins, C., A., Harrison, C., D., Hoyle, B., Liddle, A., R., Mann, R., G., Miller, C., J., Sahln, M., Viana, P., T., P., Davidson, M., Hosmer, M., Nichol, R., C., Sabirli, K., Stanford, S. A., West, M., J. 2012, MNRAS, 424, 2086, "The XMM Cluster Survey: evidence for energy injection at high redshift from evolution of the X-ray luminosity-temperature relation"

[42] Hindson, L., Johnston-Hollitt, M., Hurley-Walker, N., Buckley, K., Morgan, J., Carretti, E., Dwarakanath, K. S., Bell, M., Bernardi, G., Bhat, N. D. R., Bowman, J. D., Briggs, F., Cappallo, R. J., Corey, B. E., Deshpande, A. A., Emrich, D., Ewall-Wice, A., Feng, L., Gaensler, B. M., Goeke, R., Greenhill, L. J., Hazelton, B. J., Jacobs, D., Kaplan, D. L., Kasper, J. C., Kratzenberg, E., Kudryavtseva, N., Lenc, E., Lonsdale, C. J., Lynch, M. J., McWhirter, S. R., McKinley, B., Mitchell, D. A., Morales, M. F., Morgan, E., Oberoi, D., Ord, S. M., Pindor, B., Prabu, T., Procopio, P., Offringa, A. R., Riding, J., Rogers, A. E. E., Roshi, A., Shankar, N. U., Srivani, K. S., Subrahmanyan, R., Tingay, S. J., Waterson, M., Wayth, R. B., Webster, R. L., Whitney, A. R., Williams, A., Williams, C. L., 2014, MNRAS, 445, 330, "The First Murchison Widefield Array low-frequency radio observations of cluster scale non-thermal emission: the case of Abell 3667"

[43] Hong, S. E., Kang, H., & Ryu, D. 2015, ApJ, 812, 49, "Radio and X-Ray Shocks in Clusters of Galaxies"

[44] Hoang, D. N., Shimwell, T. W., Stroe, A., Akamatsu, H., Brunetti, G., Donnert, J. M. F., Intema, H. T., Mulcahy, D. D., Röttgering, H. J. A.,

van Weeren, R. J., Bonafede, A., Brggen, M., Cassano, R., Chyy, K. T., Enlin, T., Ferrari, C., de Gasperin, F., Gu, L., Hoeft, M., Miley, G. K., Orr, E., Pizzo, R., White, G. J. 2017, MNRAS, 471, 1107, " Deep LOFAR observations of the merging galaxy cluster CIZA J2242.8+5301"

[45] Ishisaki, Y., Maeda, Y., Fujimoto, R., Ozaki, M., Ebisawa, K., Takahashi, T., Ueda, Y., Ogasaka, Y., Ptak, A., Mukai, K., Hamaguchi, K., Hirayama, M., Kotani, T., Kubo, H., Shibata, R., Ebara, M., Furuzawa, A., Iizuka, R., Inoue, H., Mori, H., Okada, S., Yokoyama, Y., Matsumoto, H., Nakajima, H., Yamaguchi, H., Anabuki, N., Tawa, N., Nagai, M., Katsuda, S., Hayashida, K., Bamba, A., Miller, E., D., Sato, K., Yamasaki, N., Y. 2007, PASJ, 59, S113, "Monte Carlo Simulator and Ancillary Response Generator of Suzaku XRT/XIS System for Spatially Extended Source Analysis"

[46] Ishizaka, C. 1997, Ap&SS, 254, 233, "On the $\beta_{\rm SPEC}$ Values of Galaxy Clusters During the Merger"

[47] Itahana, M., Takizawa, M., Akamatsu, H., Ohashi, T., Ishisaki, Y., Kawahara, H., & van Weeren, R. J., 2015, PASJ, 67, 113, "Suzaku observations of the galaxy cluster 1RXS J0603.3+4214: Implications of particle acceleration processes in the Toothbrush radio relic"

[48] Jauzac, M., Eckert, D., Schwinn, J., Harvey, D., Baugh, C. M., Robertson, A., Bose, S., Massey, R., Owers, M., Ebeling, H., Shan, H. Y., Jullo, E., Kneib, J.-P., Richard, J., Atek, H., Clment, B., Egami, E., Israel, H., Knowles, K., Limousin, M., Natarajan, P., Rexroth, M., Taylor, P., & Tchernin, C. 2016, MNRAS, 463, 3876, "The extraordinary amount of substructure in the Hubble Frontier Fields cluster Abell 2744"

[49] Kale, R., Dwarakanath, K. S., Bagchi, J., & Paul, S. 2012, MNRAS, 426, 1204K, "Spectral and polarization study of the double relics in Abell 3376 using the Giant Metrewave Radio Telescope and the Very Large Array"

[50] Kang, H., & Ryu, D. 2015, ApJ, 809, 186, "Curved Radio Spectra of Weak Cluster Shocks"

[51] Koyama, K., Tsunemi, H., Dotani, T., Bautz, M., W., Hayashida, K., Tsuru, T., G., Matsumoto, H., Ogawara, Y., Ricker, G., R., Doty, J., Kissel, S., E., Foster, R., Nakajima, H., Yamaguchi, H., Mori, H., Sakano, M., Hamaguchi, K., Nishiuchi, M., Miyata, E., Torii, K., Namiki, M., Katsuda, S., Matsuura, D., Miyauchi, T., Anabuki, N., Tawa, N., Ozaki, M., Murakami, H., Maeda, Y., Ichikawa, Y., Prigozhin, G., Y. Boughan, E., A., Lamarr, B., Miller, E., D., Burke, B., E., Gregory, J., A. Pillsbury, A., Bamba, A., Hiraga, J., S., Senda, A., Katayama, H., Kitamoto, S., Tsujimoto, M., Kohmura, T., Tsuboi, Y., Awaki, H. 2007, PASJ, 59, 23, "X-Ray Imaging Spectrometer (XIS) on Board Suzaku"

[52] Kushino, A., Ishisaki, Y., Morita, U., Yamasaki, N. Y., Ishida, M., Ohashi, T., & Ueda, Y. 2002, PASJ, 54, 327, "Study of the X-Ray Background Spectrum and Its Large-Scale Fluctuation with ASCA"

[53] Landau, L. D., & Lifshitz, E. M. 1959, "Fluid Mechanics" (Oxford: Pergamon Press)

[54] Longair, M. S., 1994, Cambridge University Press, "High energy astrophysics Volume 2 : Stars, the Galaxy and the interstellar medium"

[55] Malkov, M. A., & Drury, L. O'C., 2001, Reports on Progress in Physics, 64, 429, "Nonlinear theory of diffusive acceleration of particles by shock waves"

[56] Markevitch, M., Gonzalez, A. H., David, L., Vikhlinin, A., Murray, S., Forman, W., Jones, C., & Tucker, W. 2002, ApJ, 567, 27, "A Textbook Example of a Bow Shock in the Merging Galaxy Cluster 1E 0657-56"

[57] Markevitch, M., Govoni, F., Brunetti, G., & Jerius, D. 2005, ApJ, 627, 733, "Bow Shock and Radio Halo in the Merging Cluster A520"

[58] Markevitch, M. 2010, arXiv.org, arXiv:1010.3660, "Intergalactic shock fronts"

[59] Miniati, F 2002 MNRAS, 337, 199, "Intergalactic shock acceleration and the cosmic gamma-ray background"

[60] Mitsuda, K., Bautz, M., Inoue, H., Kelley, R. L., Koyama, K., Kunieda, H., Makishima, K., Ogawara, Y., Petre, R., Takahashi, T., Tsunemi, H., White, N. E., Anabuki, N., Angelini, L., Arnaud, K., Awaki, H., Bamba, A., Boyce, K., Brown, G. V., Chan, K., Cottam, J., Dotani, T., Doty, J., Ebisawa, K., Ezoe, Y., Fabian, A. C., Figueroa, E., Fujimoto, R., Fukazawa, Y., Furusho, T., Furuzawa, A., Gendreau, K., Griffiths, R. E., Haba, Y., Hamaguchi, K., Harrus, I., Hasinger, G., Hatsukade, I., Hayashida, K., Henry, P. J., Hiraga, J. S., Holt, S. S., Hornschemeier, A., Hughes, J. P., Hwang, U., Ishida, M., Ishisaki, Y., Isobe, N., Itoh, M., Iyomoto, N., Kahn, S. M., Kamae, T., Katagiri, H., Kataoka, J., Katayama, H., Kawai, N., Kilbourne, C., Kinugasa, K., Kissel, S., Kitamoto, S., Kohama, M., Kohmura, T., Kokubun, M., Kotani, T., Kotoku, J., Kubota, A., Madejski, G. M., Maeda, Y., Makino, F., Markowitz, A., Matsumoto, C., Matsumoto, H., Matsuoka, M., Matsushita, K., McCammon, D., Mihara, T., Misaki, K., Miyata, E., Mizuno, T., Mori, K., Mori, H., Morii, M., Moseley, H., Mukai, K., Murakami, H., Murakami, T., Mushotzky, R., Nagase, F., Namiki, M., Negoro, H., Nakazawa, K., Nousek, J. A., Okajima, T., Ogasaka, Y., Ohashi, T., Oshima, T., Ota, N., Ozaki, M., Ozawa, H., Parmar, A. N., Pence, W. D., Porter, F. S., Reeves, J. N., Ricker, G. R., Sakurai, I., Sanders, W. T., Senda, A., Serlemitsos, P., Shibata, R. Soong, Y., Smith, R., Suzuki, M., Szymkowiak, A. E., Takahashi, H., Tamagawa, T., Tamura, K., Tamura, T., Tanaka, Y., Tashiro, M., Tawara, Y., Terada, Y., Terashima, Y., Tomida, H., Torii, K., Tsuboi, Y., Tsujimoto, M., Tsuru, T. G., Turner, M. J. L.., Ueda, Y., Ueno, S., Ueno, M., Uno, S., Urata, Y., Watanabe, S., Yamamoto, N., Yamaoka, K., Yamasaki, N. Y., Yamashita, K, Yamauchi, M., Yamauchi, S., Yaqoob, T., Yonetoku, D., Yoshida, A., 2007, PASJ, 59, 1, "The X-Ray Observatory Suzaku"

[61] Nakazawa, K., Sarazin, C., L., Kawaharada, M., Kitaguchi, T., Okuyama, S., Makishima, K., Kawano, N., Fukazawa, Y., Inoue, S., Takizawa, M., Wik, D., R., Finoguenov, A., & Clarke, T., E. 2009, PASJ, 61, 339, "Hard X-Ray Properties of the Merging Cluster Abell 3667 as Observed with Suzaku"

[62] Novicki, Megan C., Sornig, Manuela, & Henry, J. Patrick, 2002, AJ, 124, 2413, "The Evolution of the Galaxy Cluster Luminosity-Temperature Relation"

[63] Ogrean, G. A., Brüggen, M., van Weeren, R. J., Röttgering, H., Croston, J. H., & Hoeft, M. 2013, MNRAS, 433, 812, "Challenges to our understanding of radio relics: X-ray observations of the Toothbrush cluster"

[64] Ogrean, G. A., Brüggen, M., van Weeren, R., Röttgering, H., Simionescu, A., Hoeft, M., & Croston, J. H. 2014, MNRAS, 440, 3416, "Multiple density discontinuities in the merging galaxy cluster CIZA J2242.8+5301"

[65] Ohno, H., Takizawa, M., & Shibata, S. 2002, ApJ, 577, 658, "Radio Halo Formation through Magnetoturbulent Particle Acceleration in Clusters of Galaxies"

[66] Okabe, N., Zhang, Y.-Y., Finoguenov, A., Takada, M., Smith, G. P., Umetsu, K., & Futamase, T. 2010, ApJ, 721,875, "LoCuSS: Calibrating Mass-observable Scaling Relations for Cluster Cosmology with Subaru Weak-lensing Observations"

[67] Okabe, N., Umetsu, K., Tamura, T., Fujita, Y., Takizawa, M., Zhang, Y., Matsushita, K., Hamana, T., Fukazawa, Y., Futamase, T., Kawaharada, M., Miyazaki, S., Mochizuki, Y., Nakazawa, K., Ohashi, T., Ota, N., Sasaki, T., Sato, K., Tam, S., 2014, PASJ, 66, 99, "Universal profiles of the intracluster medium from Suzaku X-ray and Subaru weak-lensing observations"

[68] Okabe, N., Futamase, T., Kajisawa, M., & Kuroshima, R. 2014, ApJ, 784, 90, "Subaru Weak-lensing Survey of Dark Matter Subhalos in the Coma Cluster: Subhalo Mass Function and Statistical Properties"

[69] Okabe, N., Futamase, T., Kajisawa, M., & Kuroshima, R. 2014, ApJ, 784, 90, "Subaru Weak-lensing Survey of Dark Matter Subhalos in the Coma Cluster: Subhalo Mass Function and Statistical Properties"

[70] Okabe, N., Umetsu, K., Tamura, T., Fujita, Y., Takizawa, M., Matsushita, K., Fukazawa, Y., Futamase, T., Kawaharada, M., Miyazaki, S., Mochizuki, Y., Nakazawa, K., Ohashi, T., Ota, N., Sasaki, T., Sato, K., & Tam, S. I. 2016, MNRAS, 456, 4475, "Central mass profiles of the nearby cool-core galaxy clusters Hydra A and A478"

[71] Ota, N., Murase, K., Kitayama, T., Komatsu, E., Hattori, M., Matsuo, H., Oshima, T., Suto, Y., & Yoshikawa, K., 2008, A&A, 491, 363, "Suzaku broad-band spectroscopy of RX J1347.5-1145: constraints on the extremely hot gas and non-thermal emission"

[72] Ota, N., Nagayoshi, K., Pratt, G. W., Kitayama, T., Oshima, T., & Reiprich, T. H., 2014, A&A, 562, 60

[73] Pacholczyk, A. G. 1970, "Radio astrophysics. Nonthermal processes in galactic and extragalactic sources"

[74] Pinzke, A., Oh, S. P., & Pfrommer, C. 2013, MNRAS, 435, 1061, "Giant radio relics in galaxy clusters: reacceleration of fossil relativistic electrons?"

[75] Pizzo, R. F., & de Bruyn, A. G. 2009, A&A, 507, 639, " Radio spectral study of the cluster of galaxies Abell 2255"

[76] Planck Collaboration, 2013, A&A, 550, A134, "Planck intermediate results. VIII. Filaments between interacting clusters"

[77] Planck Collaboration, 2013, A&A, 550, A140, "Planck intermediate results. X. Physics of the hot gas in the Coma cluster"

[78] Popesso, P. M., Böhringer, H., Brinkmann, J., Voges, W., & York, D. G. 2004, A&A, 423, 449, "RASS-SDSS Galaxy clusters survey. I. The catalog and the correlation of X-ray and optical properties"

[79] Ricker, P., M., & Sarazin, C., L., 2001, ApJ, 561, 621, "Off-Axis Cluster Mergers: Effects of a Strongly Peaked Dark Matter Profile"

[80] Röttgering, H. J. A., Wieringa, M. H., Hunstead, R. W., & Ekers, R. D., 1997, MNRAS, 290, 577, "The extended radio emission in the luminous X-ray cluster A3667"

[81] Rybicki, G. B., & Lightman, A. P. 1979, "Radiative Processes in Astrophysics" (New York: John Wiley & Sons)

[82] Ryu, D., Kang, H., Hallman, E., & Jones, T. W. 2003, ApJ, 593, 599, "Cosmological Shock Waves and Their Role in the Large-Scale Structure of the Universe"

[83] Sarazin, C. L. 1988, "X-ray emission from clusters of galaxies", (Cambridge University Press)

[84] Scaife, Anna M. M., Oozeer, Nadeem, de Gasperin, Francesco, Brggen, Marcus, Tasse, Cyril, & Magnus, Lindsay, 2015, MNRAS, 451, 4021, "KAT-7 detection of radio halo emission in the Triangulum Australis galaxy cluster"

[85] Sekiya, N., Yamasaki, N. Y., Mitsuda, K., & Takei, Y. 2014, PASJ, 66, 3, "O I fluorescent line contamination in soft X-ray diffuse background obtained with Suzaku/XIS"

[86] Serlemitsos, P., J., Soong, Y., Chan, K., Okajima, T., Lehan, J., P., Maeda, Y., Itoh, K., Mori, H., Iizuka, R., Itoh, A., Inoue, H., Okada, S., Yokoyama, Y., Itoh, Y., Ebara, M., Nakamura, R., Suzuki, K., Ishida, M., Hayakawa, A., Inoue, C., Okuma, S., Kubota, R., Suzuki, M., Osawa, T., Yamashita, K., Kunieda, H., Tawara, Y., Ogasaka, Y., Furuzawa, A., Tamura, K., Shibata, R., Haba, Y., Naitou, M., Misaki, K. 2007, PASJ, 59, 9, "The X-Ray Telescope onboard Suzaku"

[87] Shafer, R., A. 1983, PhD. Thesis, University Maryland

[88] Smith, G., P., Kneib, J.-P., Smail, I., Mazzotta, P., Ebeling, H., & Czoske, O. 2005, MNRAS, 359, 417, "A Hubble Space Telescope lensing survey of X-ray luminous galaxy clusters - IV. Mass, structure and thermodynamics of cluster cores at $z = 0.2$"

[89] Shu, F., H. 1992, “The Physics of Astrophysics. Volume II: Gas Dynamics” (Mill Valley: University Science Books)

[90] Skillman, S. W., Xu, H., Hallman, E. J., O’Shea, B. W., Burns, J. O., Li, H., Collins, D. C., & Norman, M. L. 2013, ApJ, 765, 21, ”Cosmological Magnetohydrodynamic Simulations of Galaxy Cluster Radio Relics: Insights and Warnings for Observations”

[91] Stroe, A., Harwood, J. J., Hardcastle, M. J., Röttgering, H. J. A. 2014, MNRAS, 445, 1213, “Spectral age modelling of the ‘Sausage’ cluster radio relic”

[92] Stroe, A., Shimwell, T., Rumsey, C., van Weeren, R., Kierdorf, M., Donnert, J., Jones, T. W., Röttgering, H. J. A., Hoeft, M., Rodrguez-Gonzlvez, C., Harwood, J. J., & Saunders, R. D. E. 2016, MNRAS, 455, 2402, “The widest frequency radio relic spectra: observations from 150 MHz to 30 GHz”

[93] Sugawara, C., Takizawa, M., & Nakazawa, K., 2009, PASJ, 61, 1293, “Suzaku Observation of the Radio Halo Cluster Abell 2319: Gas Dynamics and Hard X-Ray Properties”

[94] Sugawara, Y., Takizawa, M., Itahana, M., Akamatsu, H., Fujita, Y., Ohashi, T.,& Ishisaki, Y. 2017, accepted for publication in PASJ, (arXiv:1708.09074), “ Suzaku Observations of the Outskirts of the Galaxy Cluster Abell 3395 including a Filament toward Abell 3391”

[95] Sunyaev, R. A. & Zeldovich, Ya. B. 1972, Comm. Astrophys. Space Phys. 4, 173, “The Observations of Relic Radiation as a Test of the Nature of X-Ray Radiation from the Clusters of Galaxies”

[96] Institute of Space and Astronautical Science (ISAS/JAXA), “ The Suzaku Technical Description”

[97] Takizawa, M. 1999, ApJ, 520, 514, “Two-Temperature Intracluster Medium in Merging Clusters of Galaxies”

[98] Takizawa, M. 2005, ApJ, 629, 791, "Hydrodynamic Simulations of a Moving Substructure in a Cluster of Galaxies: Cold Fronts and Turbulence Generation"

[99] Takizawa,M. 2008, ApJ, 687, 951, "N-Body + Magnetohydrodynamical Simulations of Merging Clusters of Galaxies: Characteristic Magnetic Field Structures Generated by Bulk Flow Motion"

[100] Takizawa, M., Nagino, R., & Matsushita, K. 2010, PASJ, 62, 951, "Mass Estimation of Merging Galaxy Clusters"

[101] Tawa, N., Hayashida, K., Nagai, M., Nakamoto, H., Tsunemi, H., Yamaguchi, H., Ishisaki, Y., Miller, E., D., Mizuno, T., Dotani, T., Ozaki, M., Katayama, H. 2008, PASJ, 60, 11, "Reproducibility of Non-X-Ray Background for the X-Ray Imaging Spectrometer aboard Suzaku"

[102] Thierbach, M., Klein, U., & Wielebinski, R. 2003, A&A, 397, 53, "The diffuse radio emission from the Coma cluster at 2.675 GHz and 4.85 GHz"

[103] Trasatti, M., Akamatsu, H., Lovisari, L., Klein, U., Bonafede, A., Brggen, M., Dallacasa, D., & Clarke, T. 2015, A&A, 575, 45, "The radio relic in Abell 2256: overall spectrum and implications for electron acceleration"

[104] van Weeren, R. J., Röttgering, H. J. A., Brüggen, M., & Hoeft, M., 2010, Science, 330, 347, "Particle Acceleration on Megaparsec Scales in a Merging Galaxy Cluster"

[105] van Weeren, R. J., Brüggen, M., Röttgering, H. J. A., Hoeft, M., Nuza, S. E., & Intema, H. T. 2011, A&A, 533, 35, "Radio continuum observations of new radio halos and relics from the NVSS and WENSS surveys. Relic orientations, cluster X-ray luminosity, and redshift distributions"

[106] van Weeren, R. J., Röttgering, H. J. A., Intema, H. T., Rudnick, L., Brüggen, M., Hoeft, M., Oonk, J. B. R. 2012, A&A, 546, A124, "The toothbrush-relic: evidence for a coherent linear 2-Mpc scale shock wave in a massive merging galaxy cluster?"

[107] van Weeren, R., J., Brunetti, G., Brggen, M., Andrade-Santos, F., Ogrean, G. A., Williams, W. L., Röttgering, H. J. A., Dawson, W. A., Forman, W. R., de Gasperin, F., Hardcastle, M. J., Jones, C., Miley, G. K., Rafferty, D. A., Rudnick, L., Sabater, J., Sarazin, C. L., Shimwell, T. W., Bonafede, A., Best, P. N., Brzan, L., Cassano, R., Chyy, K. T., Croston, J. H., Dijkema, T. J., Enlin, T., Ferrari, C., Heald, G., Hoeft, M., Horellou, C., Jarvis, M. J., Kraft, R. P., Mevius, M., Intema, H. T., Murray, S. S., Orrú, E., Pizzo, R., Sridhar, S. S., Simionescu, A., Stroe, A., van der Tol, S., White, G. J. 2016, ApJ, 818, 204, "LOFAR, VLA, and Chandra Observations of the Toothbrush Galaxy Cluster"

[108] Vazza, F., Brunetti, G., Kritsuk, A., Wagner, R., Gheller, C., & Norman, M. 2009, A&A, 504, 33

[109] Vink, J., & Yamazaki, R. 2014, ApJ, 780, 125, "A Critical Shock Mach Number for Particle Acceleration in the Absence of Pre-existing Cosmic Rays: $M = sqrt5$"

[110] Vink, J., Broersen, S., Bykov, A., & Gabici, S. 2015, A&A 579, 13, "On the electron-ion temperature ratio established by collisionless shocks"

[111] Watanabe, E., Takizawa, M., Nakazawa, K., Okabe, N., Kawaharada, M., Babul, A., Finoguenov, A., Smith, G., P., & Taylor, J., E. 2011, PASJ, 63, 357, "Suzaku X-Ray Follow-Up Observation of Weak-Lensing-Detected Halos in the Field around ZwCl 0823.2+0425"

[112] Willingale, R., Starling, R. L. C., Beardmore, A. P., Tanvir, N. R., & O'Brien, P. T. 2013, MNRAS, 431, 394, "Calibration of X-ray absorption in our Galaxy"

[113] Wilson, S., Hilton, M., Rooney, P. J., Caldwell, C., Kay, S. T., Collins, C. A., McCarthy, I., G., Romer, A. K., Bermeo, A., Bernstein, R., da Costa, L., Gifford, D., Hollowood, D., Hoyle, B., Jeltema, T., Liddle, A., R., Maia, M., A. G., Mann, R., G., Mayers, J., A., Mehrtens, N., Miller, C., J., Nichol, R., C., Ogando, R., Sahln, M., Stahl, B., Stott, J., P., Thomas, P. A., Viana, P., T., P., Wilcox, H. 2016, MNRAS, 463,

413, “The XMM Cluster Survey: evolution of the velocity dispersion-temperature relation over half a Hubble time”

[114] Wu, X.P., Fang, L.Z., & Xu, W., 1998, A&A, 338, 813, “Updating the sigma -T relationship for galaxy clusters”

[115] Xue, Y.J., Wu, X.P., 2000, ApJ, 538, 65, “The $L_X - T$, $L_X - \sigma$, and $\sigma - T$ Relations for Groups and Clusters of Galaxies”

[116] Yamaguchi, H., Koyama, K., Katsuda, S., Nakajima, H., Hughes, J., P., Bamba, A., Hiraga, J., S., Mori, K., Ozaki, M., Tsuru, T., G. 2008, PASJ, 60, 141, “X-Ray Spectroscopy of SN 1006 with Suzaku”

[117] Yamaguchi, H., Eriksen, K. A., Badenes, C., Hughes, J. P., Brickhouse, N. S., Foster, A. R., Patnaude, D. J., Petre, R., Slane, P. O., & Smith, R. K. 2014, ApJ, 780, 136, “New Evidence for Efficient Collisionless Heating of Electrons at the Reverse Shock of a Young Supernova Remnant”

[118] Yoshino, T., Mitsuda, K., Yamasaki, N. Y., Takei, Y., Hagihara, T., Masui, K., Bauer, M., McCammon, D., Fujimoto, R., Wang, Q. D., & Yao, Y. 2009, PASJ, 61, 805, “Energy Spectra of the Soft X-Ray Diffuse Emission in Fourteen Fields Observed with Suzaku”

[119] ZuHone, J. A., Markevitch, M., & Lee, D. 2011, ApJ, 743, 16, “Sloshing of the Magnetized Cool Gas in the Cores of Galaxy Clusters”